# ON THE START UP OF SUPERSONIC UNDEREXPANDED JETS

Thesis by
Nehemias Lima Lacerda

In Partial Fulfillment
of the Requirements for the Degree of
Doctor of Philosophy

California Institute of Technology
Pasadena, California

1987
(Submitted 22 August 1986)

Dedicated to Marcia and Marcelo

## ACKNOWLEDGMENTS

First of all I would like to thank my advisor, Professor Bradford Sturtevant, for his constant suggestions, advice, motivation, enthusiasm and invaluable editorial assistance throughout the course of this work.

I am grateful to Prof. Edward Zukoski for his valuable contribution during the performance of this work. I would also like to thank my friends, in particular Dr. David Frost and Dr. Jane Lin for stimulating discussions as well as my fellow student Adiel Guinzburg for their English assistance.

I am grateful to all the secretaries, librarians, technicians, and other Caltech staff that directly or indirectly helped me so that this work could be completed. I would like to especially point out Taras Kiceniuk for his friendship.

Finally I am especially grateful to the Brazilian Air Ministry, that sent me to CALTECH to obtain the degree of Ph.D. and in particular to Maj.Brig. Hugo de Oliveira Piva and Cel. Erler Schall Amorin for their support and enthusiasm towards this mission. I am also sincerely grateful to Dr. Anatol Roshko, as well as, to Aydeth Roshko for their encouragement and attention to my family and I.

This research was supported by National Science Foundation under Grant No. EAR-8218445.

# ABSTRACT

An impulsively started jet can be formed by a gas confined in a high pressure reservoir that escapes suddenly through an exit orifice, into a controlled atmosphere. Supersonic gas jets of this type are unsteady and differ from the steady jet that develops later by the presence of a bow shock, a jet head and a nonstationary Mach disk. The effects of the pressure ratio between the high pressure gas inside the reservoir and the lower pressure atmospheric gas, as well as the gas combination used, are studied experimentally. The gases used for the jet and the atmosphere were selected from helium, nitrogen and sulfur hexafluoride.

The data acquisition consisted of: high resolution flash photography to obtain detail from the pictures; high-speed movie pictures to obtain the time development of selected features; and fast-response pressure transducers located at the reservoir end plate, the tank end plate and the jet exit.

The initial development of the jet is highly time dependent. During this phase, the shape that the jet assumes varies with pressure ratio and with the choice of gas. In particular an extremely light gas exhausting into a heavy atmosphere, exhibits an uncommon shape. It develops as a bubble wrapped by the bow shock, that increases its volume with flow time and pressure ratio. As the pressure ratio increases, it becomes more tightly wrapped by the bow shock. At later times the jet assumes conventional linear growth.

After the jet starts, a Mach disk is observed close to the jet exit which moves downstream as the exit pressure builds up. The monotonic increase in exit pressure is caused by the slow breaking of the diaphragm. The position of the Mach disk is furthest from the jet exit when the exit pressure is a maximum. After that it oscillates around the location predicted by the steady theory of Ashkenas & Sherman (1966) at a frequency close to one of the resonant frequencies of the reservoir. The features observed for the inner structure of the jet were verified to agree with those obtained for impulsive flow generated by a muzzle blast.

The frontal part of the jet forms the jet head, whose shape changes with the flow conditions. The initial evolution of the jet head is linear but after propagating a distance of around ten exit diameters, it reaches asymptotic behavior with an evolution that is approximately proportional to square root of time. The head creates a bow shock ahead of it that propagates downstream and increases the pressure of the atmospheric gas. This bow shock was found to be less attenuated than in spherically symmetric explosions. The asymptotic behavior of the bow shock was reached after about eight exit diameters.

# TABLE OF CONTENTS

# LIST OF FIGURES

## LIST OF TABLES

# LIST OF SYMBOLS

| Symbol | Description | Reference |
|---|---|---|
| $a$ | Sound speed | |
| $d$ | Jet exit diameter measured on high-speed film | |
| $D$ | Jet exit diameter | |
| $l$ | Reservoir length | |
| $\dot{m}$ | mass flux | |
| $M$ | Mach number | |
| $P$ | Pressure | |
| $R$ | Universal gas constant | |
| $S$ | Entropy | |
| $t$ | Time | |
| $T$ | Temperature | |
| $u$ | Velocity | |
| $X$ | Position | |
| $W$ | Molecular weight | |

Greek Letters

| | | |
|---|---|---|
| $\beta$ | Growth-law index for bow shock | |
| $\gamma$ | Ratio of specific heats | |
| $\Delta$ | Variation | |
| $\lambda$ | Growth-law index for jet head | |
| $\nu$ | Kinematic viscosity | |
| $\rho$ | Density | |
| $\omega$ | Frequency | |

Subscripts

| | | |
|---|---|---|
| $a$ | Undisturbed atmospheric conditions | |
| $e$ | Jet exit properties | |
| $i$ | Initial exhaust properties | |
| $m$ | Downstream of the Mach Disk | |
| $n$ | upstream of the Mach disk | |
| $o$ | Undisturbed reservoir conditions | |
| $t$ | Transition | |
| $\infty$ | State far downstream | |

## Chapter 1

## INTRODUCTION

A supersonic jet may be initiated by breaking a thin diaphragm that separates a pressurized reservoir from the ambient atmosphere, provided the pressure ratio between the reservoir and the outer ambient is large enough. During the initial phase of this flow, the physical properties of the fluid are highly time dependent. Supersonic gas jets of this type are unsteady and differ from the steady jet that develops later by the presence of a bow shock, a jet head and a nonstationary Mach disk (see figure 1.1).

Under steady conditions the flow at the minimum cross section of the jet is sonic and the fluid expands supersonically downstream if the pressure ratio is high enough. If the static pressure at the exit of the jet is higher than the ambient pressure, an underexpanded jet is formed, but if these pressures are equal, the jet is said to be pressure matched. For the underexpanded case a system of normal and oblique waves are present within the jet to adjust the pressure to the ambient value. The normal waves are called Mach disks, while the first outer oblique wave often takes the form of a barrel shock. For low pressure ratios, the cell formed by the Mach disk and the oblique shocks is repetitive, and forms the well-known diamond cell structure. For the pressure-matched jet, the Mach disk is always unsteady and moves away from the exit just upstream of the jet head. It is the purpose of this work to determine how the jet structure develops as a function of time in an impulsively initiated underexpanded jet.

In an impulsive jet the head is defined as that part containing the starting vortex bounded downstream by the interface between the driver and the driven fluids. It is the portion of the flow that is inherently nonsteady. Unsteadiness of the jet head generates acoustic disturbances that propagate outward into the atmosphere. The initial

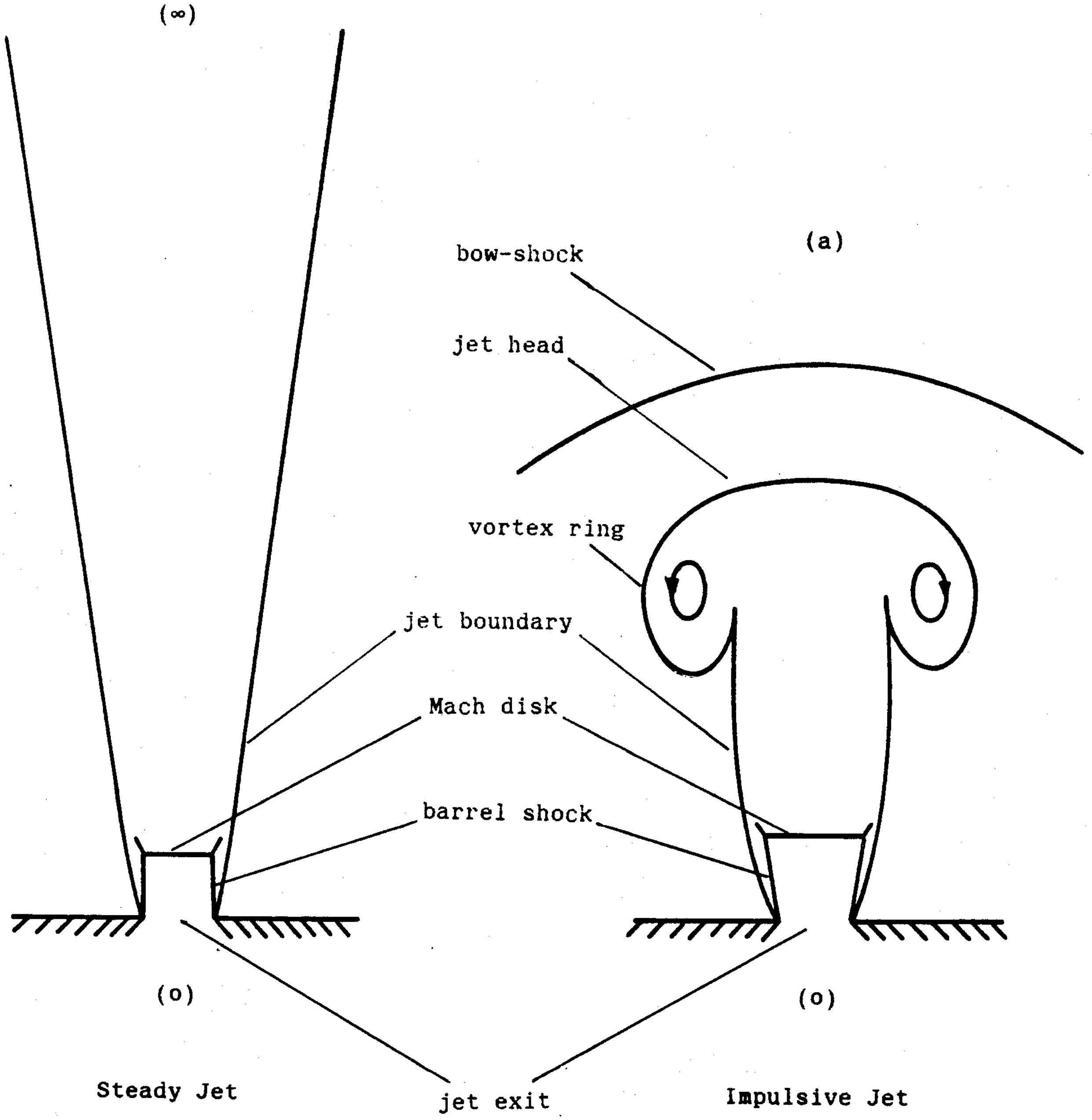

Figure 1.1 Comparison between steady and impulsive jets of gases.

disturbance is the bow shock, formed by the sudden injection of fluid into the ambient atmospheric gas. It separates the low- and high-pressure fluids, and induces a flow in the undisturbed outer fluid. The strength of the bow shock decreases as it propagates away from the source.

### 1.1. Motivation.

The present work is a continuation of the work done by Kieffer & Sturtevant (1984), motivated by the desire to understand the effects of jet and atmospheric composition and pressure ratio on the starting phase of an underexpanded supersonic jet. In the present investigation, a pressurized reservoir served as the driver for a 7 mm diameter jet issuing into a controlled atmosphere. The gases for the reservoir and atmosphere were helium (He), nitrogen ($N_2$) and sulfur hexafluoride ($SF_6$). High speed photography and fast-response pressure measurements were used to obtain qualitative and quantitative data. The present experiments were performed to investigate the influence of pressure ratio $P_o/P_a$ and molecular weight ratio $W_o/W_a$ on the jet development, the initial phase of propagation of the bow shock and jet head, and the development of the Mach disk.

The most important accomplishment of this work is the elucidation of the behavior of the starting phase of the supersonic jet. The effect of the pressure and the molecular weight ratios on the jet shape has been systematically documented. The following chapters include a qualitative and quantitative description and analysis of the influence of these parameters on the flow field behavior.

### 1.2. Previous related work.

Both experimental and computational studies have been carried out by earlier investigators on the behavior of unsteady jets of gases. The work that is most closely related to the present work is the experimental research done by Kieffer & Sturtevant (1984). They studied high molecular weight gas jets as an analog for particulate-laden volcanic fluids erupting into air and low molecular weight gases to simulate, for example, steam into water. Tombach (1969) measured velocity in inhomogeneous turbulent subsonic jets. He found the axial profile of the jet width for several cases involving different gas combinations. The jet width was obtained by fitting a normal distribution to the velocity profile which was obtained experimentally. Naboko et al. (1979) proposed time dependent relations for the development of both the bow shock and the jet head for argon, nitrogen and carbon dioxide jets, with exit Mach numbers ranging from 3 to 5. Norman et al. (1983) used a numerical simulation of the time dependent, axisymmetric equations of motion to investigate pressure-matched jets. Schmidt & Shear (1974) analyzed the flow structure formed downstream of the muzzle of an M16 rifle during firing. Both precursor and propellant gas flows were considered, and power laws for the development of the bow shock and jet head were obtained. They included plots of the development of the Mach disk and compared the Mach disk evolution with the corresponding steady jet theory. Ashkenas & Sherman (1966) checked the validity of previous results on the Mach disk location of steady jet by using the impact pressure and free molecule wire technique, which covers a wide range of pressure ratios and a variety of monatomic, diatomic and triatomic gases. They found that the Mach disk location is a function of the pressure ratio only, being independent of $\gamma_0$. A theoretical approach to this problem was given by Young (1975), who found the location of the Mach disk in a free jet using the entropy balance principle. He showed that the dependence on $\gamma_0$ is weak, and obtained results close to those obtained by Ashkenas & Sherman. A great deal of information concerning exhaust plume technology can be found in Chapter 2 in JANNAF (1975). This handbook provides information and bibliography of previous works regarding the Mach disk location for steady jets.

## 1.3. Outline of Present work.

The objective of the present experimental work was to investigate the physical mechanisms involved in the starting phase of unsteady jets. Information concerning the experimental method and measurement procedure is contained in Chapter 2. Chapter 3 consists of a survey of results showing the influence of pressure and gas combination on the outer flow field, as well as the temporal development of the jet.

Experimental results, including both qualitative descriptions and quantitative data are given for the Mach disk in Chapter 4, for the jet head in Chapter 5 and for the bow shock in Chapter 6. In Chapter 7 the data obtained from the three previous chapters are discussed together with an analysis of the jet interior. Finally, the conclusions of this investigation are given in Chapter 8.

Appendix A contains some comments on the wave structure close to the jet exit and explanations concerning the pressure history at the top of the tank, the jet exit and the bottom of the reservoir. An attempt to find a general method to filter the data obtained from the high-speed movies is given in Appendix B. A general description of the high-speed camera used, as well as a description of the experiment performed to calibrate the camera for timing purposes, is included in Appendix C. In appendix D, theoretical arguments on the evolution of the Mach disk and the jet head are presented.

# Chapter 2

# EXPERIMENTAL FACILITY AND INSTRUMENTATION

## 2.1. Shock Tube.

The apparatus in the present experiment is a modified version of the one used by Kieffer & Sturtevant (1984). The apparatus was modified to include the capability of varying the ambient gas and its corresponding pressure (up to 0.1 MPa). The apparatus is shown in figure 2.1 and consists of a high pressure reservoir and a low pressure tank: each is filled with one of the test gases (He, $N_2$ or $SF_6$). The tank and reservoir are separated by an aluminum diaphragm. Before starting an experimental run, both compartments are evacuated to remove the residual gas from a previous run. The tank is then filled with the "atmosphere" gas at the selected pressure. The reservoir is slowly filled with the "jet" gas until the diaphragm breaks. After the diaphragm breaks, the flow of the reservoir gas into the tank forms an unsteady supersonic jet that develops and decays within an interval of time less than 0.1 s. In some experiments flash schlieren photography stops the jet at a selected instant of time, while in others motion picture schlieren photography continuously records the development of the jet. The pressure history at the top of the tank, the jet exit and the bottom of the reservoir are recorded by fast-response pressure transducers.

A detailed view of the tank-reservoir interface is given in figure 2.2 . The contraction section is made in two parts to allow the aluminum diaphragm to be inserted between them. This schematic shows that the constant area section of the reservoir smoothly contracts to a minimum cross section area at jet exit, with an area contraction ratio of 86. The small exit area was chosen in order to get an acceptable jet image length. The reservoir cross section must be large enough to avoid viscous effects (boundary layer formation) and to provide enough

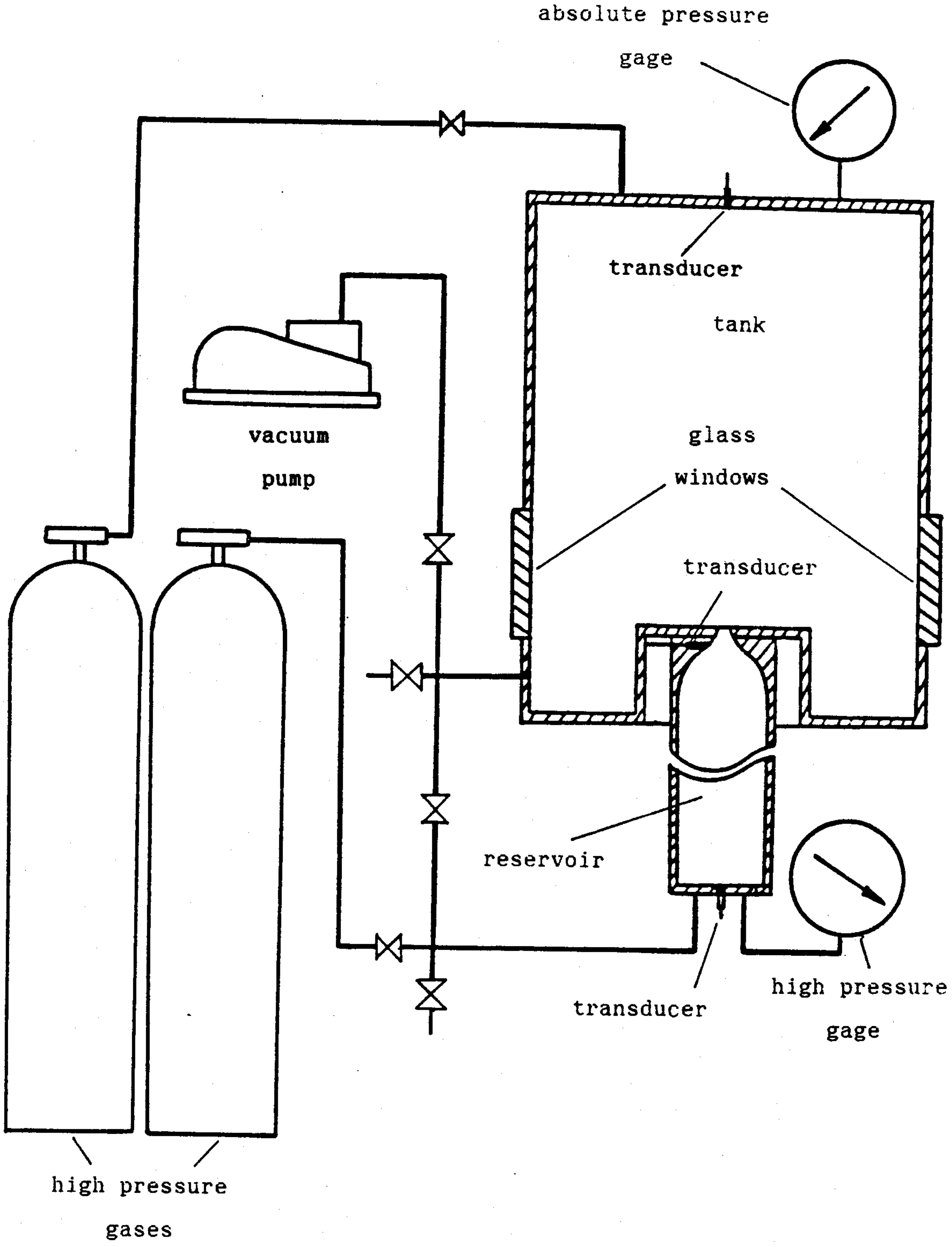

Figure 2.1 Experimental apparatus showing the shock tube and pressure lines connecting the bourdon tube manometers, vacuum pump and gas supply . The pressure transducers are also included.

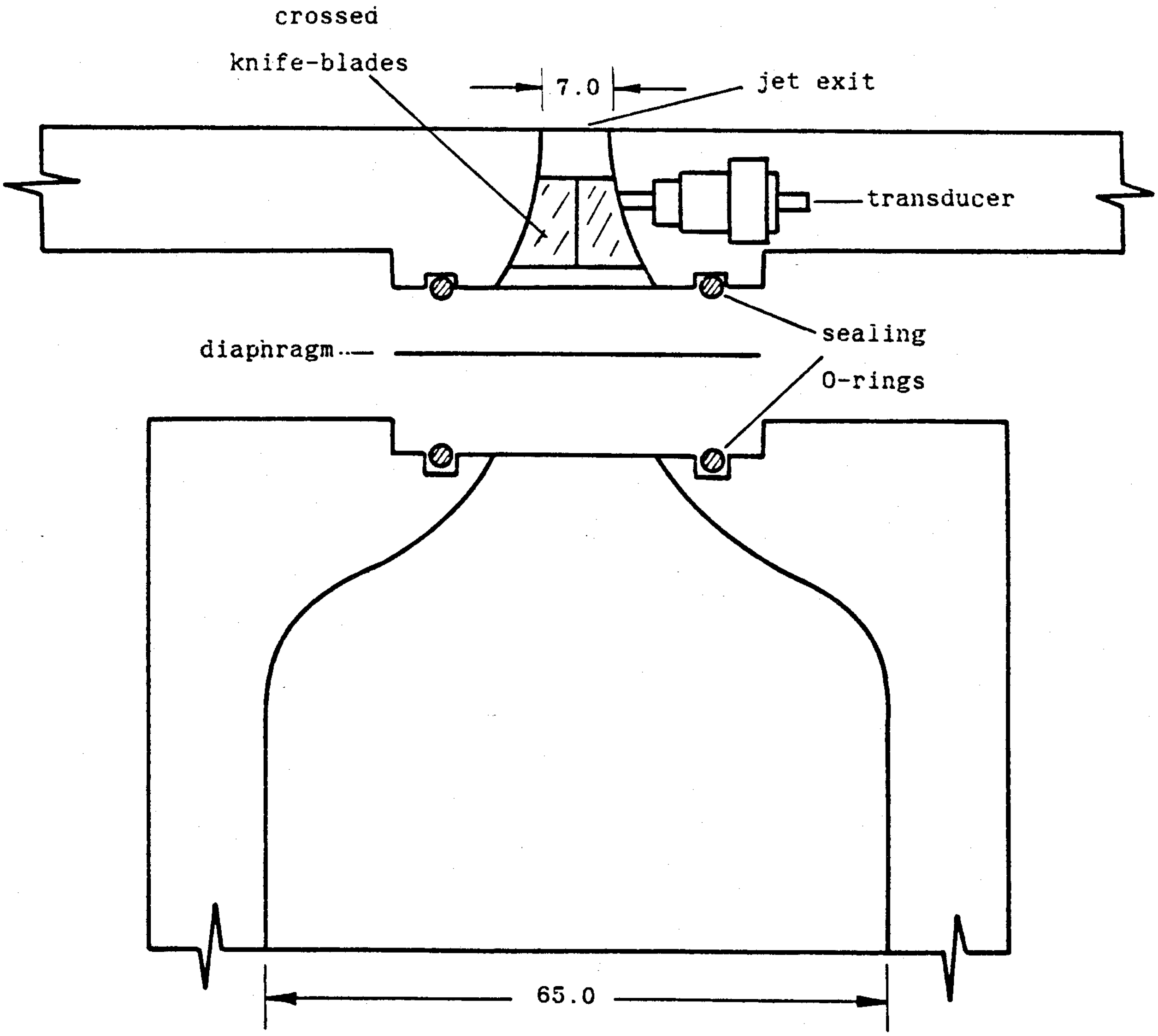

Figure 2.2 Exploded view of the contraction section, showing how the diaphragm is placed. The location of the cross-blades and the pressure transducer is also shown. Dimensions are in mm.

volume of gas to get a suitable run time. The flow is sonic at the exit of the jet, and consequently the jet under study is underexpanded and supersonic. Other nozzle geometries such as the Laval nozzle can be used to investigate pressure-matched-jets. Figure 2.2 also shows that the diaphragm is placed in the contraction section 1.5 mm upstream of the crossed knife-blades that serve to rupture the diaphragm cleanly. O-rings contact the diaphragm on each side to seal the tank and reservoir. Within the range of the cross blades a pressure transducer is located to record the static pressure at the jet exit.

The tank is constructed of steel with an internal diameter of 38.6 cm, height of 52.0 cm and an internal volume of 0.060 $m^3$. The test section has two glass windows (12.4 cm diameter each) that are optically flat to within 0.5 $\mu m$. The contraction section is constructed of brass while the reservoir is aluminum. The length of the reservoir (l) may be varied and the reservoir volume depends upon the gas in use: 125 $cm^3$ for $SF_6$ (l = 5.13 cm), 395 $cm^3$ for $N_2$ (l = 13.5 cm) and 1200 $cm^3$ for He (l = 38.9 cm). The volume scaling for each gas was obtained empirically, based on the amount of gas at the same initial pressure that provides approximately the same pressure drop after the same time interval. These volumes were obtained analytically using equation 10 from Kieffer & Sturtevant (1984) and was based on the calculated emptying time of a pressurized reservoir containing a perfect gas discharging into a vacuum. Isentropic flow was assumed and lead to the results that were used as a starting point for the empirical solution. The empirical results were found to be close to the analytical values, however $N_2$ showed the largest discrepancy with a volume 7% larger than calculated.

Experiments are carried out with tank pressures of 10, 50 and 100 KPa, using aluminum diaphragms of 76 and 13 $\mu m$ thickness. The possible combinations between the two diaphragm thicknesses and the three tank pressures provides pressure ratios between the reservoir and tank of 3, 10, 20, 50 and 100.

## 2.2. Description of the Gases.

The gases used for the jet and atmosphere were selected from nontoxic, nonflamable gases with saturation pressure above 20 MPa at room temperature. The gases were chosen to provide as large a density contrast as possible.

He and $N_2$ were obtained with a stated purity of 99.99% and 99.995% while the $SF_6$ was 99.8% pure. Selected physical properties for these three gases are shown in table 2.1.

Table 2.1 Properties of He, $N_2$ and $SF_6$

| Property | He | $N_2$ | $SF_6$ |
|---|---|---|---|
| Density (273 K)<br>$\rho$ (kg/m$^3$) | 0.1785 | 1.2516 | 6.520 |
| Molecular weight<br>W (Kg/Kmol) | $4.0026^2$ | $28.013^2$ | $146.05^2$ |
| Kinematic viscosity (300 K)<br>$\nu$ ($10^{-6}$ m$^2$/s) | $110.4^2$ | $14.22^2$ | $2.342^4$ |
| Specific heat ratio (300 K)<br>$\gamma$ | 1.667 | 1.4 | $1.093^1$ |
| Sound speed (273 K)<br>a (m/s) | $965^2$ | $334^2$ | $149^3$ |
| Gladstone-Dale constant (273 K)<br>sodium D line | $0.000036^5$ | $0.000297^5$ | $0.000783^4$ |

1. Tacheon (1975)
2. Weast (1983)
3. Calculated using empirical relation from Hammond (1972)
4. Marshall (1976)
5. Liepmann & Roshko (1957)

## 2.3. Pressure Measurements.

The measurement of pressure in the nozzle and reservoir sections was facilitated by the use of fast-response pressure transducers. The transducers used were PCB models 112A21 and 113A21 high-sensitivity quartz transducers manufactured by Piezotronics. Specifications for these dynamic transducers are given in table 2.2.

Table 2.2 - Specification for the Dynamic Transducer

| Specification | 112A21 | 113A21 |
|---|---|---|
| Resolution @ S/N = 1 (Pa)<br>(noise 200 $\mu$v p-p) | 27.5 | 68.9 |
| Sensitivity (mv/KPa) | 7.44 | 3.62 |
| Rise time ($\mu$s) | 2.0 | 1.0 |
| Resonant Frequency (Khz) | 250 | 500 |
| Discharge time constant (s) | 1.0 | 1.0 |
| Linearity (%) | 1.0 | 1.0 |

A PCB model 112A21 transducer is located flush-mounted in the reservoir end plate, another PCB model 112A21 transducer is also flush-mounted at tank end plate and PCB model 113A21 transducer is located in the nozzle, recessed near the jet exit. The first transducer measures the decay of pressure within the reservoir, The second measures the arrival of shock waves at the top of the tank while the third measures the pressure history at the throat, and, in the flash schlieren experiments, also provides an electrical signal for triggering. With this pulse, the time delay electronics trigger the spark-gap used to record the jet picture at a preset instant of time, as described in section 2.4.1 below.

The pressure signals are recorded by a Nicolet Model 4094 digital oscilloscope and stored on floppy disks. The digital pressure data are then transferred via a GP-IB interface to a PDP-11 computer for data analysis and plotting.

## 2.4. Flow Visualization.

The jet as well as the shock waves are visualized using the schlieren technique. For turbulent jets, a common technique to improve the visibility of the steady wave structure is to increase the exposure time. For example, Donaldson et al. (1966) obtained two pictures of steady jets, the first taken with a short duration spark-gap, and the second with long-exposure continuous illumination. Examples of these photographs are shown in figure 2.3. The first picture shows a jet frozen during a short time interval (on the order of $\mu$s), while the second jet is averaged over a longer time interval (on the order of ms) and shows a clearer wave structure. In the present experiments a long exposure is impractical, since for unsteady jets, features change on time scales on the order of microseconds. To record the high-speed flow, both spark-photographs and high speed movies were taken.

The schlieren system used is of the so-called "Z" type, and is shown in figures 2.4 and 2.5. Due to the physical boundaries in the lab, plane mirrors were used to deflect the light beam as shown in the figures. The focal length of the spherical mirror closest to the spark gap is 1.65 m and 1.14 m for the other. In order to visualize density gradients in all directions, an opaque circular dot (250 $\mu$m diameter), replaced the usual knife edge at the focus of the second mirror. This dot was constructed using the techniques of photolithographic reduction. The dot was made small enough so that the primary, undeflected light beam was not totally blocked. This insured optimum sensitivity and contrast on the exposed film.

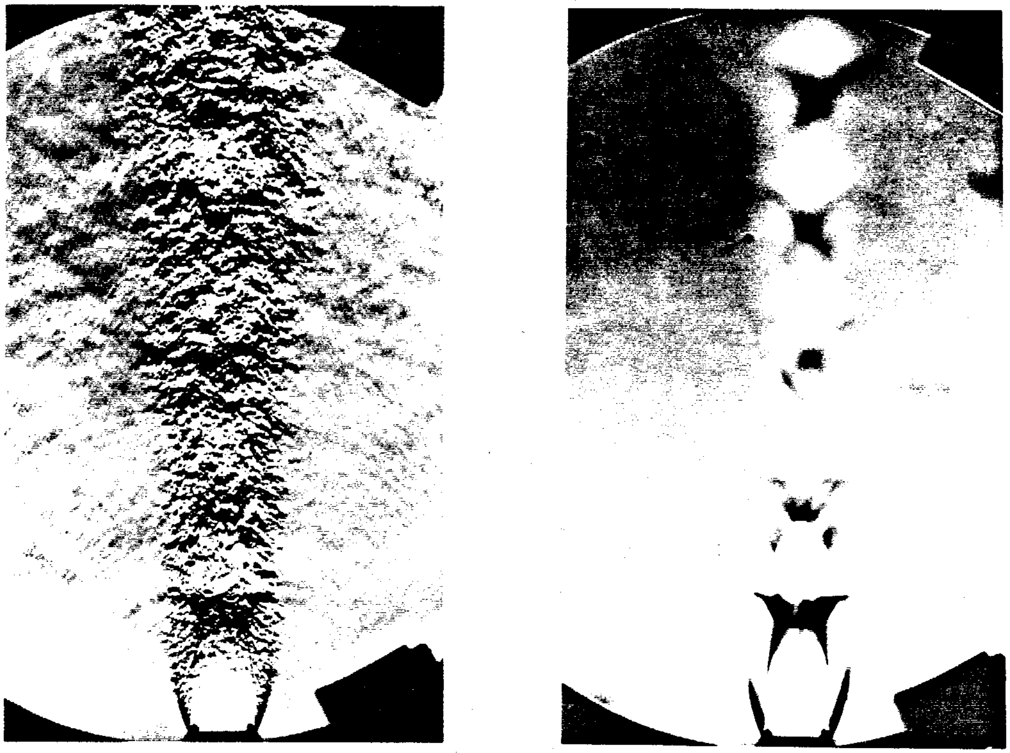

Spark Gap

Continuous Light

Figure 2.3 Schlieren photographs of a steady jet of air into air for different time exposure (from Donaldson et al., 1966).

2.4.1. <u>Photography</u>. To obtain spark-illuminated photographs, the signal detected by the pressure transducer in the nozzle after the diaphragm breaks is shaped and delayed by the pulse generator shown in figure 2.4. The resulting signal triggers the digital oscilloscope, which then records the pressure transducer outputs. The pulse generator output is also used to trigger the high voltage power supply. The power supply is used to charge the spark gap capacitor (0.1 $\mu$F, 10 kV rated for operation) to 10 kV as well as sending a 2 KV pulse that discharges the spark gap. The triggering pulse ionizes the gas between the electrodes, discharging the capacitor and providing a 1 $\mu$s duration light pulse. The flow structure is recorded on Polaroid 667 (ASA 3000) film.

2.4.2. <u>High Speed Movie</u>. The single-realization photographic process described above provides photographs with very good spatial resolution, but is tedious because a large number of pictures is required to document the flow, and is not useful for timing and velocity measurements. To obtain multiple pictures during a single run, with poorer spatial resolution than the spark schlieren photographs, a high speed Cordin model 374A camera was used in the configuration shown in figure 2.5. The camera consists of a rotating drum and a counter-rotating prism, using a 1.00 m long piece of 70 mm (ASA 400) film. A general description of this apparatus is included in Appendix C. For a light source, the spark gap source described above was replaced by a high pressure continuous 100 W mercury arc lamp with a luminous flux of 2200 lm, intensity of 260 cd and luminous area of 0.25 x 0.25 mm. To take a movie of the flow, some changes in the electronics were required because of the slow camera shutter. Time delay devices were connected to allow the camera to trigger the experiment. Before initiating the data acquisition, the camera is readied for an experimental run. After it reaches its preset drum speed of 50,000 frames per second and the lights in the lab are turned off, the experiment may be started by pushing the camera control button that opens the camera shutter in about 13 ms. Enabling the camera also causes a pulse delayed by 50 ms and width of 10 ms to open the electronic shutter (see figure 2.5).

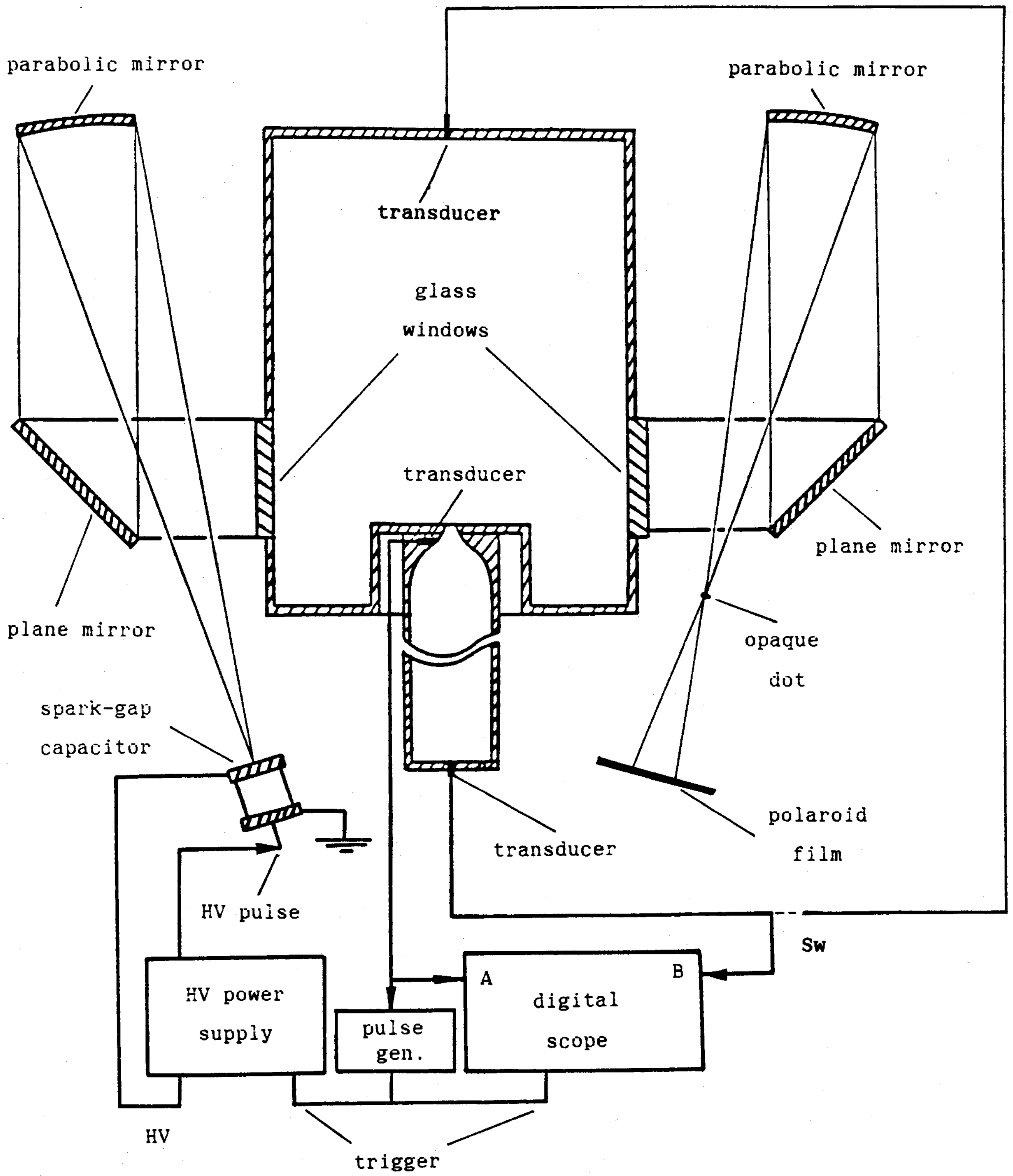

**Figure 2.4** The optical and electronic data aquisition system for a single picture experiment.

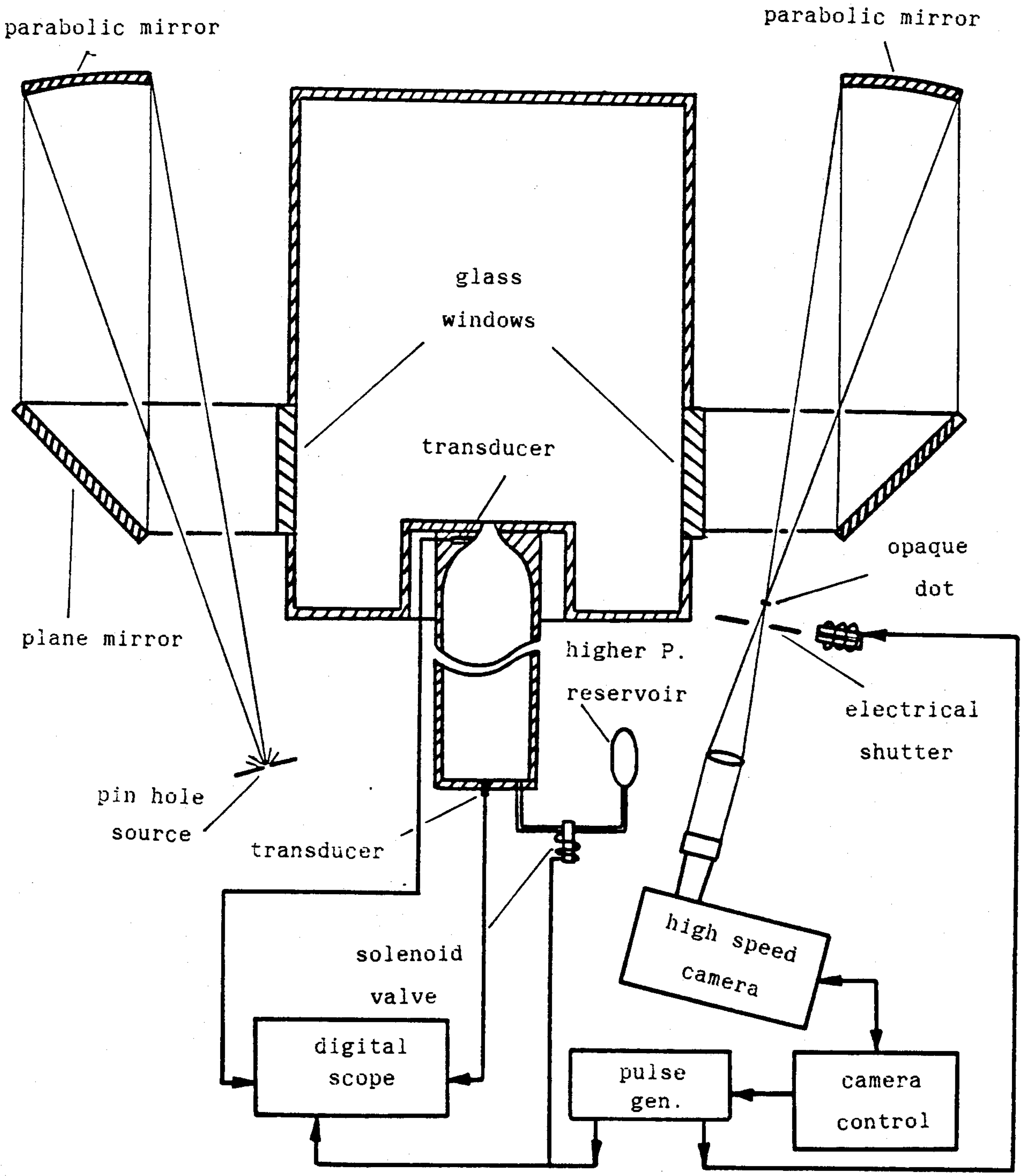

**Figure 2.5** **The optical and electronic data aquisition system for multiple picture experiment.**

The shutter (manufactured by Uniblitz, model 26LOA3X5) has an aperture time of 1.3 ms. Simultaneously, the pulse generator sends another pulse to open the solenoid valve that connects the reservoir to a higher pressure reservoir. Once this valve is opened, the pressure inside the reservoir rises until the diaphragm breaks. The transient jet is initiated and the film recording is possible since by now both shutters are fully open. After the electrical shutter closes, to avoid double exposure of the film, the camera shutter also closes. The 50 ms delay allows for the filling time of the reservoir and the 10 ms pulse width provides for the recording of the 16 mm frames at 50,000 frames per second on the 70 mm film in the configuration shown in Appendix C . Typically, the timing with this set up was sufficiently accurate to acquire 200 frames of useful data out of a possible 512 frames.

# Chapter 3

# GENERAL SURVEY OF RESULTS

## 3.1. Introduction.

Using the spark-illuminated apparatus described earlier, a large number of high resolution photographs of transient jets were obtained. A selection of the photographs was chosen to form a matrix of data arranged according to the gas combination, pressure ratio and development time of the jet. The nine figures shown in this chapter illustrate the variety of jet features that has been observed in the present work. Each one of the nine figures represents a different gas combination.

This chapter will consist of a qualitative survey of the matrix of photographs that will describe the main features that occur in the outer flow field. In general, for each figure the first four columns of photographs correspond to the initial unsteady phase of the flow, while the latter three cover the quasi-steady flow features.

In general the appearance of flow fields is strongly dependent on the method of flow visualization, and the present experiments are no exception. In particular, schlieren systems are sensitive to density gradients. In view of the relatively large density differences that would be expected to occur in dense gases, it should be expected that in the present study the visualization will accentuate the features in heavy gases at the expense of those in light gases. The cases involving light into light combinations (figure 3.9) show the shock structure in the jet, while the cases of light into heavy (figure 3.3) show the jet envelope, i.e. the turbulent shear layer, and the bow shock. The cases of heavy into light (figures 3.4 and 3.7) show the jet interior, and only the heavy into heavy (figure 3.1) show both the structure inside the jet and in the atmospheric gas. Intersections between shock waves, such as between the Mach disk and the barrel shock, produce turbulent shear layers. These slipstreams are easily seen in jets of heavy gases into light (figures 3.4, 3.7 and 3.8). For tests in which the gas densities are close (figures 3.1, 3.5 and 3.9), the visibility of the shock cell structure is improved, and the shear layer is visible, so linear spatial growth for developed, steady shear layers can be verified. For the jets under study the Reynolds numbers based on exit diameter and exit sound speed are $5 \times 10^4$ for the He jet, $15 \times 10^4$ for the $N_2$ jet and $45 \times 10^4$ for the $SF_6$ jet.

## 3.2. Jet Shape.

The shape that the jet assumes is always strongly dependent on the pressure ratio and the ratio of specific heats ($\gamma$) of the jet gas. For high pressure ratio and low $\gamma$ (figure 3.1, 3.4 and 3.7) the jet is plume-like, because the Prandtl-Meyer angle of the expansion at the exit is large under these conditions. Unfortunately, in the high pressure ratio case of He → $SF_6$ (figure 3.3) the flow is completely obscured after 500 $\mu$s by the turbulence induced in the heavy driven gas. This continues for as long as 20 ms, until the jet entrains the disturbed gas and carries it out of the test section. During the late, low-pressure-ratio quasi-steady phase, when the jet is visible, it has the appearance of a conventional subsonic jet with a spreading angle close to $25^o$. The lower pressure ratio cases from figures 3.3, 3.6 and 3.8, for the quasi-steady phase, show (quantitatively) the same visual linear growth as in figures 7 and 15 from Tombach (1969), but the light into heavy combinations exhibited different growth when compared with his results that were obtained from velocity measurements in his figure 14. Tombach defined the jet thickness to be the distance from the jet axis to the position where the velocity is half that of the velocity on the jet axis. With this definition, the light into heavy combination appears to grow faster visually than by using the velocity thickness.

For cases involving light into heavy combinations (figures 3.2 and 3.3), the light gas jet has a bubble-like shape with a bow shock wrapped tightly around it. The penetration of the light gas into the heavy gas is severely damped by the higher inertia atmosphere. The high resistance to the axial movement of the jet gas causes a larger lateral growth that forms the observed cocoon. The damping increases with mass flow rate. As the pressure ratio increases more gas is driven into the atmosphere. This forms a bigger bubble and increases the speed of the head, causing the head to be more tightly wrapped by the bow shock.

The shape of the jet is also highly dependent on the molecular weight ratio of the jet and atmospheric gases. For the case of a heavy jet into a light atmosphere (figure 3.7), the jet is ballistic and shows a dramatically different behavior than the light into heavy described above. It appears quite collimated, apparently due to reduced interaction with the atmosphere due to its high momentum flux. For the equal density case He → He (figure 3.9), at low pressure ratios, the structure of the jet becomes unstable about six diameters downstream of the jet exit. This is probably as a result of the helical instability characteristic of axisymmetric jets.

## 3.3. Mach Disk.

A Mach disk is formed downstream of the jet exit for all the underexpanded jets observed in the present experiments. As is well known, the late-time quasi-steady location of the Mach disk depends on the pressure ratio $P_0/P_a$. In the present experiments it varies from one to seven diameters downstream of the exit; the largest values were for the experiment that involved $SF_6$ jets (figure 3.1, 3.4 and 3.7) with $P_0/P_a = 100$. A comparison of this case with other cases verifies that the Mach disk location is a stronger function of pressure ratio than of $\gamma_0$, for both the unsteady and quasi-steady flow phases. The structure of the jet in the neighborhood of the Mach disk is treated in Appendix A.

The repeated diamond cell structure for low pressure ratio jets, for example in figure 3.5, is caused by compression and reexpansion of the jet fluid as it adjusts to the ambient conditions.

## 3.4. Jet Head.

For heavy ambient fluids the jet head often takes the shape of a vortex ring. For the case of $SF_6 \rightarrow SF_6$ (figure 3.1) at moderate pressure ratios, the vorticity is confined to a rather compact ring, but for the case of $He \rightarrow SF_6$ (figure 3.3) the ring spreads into a cocoon of recirculating fluid around the outside and obscures the jet. In general, for cases involving a light atmosphere (figure 3.7), there is no visible recirculating fluid, but rather, the head is smaller and has a pinched appearance. The higher the pressure ratio, the more the jet plumes. This is because of the influence of the pressure ratio on the Prandtl-Meyer angle.

## 3.5. Bow Shock.

The bow shock is strongest for light jets into dense atmospheres (figure 3.3) because the strength of the shock is dependent on the velocity of the jet head, which in turn depends on the speed of sound in the jet gas. The shape of the jet head of course influences the shape of the bow shock, particularly for the cases of light into heavy gases (figure 3.2). In this case, the distorted head (in the shape of a vortex ring or cocoon), is moving at supersonic speed, and every little bump on the surface of the head induces a disturbance on the bow shock.

Aeroacoustical effects in the form of noise generated by the jet, are also evident in the photographs. Oblique acoustic waves are generated in the atmosphere for the case of a light jet into a heavy ambient gas (figure 3.2, 3.3 and 3.6). The larger the Mach number of the jet, the smaller the angle between the waves and the jet axis. In this respect, the most extreme example occurs for the case of $He \rightarrow SF_6$ (figure 3.3) at low pressure ratios. On the other hand, for the case of $SF_6 \rightarrow He$ (figure 3.7) there are no visible acoustic waves present.

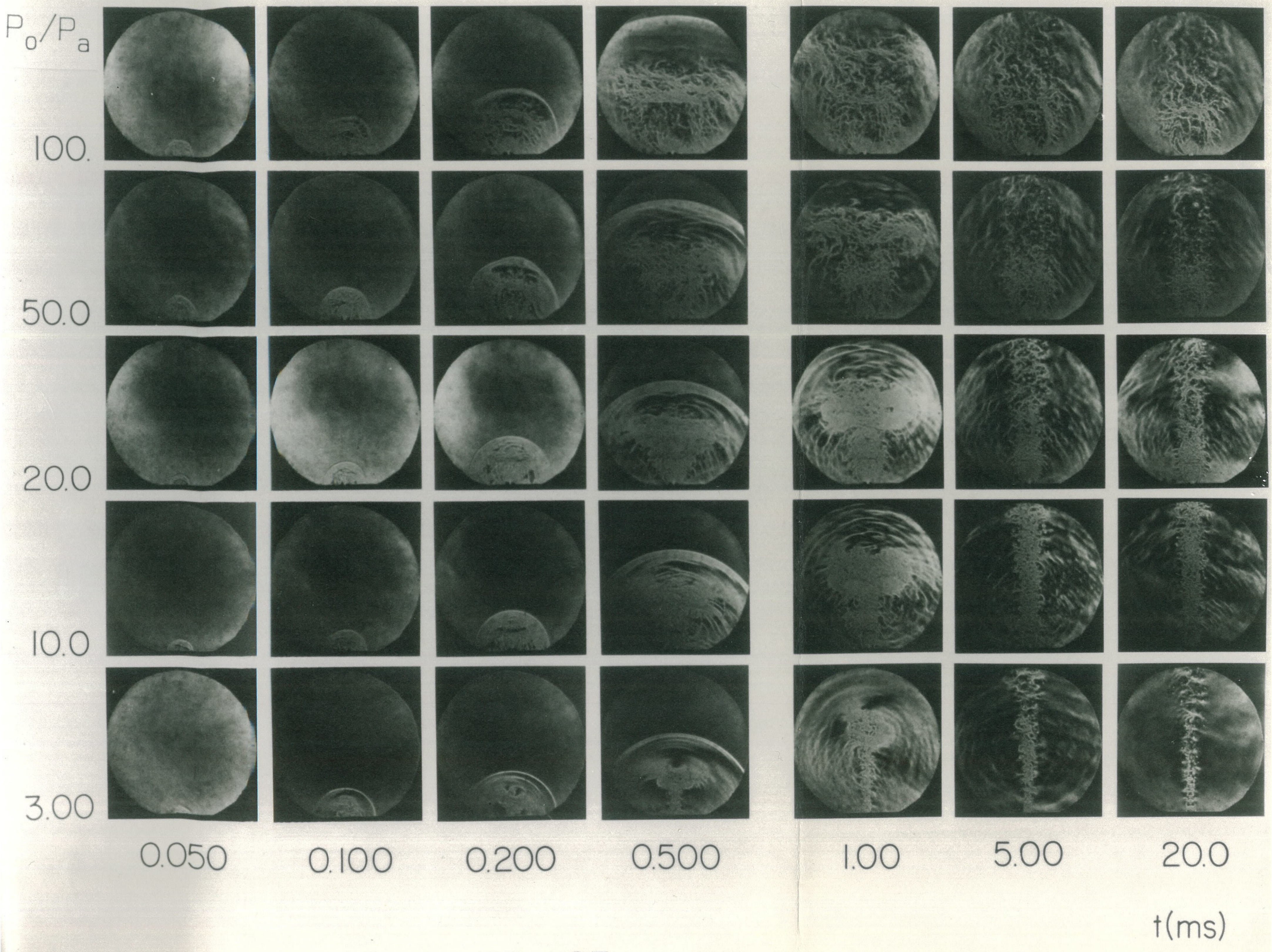

Figure 3.1 — $SF_6 \rightarrow SF_6$

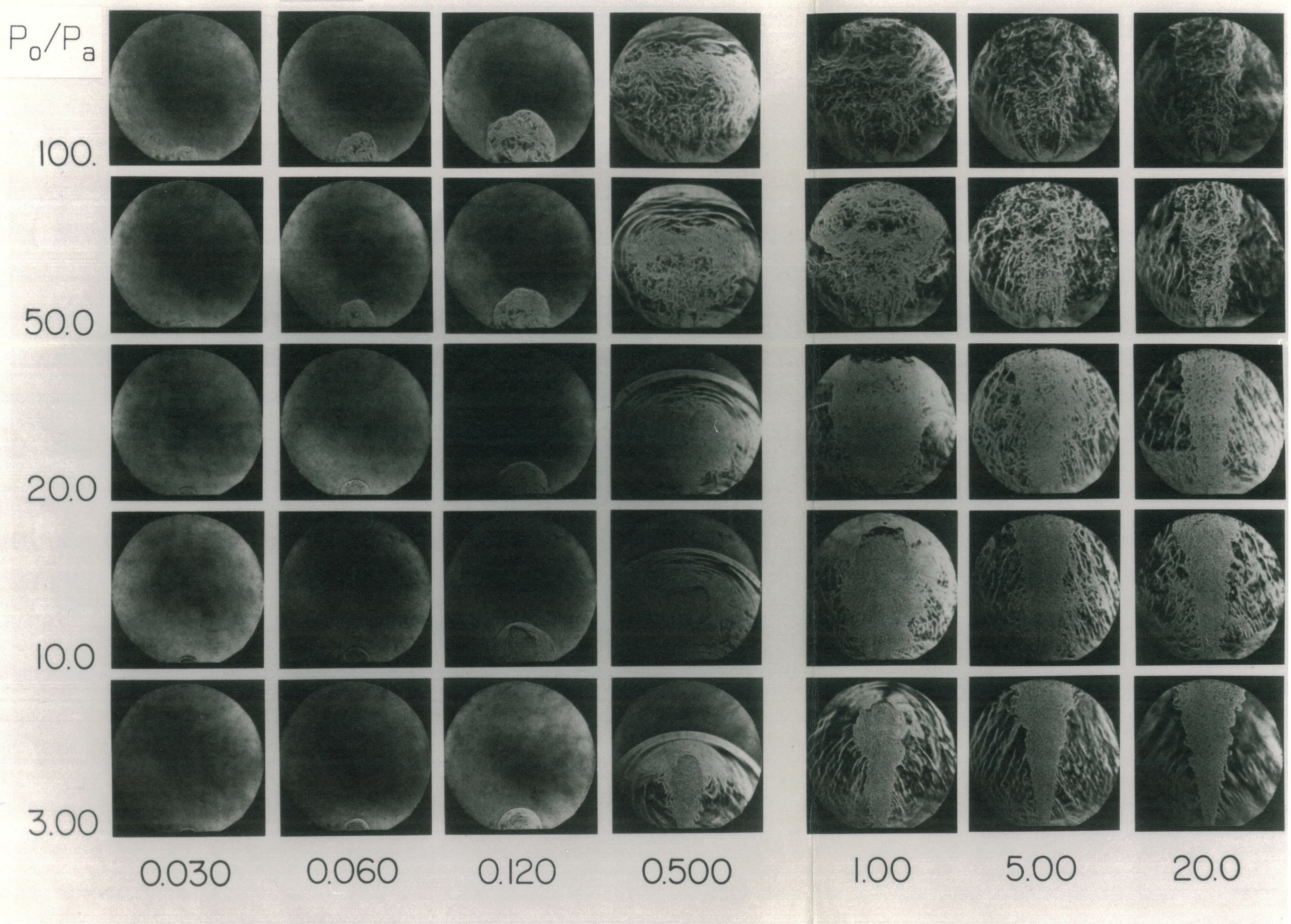

Figure 3.2 — $N_2 \rightarrow SF_6$

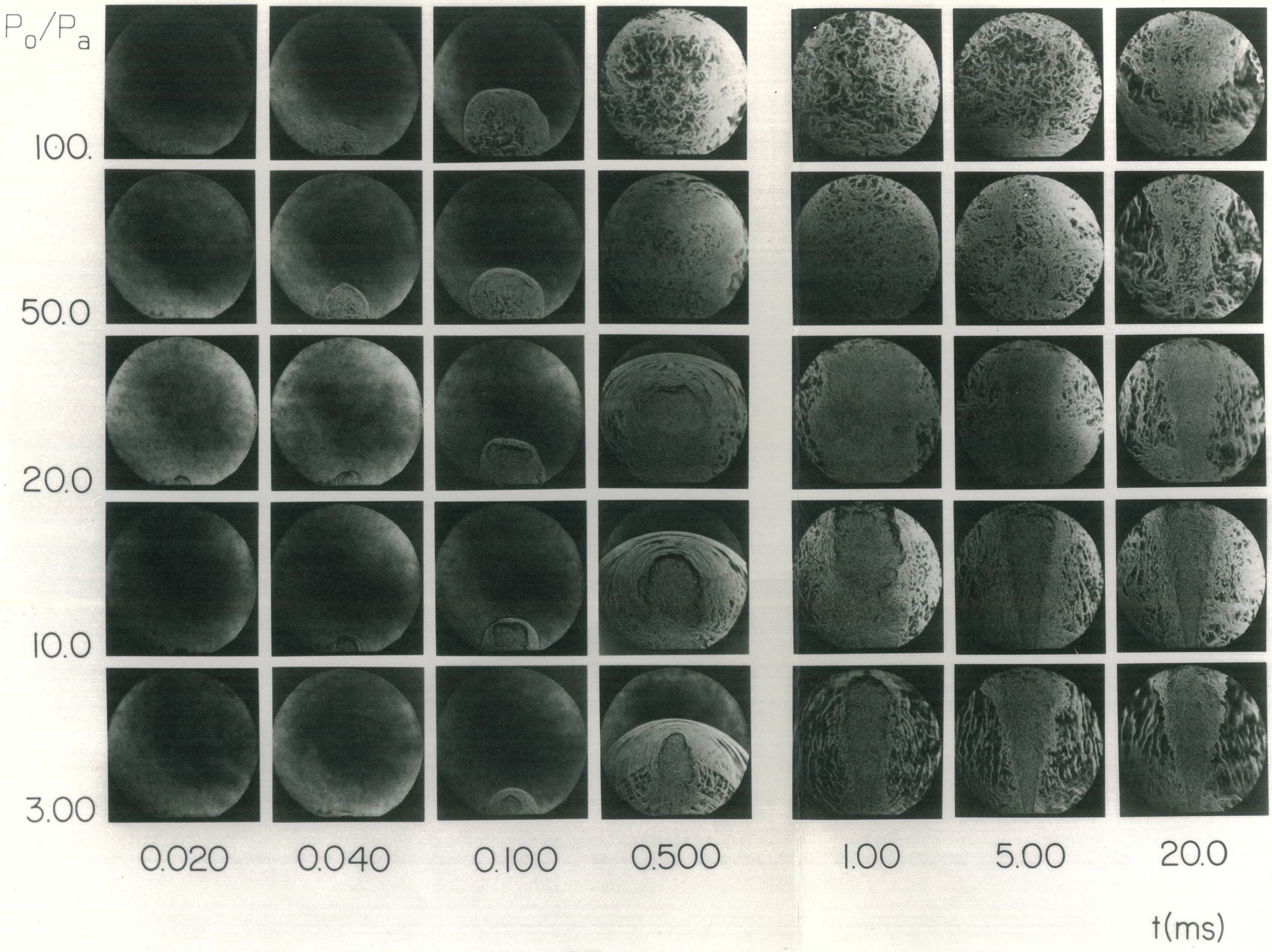

Figure 3.3 — He → $SF_6$

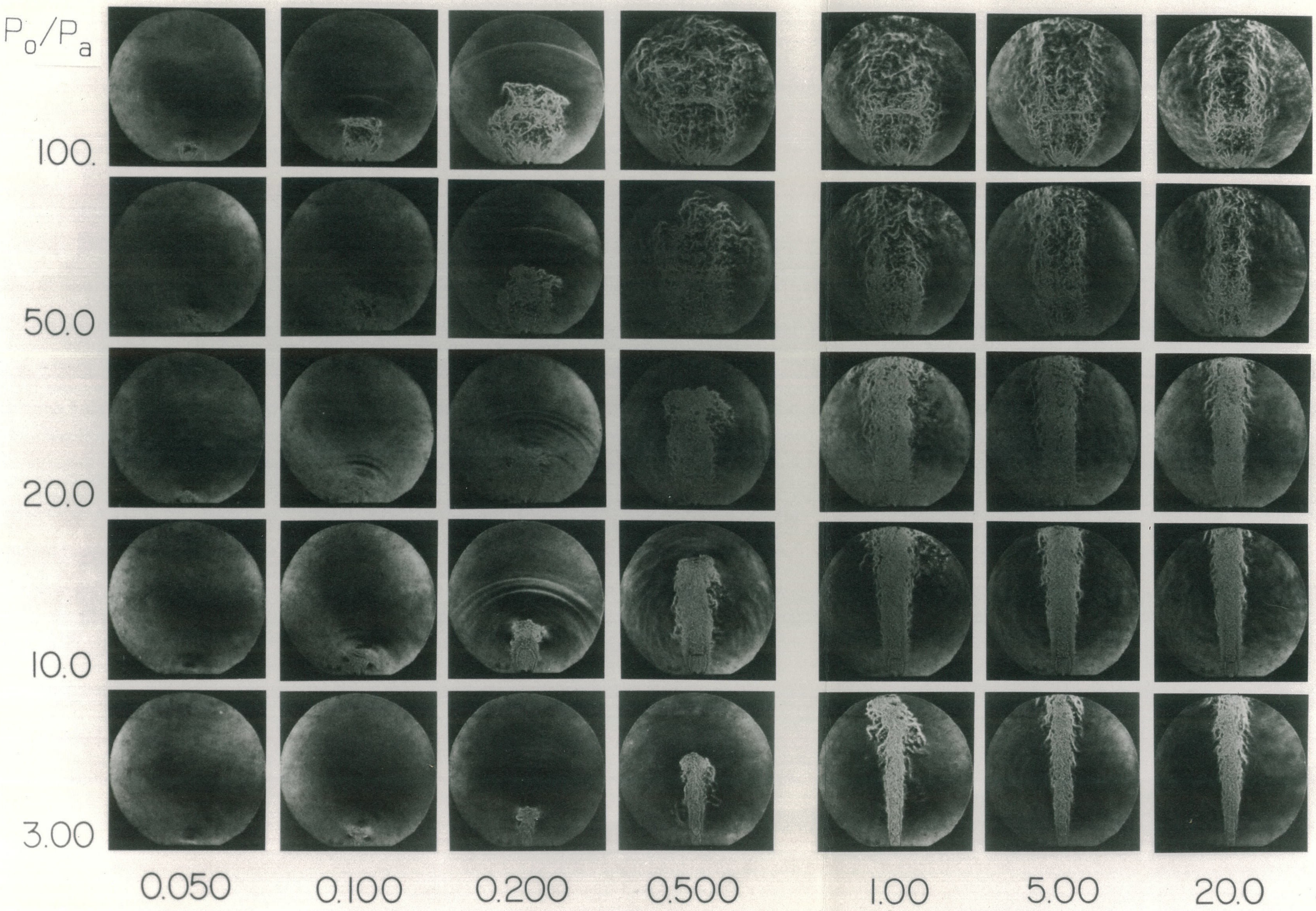

Figure 3.4 – $SF_6 \rightarrow N_2$

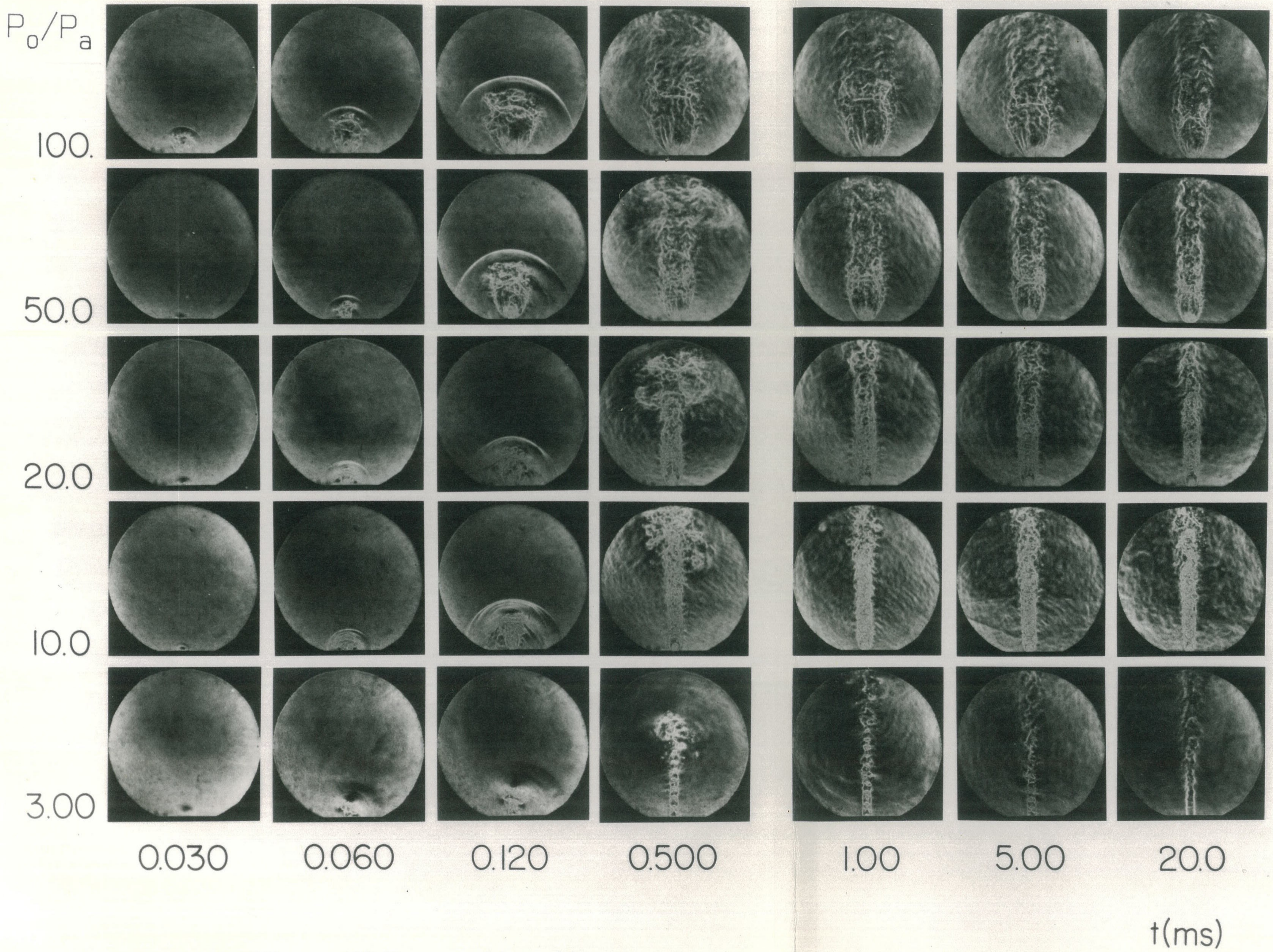

Figure 3.5 — $N_2 \rightarrow N_2$

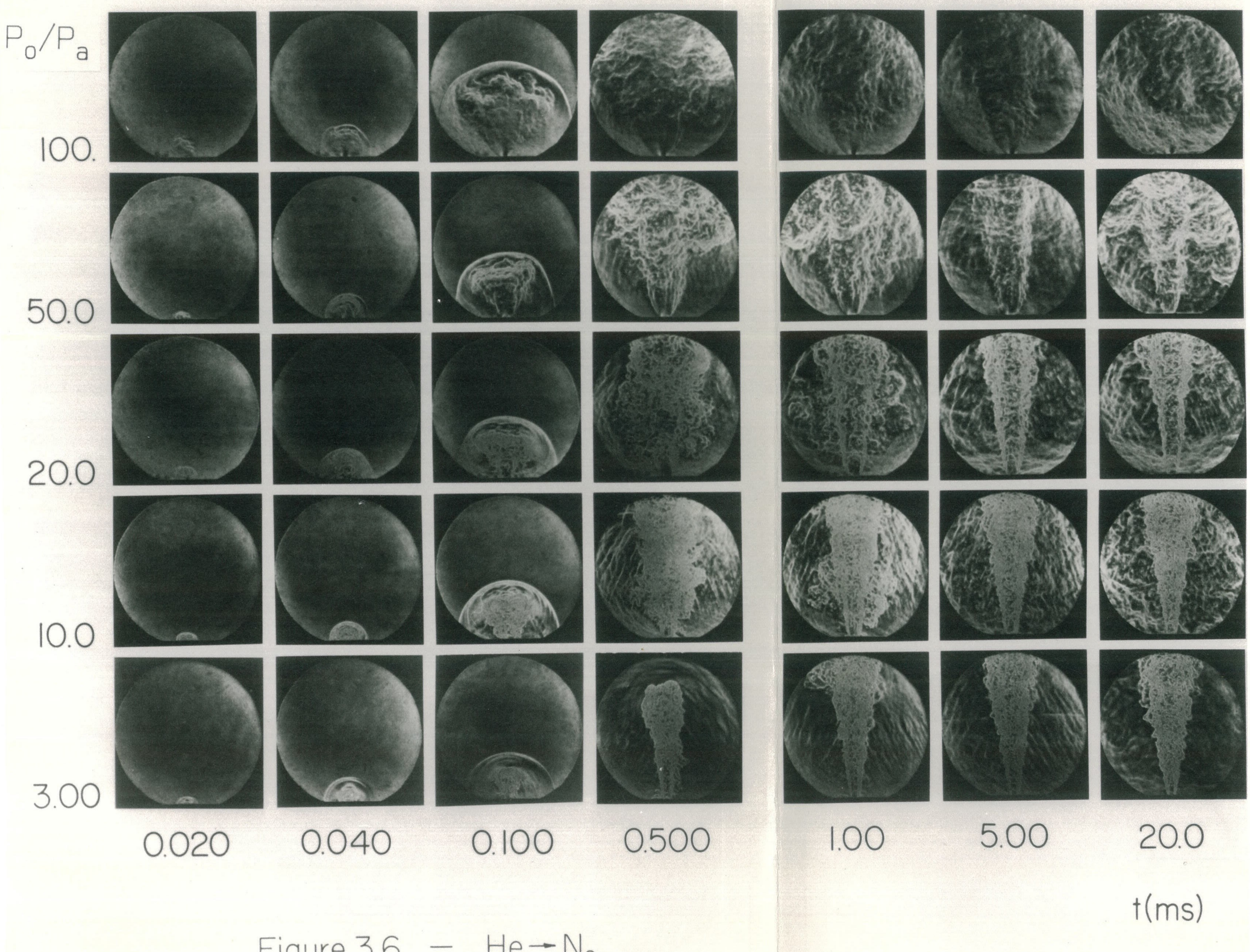

Figure 3.6 — He → $N_2$

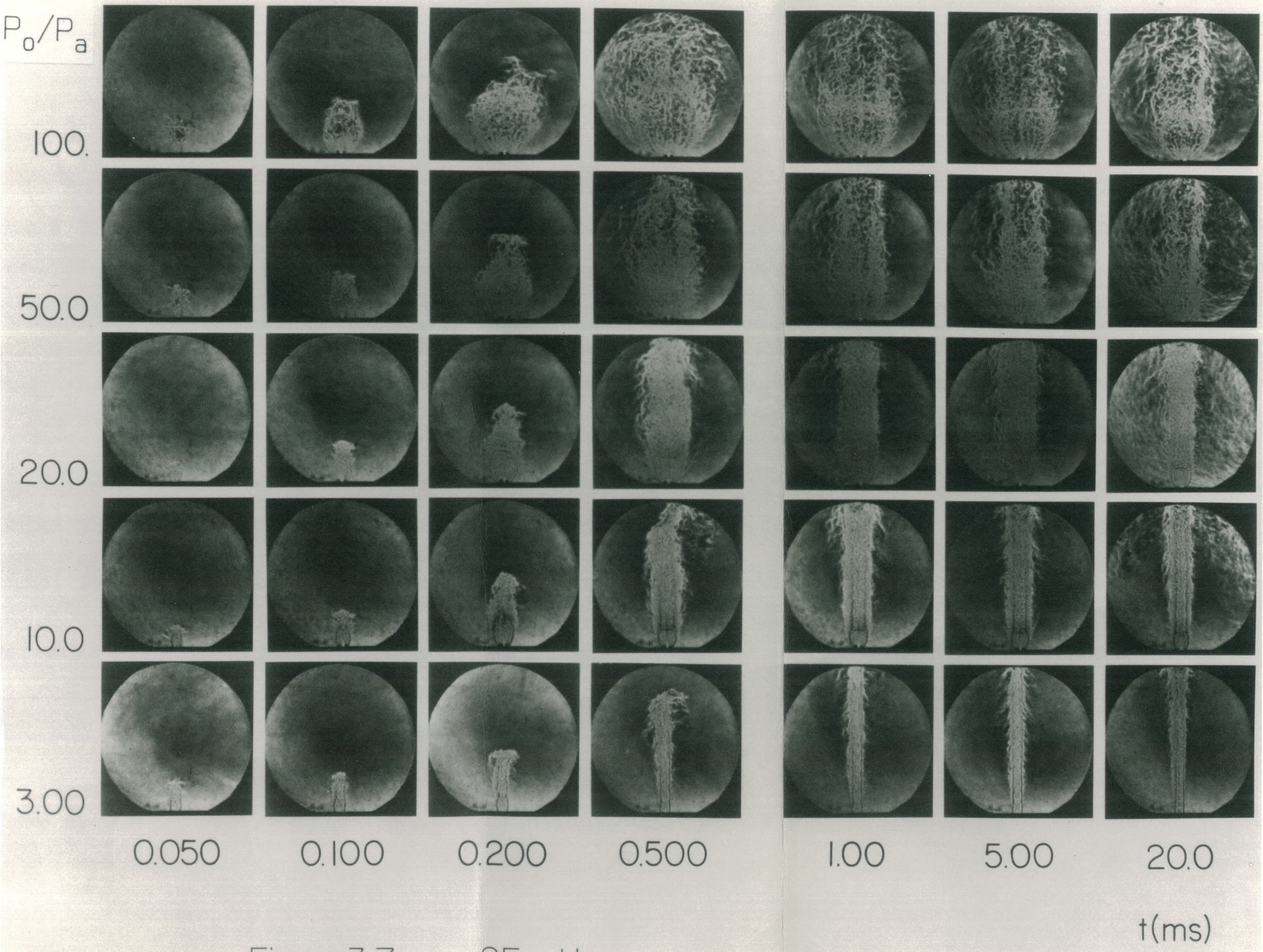

Figure 3.7 — $SF_6 \rightarrow He$

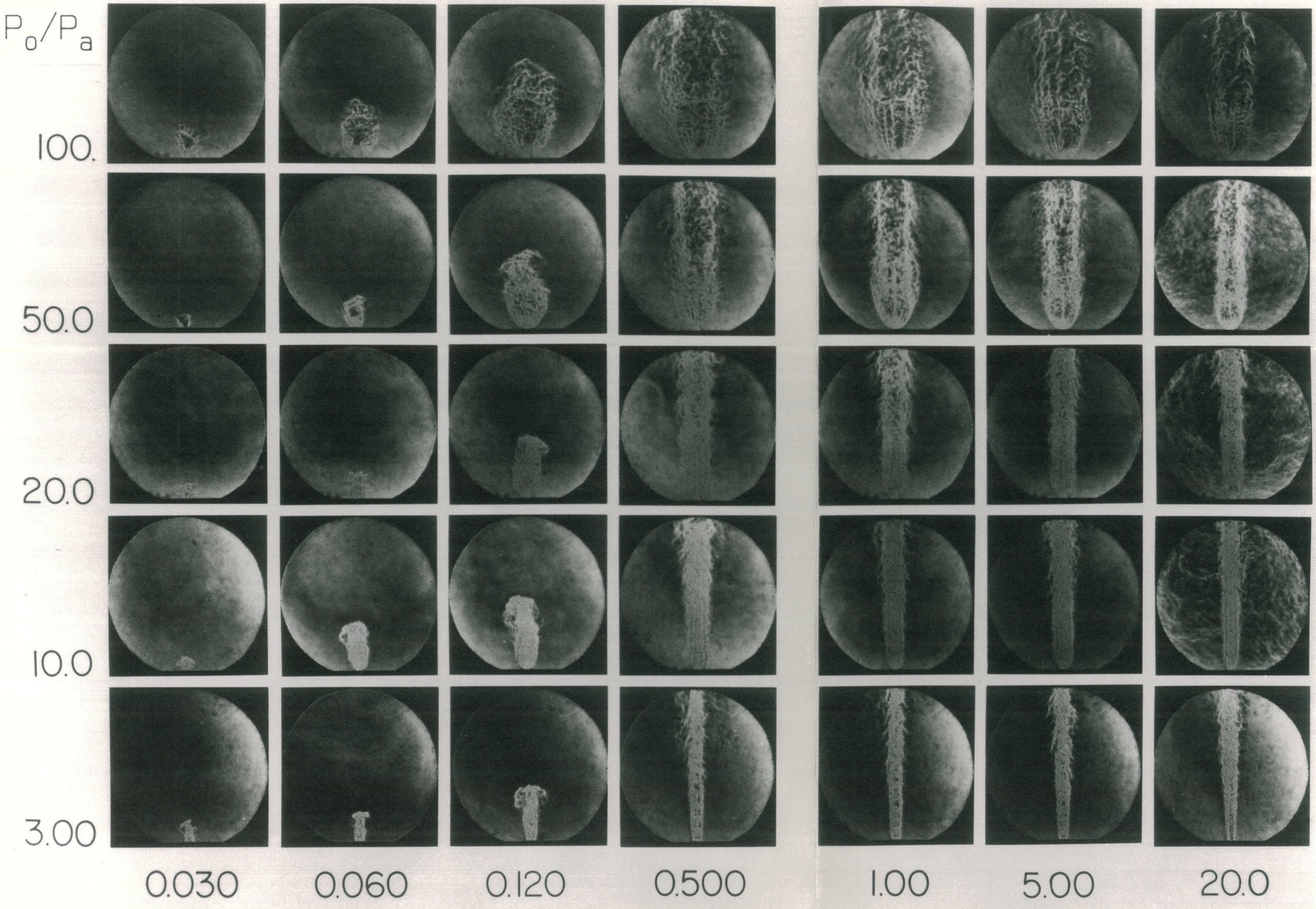

Figure 3.8 — $N_2 \rightarrow He$

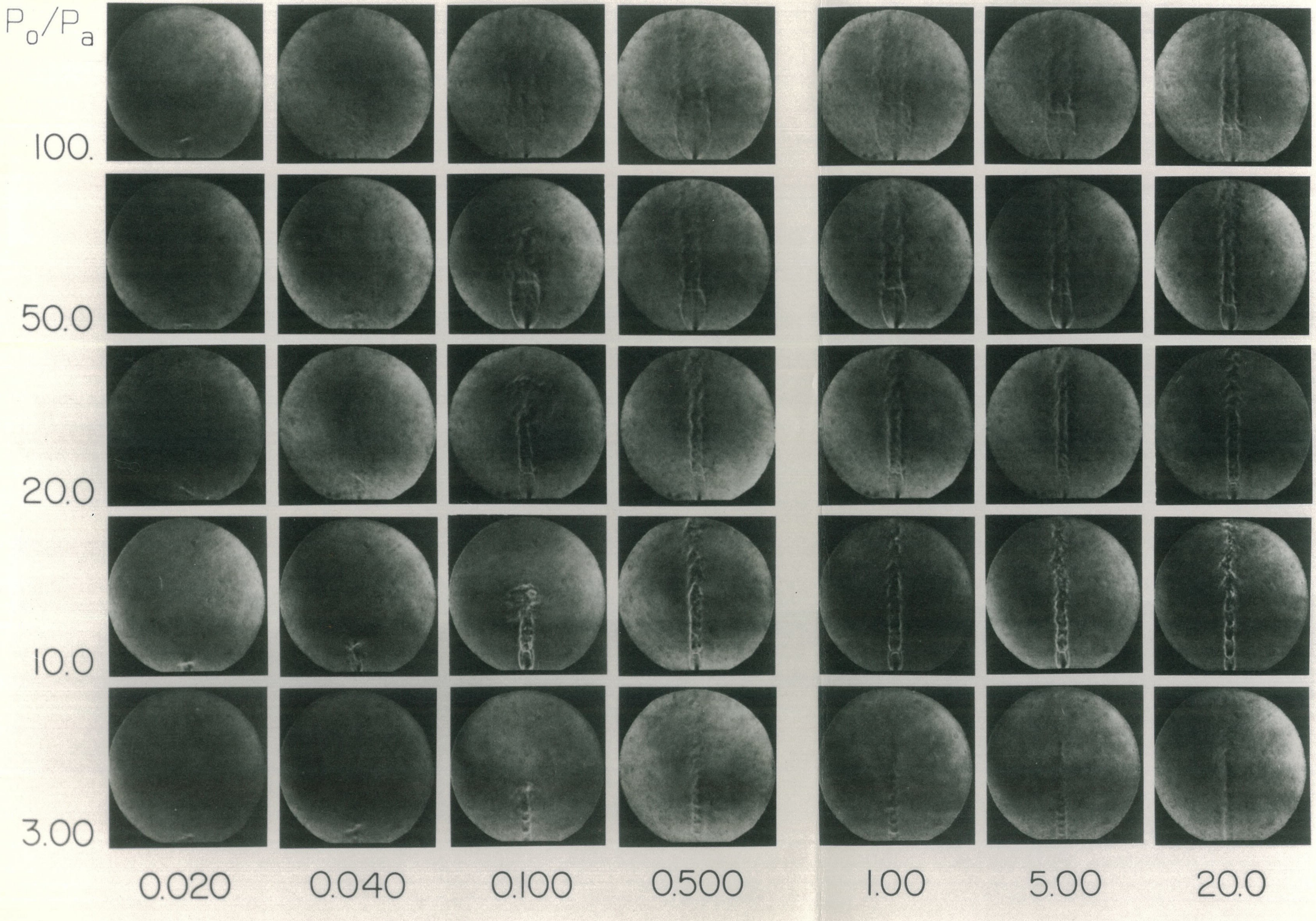

Figure 3.9 — He → He

## Chapter 4

## EXPERIMENTAL RESULTS FOR MACH DISK

### 4.1. Introduction.

This chapter presents the results of experiments that were carried out to determine the time evolution of the Mach disk and barrel shock, and the effect of the pressure ratio on the location of the Mach disk and barrel shock. A series of line drawings of the Mach disk and barrel shock, as well as time histories of the position of the Mach disk are also included. The location of the Mach disk oscillates for the case of a finite reservoir due to fluctuations of $P_o$, and the frequency of vibration is found to depend on the jet gas.

The experiments were carried out using all gas combinations: From the nine possible cases, the interior of the jet is visible in seven, while it is obscured by the turbulent shear layer in the other two cases. The results are organized to show (a) the wave structure, and (b) the Mach disk location.

### 4.2. The Wave Structure.

In previous work, Schmidt & Shear (1974) showed that for the precursor flow of a muzzle blast, the location and shape of the barrel or intercepting shock is invariant with time, the only time dependence being in the length or extent of the shock (figure 4.1). As shown in figure 4.1, this is approximately the case for our low pressure ratio $N_2 \rightarrow N_2$ case, in which the barrel shock grows axially. However, this observation is not valid for other gas combinations and higher pressure ratios. In figure 4.2, $SF_6$ jets show the largest lateral growth. This is related to the low value of $\gamma_o$ in $SF_6$. The lower the value of $\gamma_o$, the larger the expansion angle at the jet exit, thus causing the observed lateral growth. Even $N_2$ jets at high pressure ratio grow laterally. Figure 4.2 contains a series of line drawings illustrating the time evolution of the Mach disk and the barrel shock. The

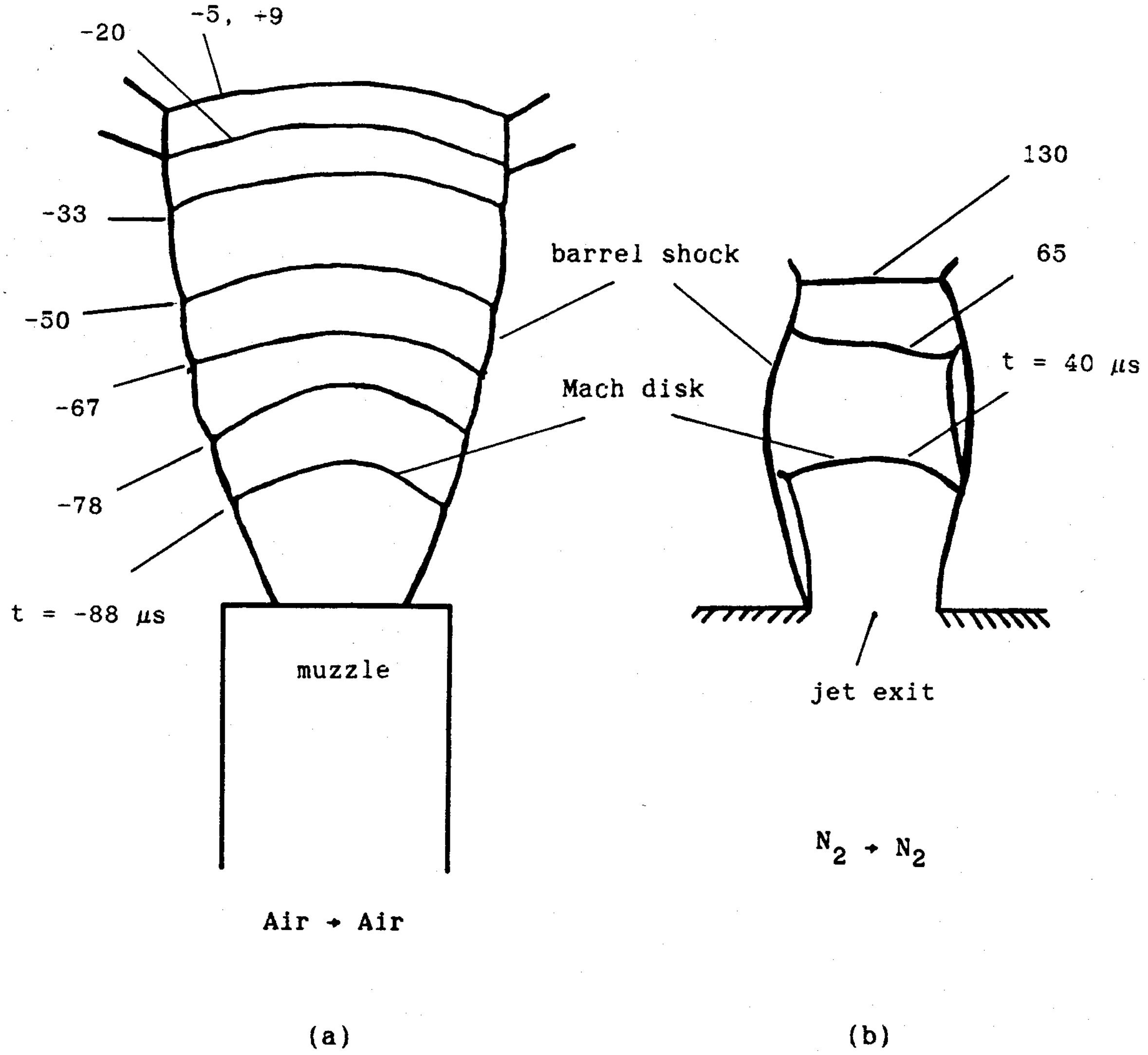

Figure 4.1 Evolution of the normal and oblique waves at equal pressure ratios ($P_o/P_a$ = 15) (a) muzzle blast (taken from Schmidt & Shear, 1974) and (b) the corresponding case from present work.

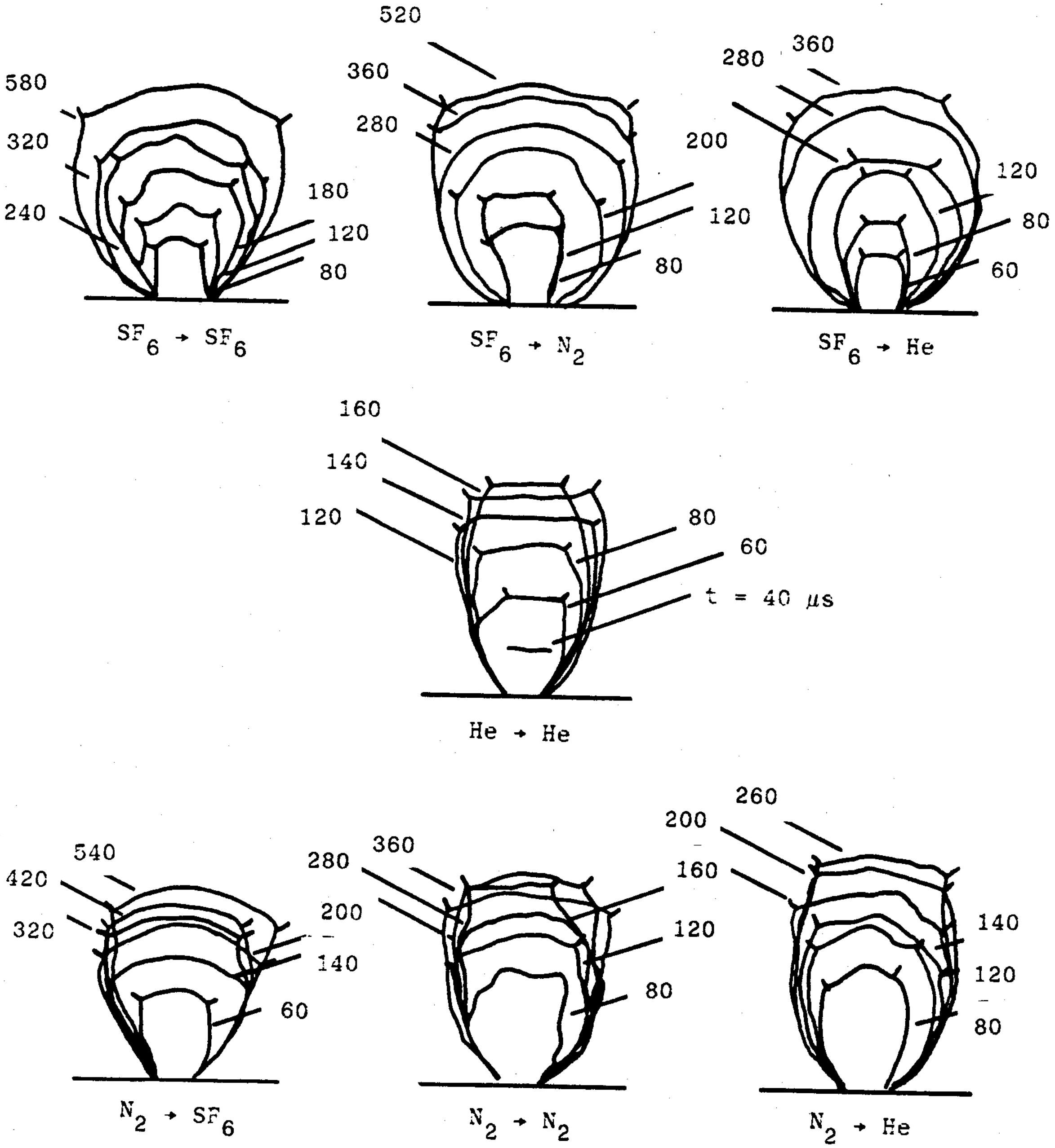

Figure 4.2 Time development of the Mach disk and the barrel shock for several gas combinations at $P_o/P_a = 100$.

structures are shown at typical times between the first appearance of the shocks and later times when the structures are quasi-steady. In general they are deformed during the initial start-up of the jet and exhibit a more well-defined shape during the quasi-steady phase. During the initial propagation of the Mach disk and barrel shock, the observed lateral growth is caused by the increasing exit pressure. This is caused by more plume as a result of the pressure ratio influence on the Prandtl-Meyer expansion angle.

The barrel shock wave has a bulbous appearance for heavy jets and is more slender for light jets, again, because of the low value of $\gamma_o$ for the heavy gases used in the experiments. At early times, when the exit pressure is still low, heavy jets also exhibit a slender structure. Indeed partially-developed early time low pressure cases and quasi-steady low pressure cases are more slender than the higher pressure cases. This observation is confirmed in figure 4.3, which shows shock structures after the flow becomes quasi steady at different pressure ratios. For the lowest pressure ratios the downstream structure has a different appearance than the others. This is caused by the repetitive diamond-shaped cell structure for the low pressure ratio cases, that was mentioned earlier. The "M" shaped wave at the lowest pressures in figure 4.3 is the beginning of the repetitive diamond structure.

### 4.3. The Mach Disk Location.

The time evolution of the Mach disk location was obtained from high speed movies for the seven different cases mentioned above. All the cases involving the highest pressure ratios showed features that were pressure-ratio dependent. The results are plotted together with the prediction from the relations for steady jets developed empirically by Ashkenas & Sherman (1966) in figures 4.4 to 4.6. The dependence of the Mach disk location on pressure ratio is discussed in Appendix D. The Mach disk first forms a few jet diameters downstream of the exit. As the jet exit pressure increases, the Mach disk moves downstream. It

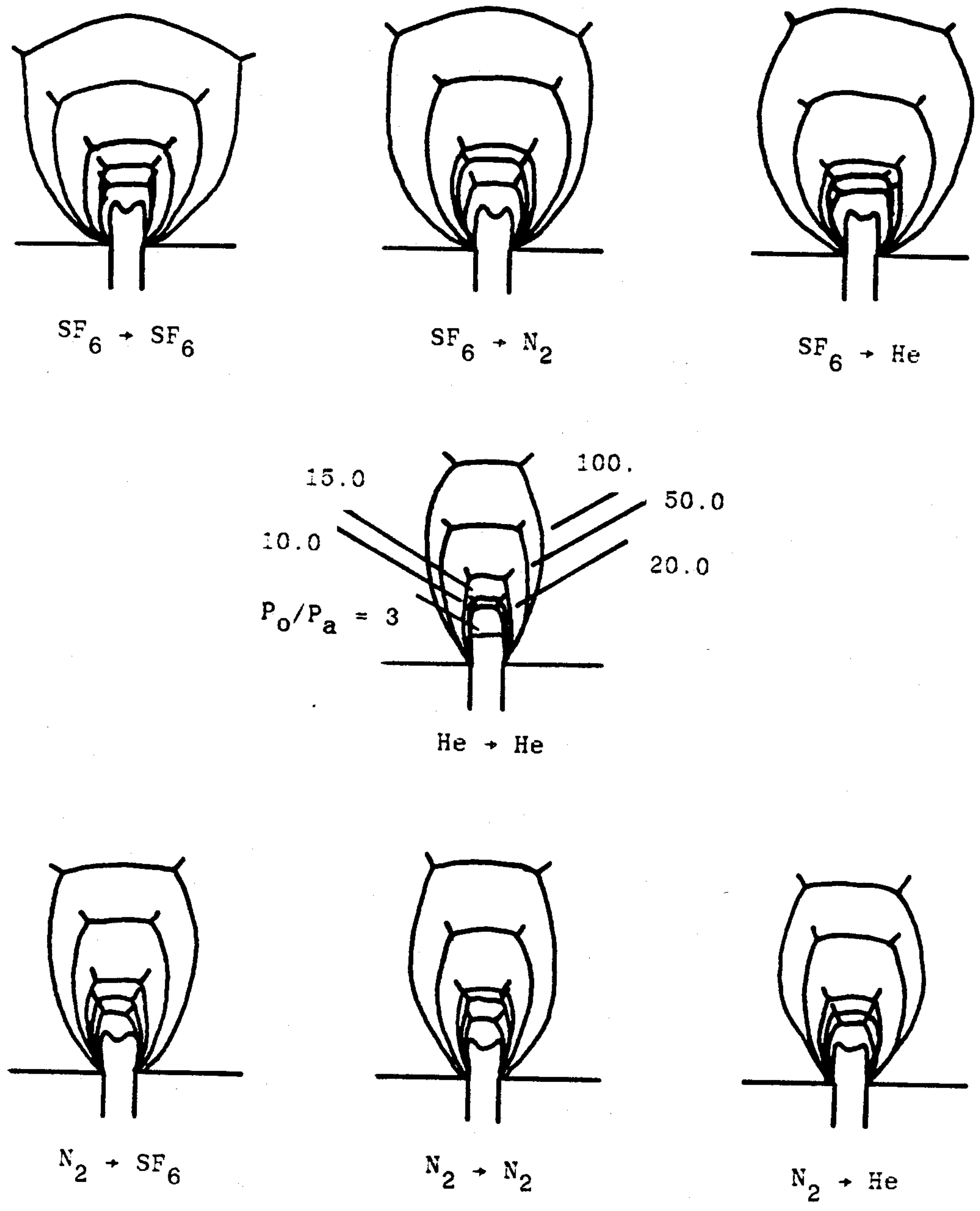

Figure 4.3 Influence of pressure ratio on the shape of the fully-developed Mach disk and barrel shock at t = 500 $\mu s$.

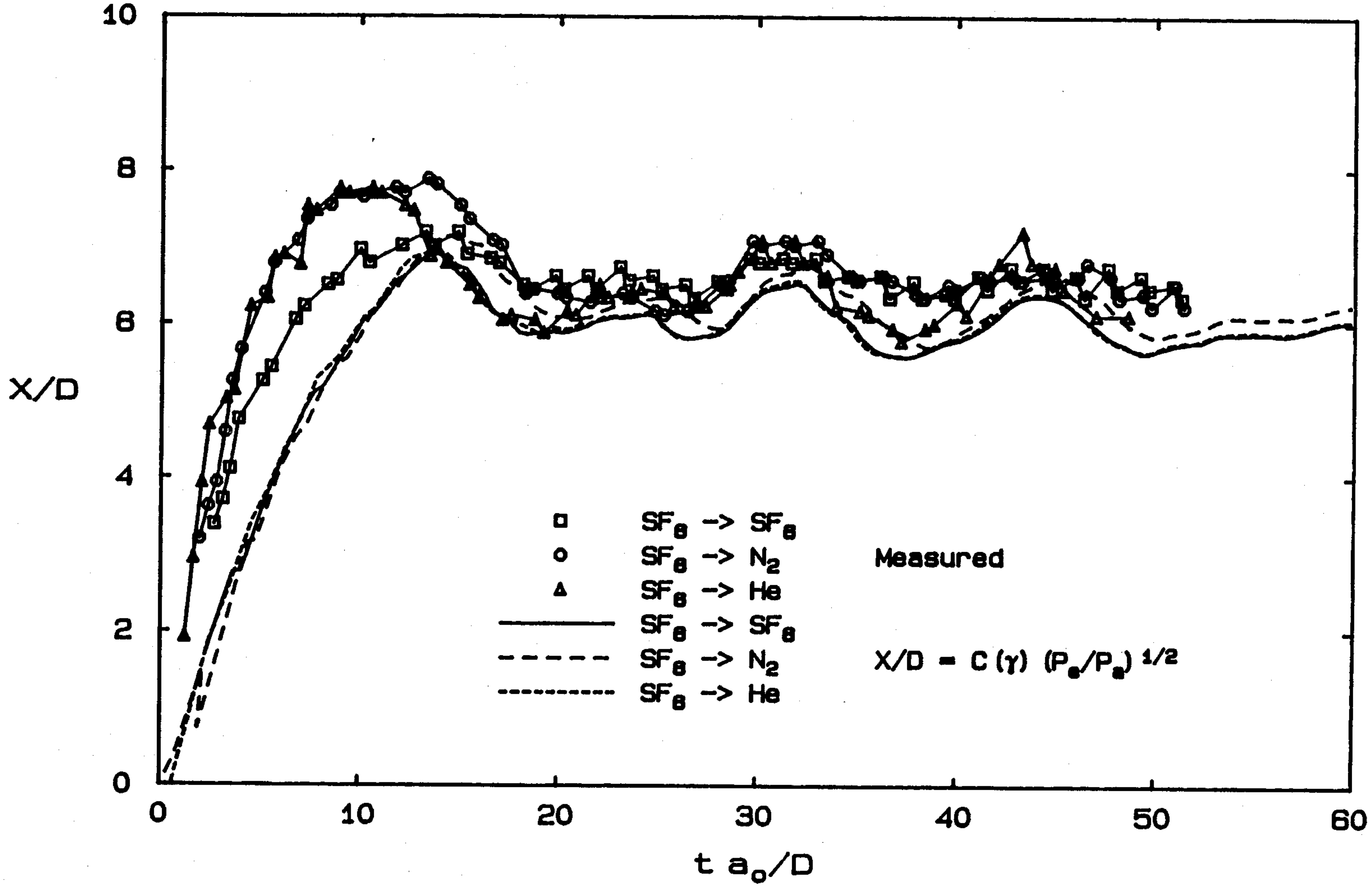

Figure 4.4 The evolution of the Mach disk for $SF_6$ jets at $P_o/P_a = 100$.

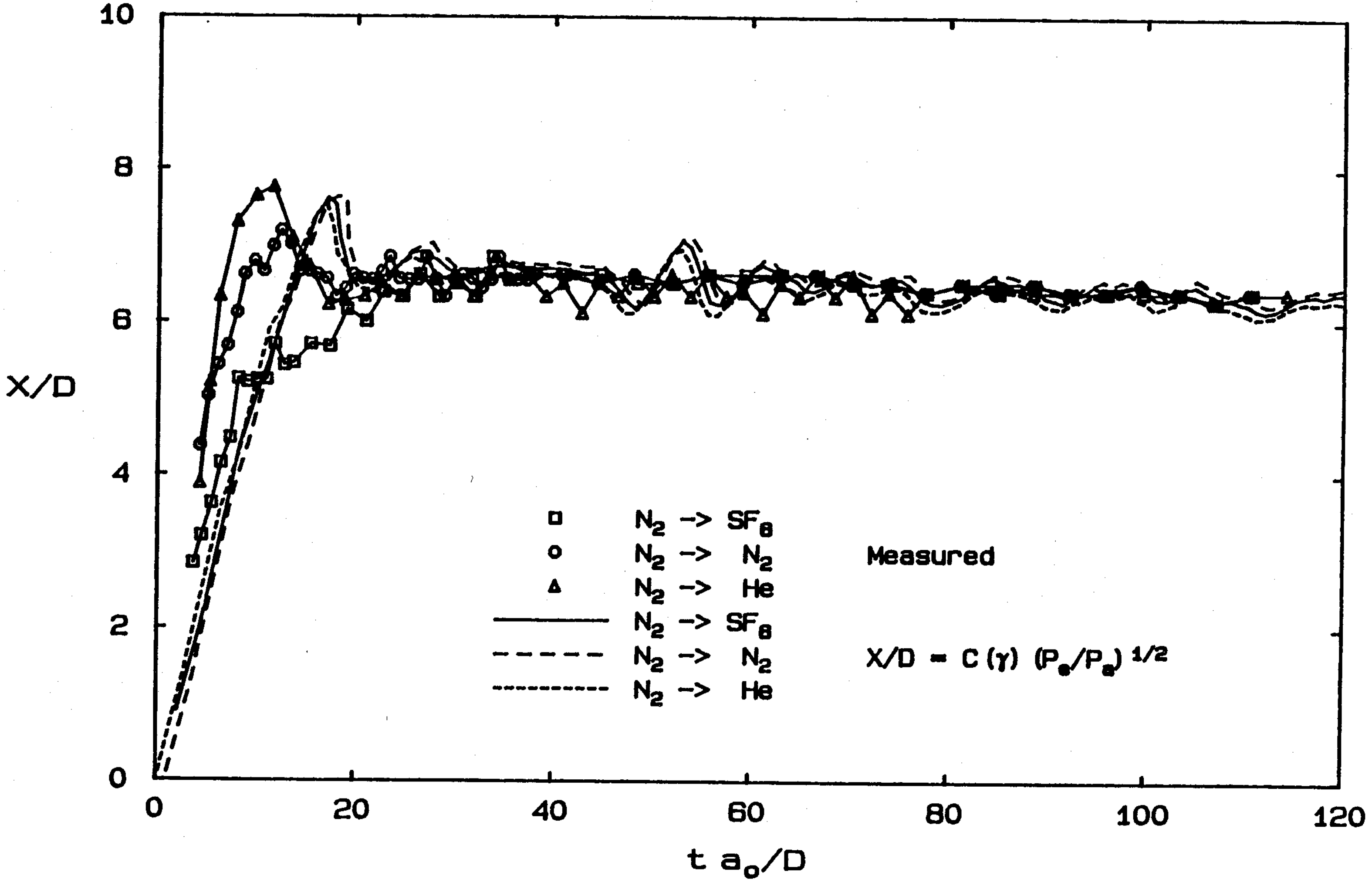

Figure 4.5 The evolution of the Mach disk for $N_2$ jets at $P_o/P_a = 100$.

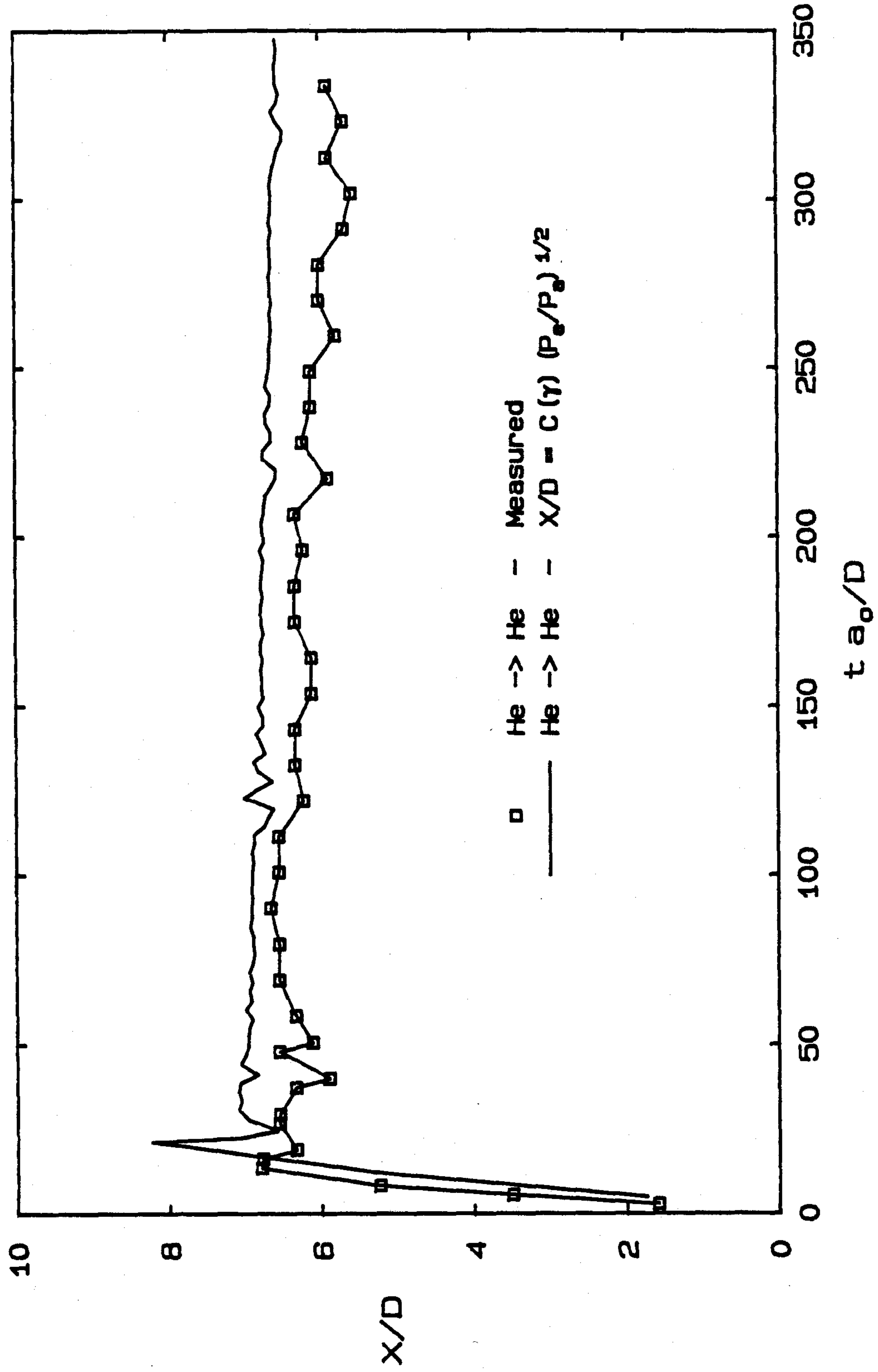

Figure 4.6 The evolution of the Mach disk for He jet at $P_o/P_a = 100$.

oscillates about its final location, with an amplitude that increases with pressure ratio and $W_0$. For pressure ratios lower than 10 there is no detectable vibration of the Mach disk. The Ashkenas-Sherman equation includes the effect of the ratio of reservoir to ambient pressure, and is independent of the gases used. Since the exit pressure was measured in the present experiments, a factor was included in the Ashkenas-Sherman equation to convert the reservoir pressure to exit pressure. The figures show that the quasi-steady theory underestimates the distance from the exit to the Mach disk during large time for quasi-steady heavy jets (figure 4.4) and overestimates it for light jets (figures 4.5, 4.6). This disagreement is not understood yet.

In figures 4.4 to 4.6 the Mach disk location was predicted by using the empirical result of Ashkenas & Sherman but was shifted by the time that the waves would take to propagate from the jet exit to the instantaneous location of the Mach disk. This was done since the oscillations could result from waves emanating from the reservoir. Computations showed that this interval of time is of the order of the jet flow time ($D/a_0$). The agreement of the oscillations about the Mach disk location during the quasi-steady phase c.f. figure 4.4, suggests that the Mach disk oscillates due to changes in exit pressure. A compression wave increases the strength of the Mach disk, causing the equilibrium position to be further downstream, whereas an expansion wave induces the opposite behavior. The oscillation of the Mach disk between these two positions is the observed result. For the unsteady initial propagation of the Mach disk this prediction fails, because the Mach disk moves faster than expected from exit pressure estimates. The departure of the experimental Mach disk location from the theoretical result cannot be explained by diaphragm opening because to get agreement, the effective diameter is always larger than the actual diameter. Improved predictions for the initial propagation of the Mach disk were obtained by the non-shifted pressure trace shown in figure 4.7. The exit pressure traces for a given jet gas are similar, independent of the ambient gas. For early times the discrepancies observed are probably caused by

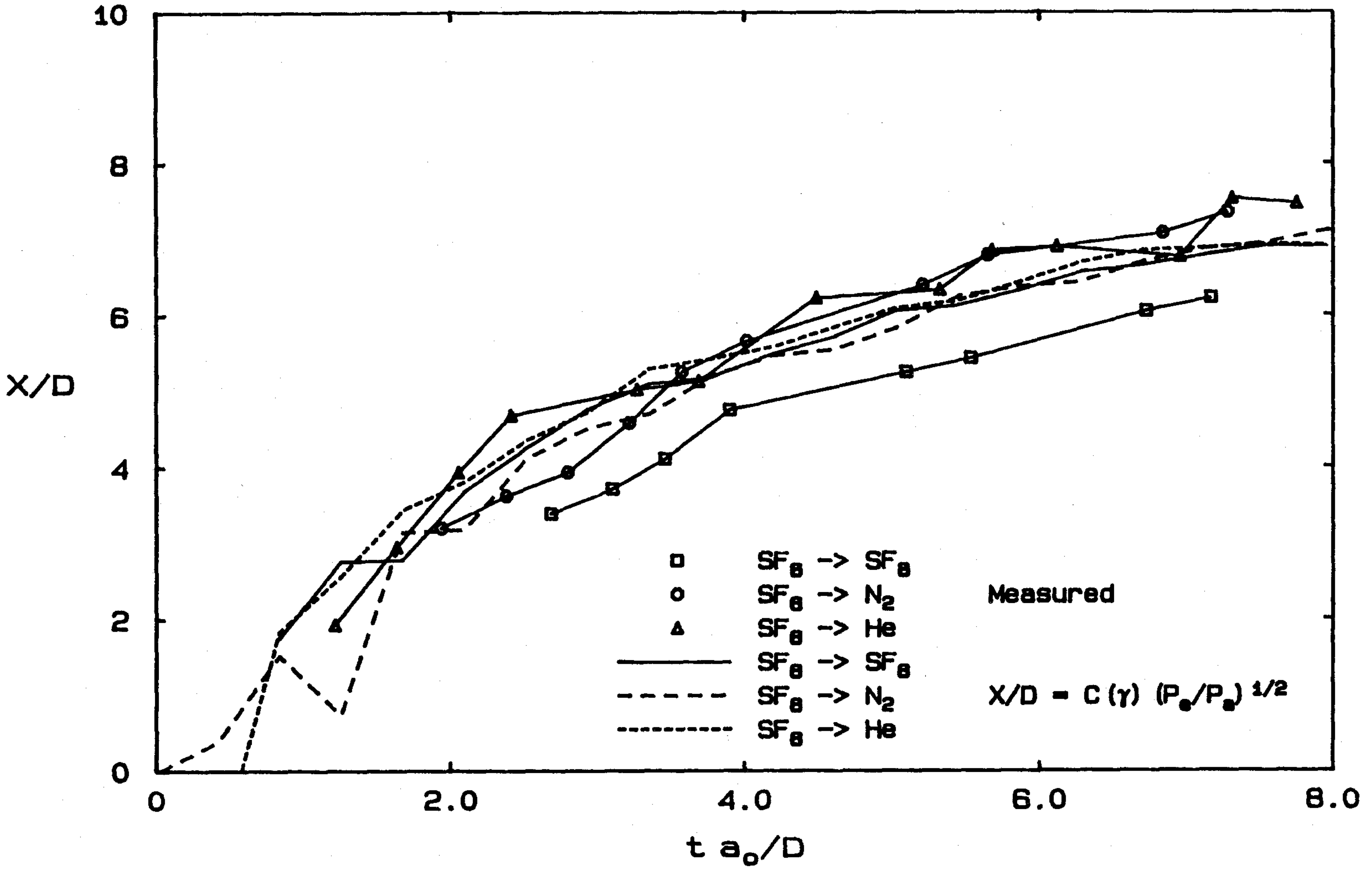

Figure 4.7 The initial evolution of the Mach disk for $SF_6$ jets at $P_o/P_a = 100$.

slight differences in the way that the diaphragm breaks each time.

The oscillation frequencies are shown in Table 4.1. The fundamental frequency ($\omega_{fund}$) of the reservoir was obtained by assuming that nodes are formed both at the bottom of the reservoir, due to a solid wall, and at the jet exit, because the exit area is much smaller than the reservoir cross section.

Table 4.1 Frequencies for the Mach Disk Oscillation

| Gas Combination | $\omega_{fund}$ (kHz) | $\omega_{M.d.}$ (kHz) |
|---|---|---|
| $SF_6 \rightarrow SF_6$ | 1.45 | 1.96 |
| $SF_6 \rightarrow N_2$ | 1.45 | 2.06 |
| $SF_6 \rightarrow He$ | 1.45 | 2.11 |
| $N_2 \rightarrow SF_6$ | 1.24 | - |
| $N_2 \rightarrow N_2$ | 1.24 | 3.98 |
| $N_2 \rightarrow He$ | 1.24 | 3.75 |
| $He \rightarrow He$ | 1.24 | 1.30 |

This is equivalent to assuming that the wavelength of the observed pressure oscillations is twice the length of the reservoir. The frequencies of oscillation of the Mach disk location ($\omega_{M.d.}$) were found by counting the number of periods within an interval of time in figures 4.4 to 4.6; they are dependent only on the jet gas and have values close to the resonant frequency of the reservoir. For heavy jets the frequency is close to the fundamental value for the reservoir. For the lighter jets, the oscillations are much less distinct, but for $N_2$ jets the most prominent frequency approximates the third harmonic, and for He jet it seems close to the the fundamental. The time taken by the Mach disk to reach the furthest position increases with both jet and atmosphere densities. For $N_2 \rightarrow SF_6$ Mach disk oscillation does not occur, although oscillations in the pressure are still observed.

# Chapter 5

# EXPERIMENTAL RESULTS FOR JET HEAD

## 5.1. Introduction.

In this chapter, experimental results are reported to illustrate the formation of the jet head. A selection of high speed photographs obtained by the spark and the high speed movie technique, are presented to illustrate the time dependence of both the head volume and head location.

It will be shown that the shape of the jet head depends on gas combination and pressure ratio. The results are organized to illustrate (a) the formation of the jet head, and (b) the development of the jet head.

## 5.2. The Formation of the Jet Head.

The gas at the front region of the jet head flows at a velocity that decreases with time. The more energetic fluid behind tends to push aside the slow moving gas, causing the slower gas to move upstream relative to the jet. The shape of the head depends on gas combination and pressure ratio, as illustrated in the nine figures in Chapter 3. Often the jet head takes on interesting shapes; some of these will be discussed here.

For jets with small density contrasts, other than the heavy into light gas combinations, the head may show up as a well defined vortex ring whose size and appearance is pressure ratio dependent. The sequence of pictures shown in figure 5.1 demonstrates how the pressure ratio influences the formation of the vortex ring for the case of $SF_6 \rightarrow SF_6$. For the smallest pressure ratio the shape of the head is nearly spherical, but as the pressure ratio increases, the similarity to a vortex ring becomes more apparent. The formation of a spherical head at lower pressure ratios is probably caused by the way that the

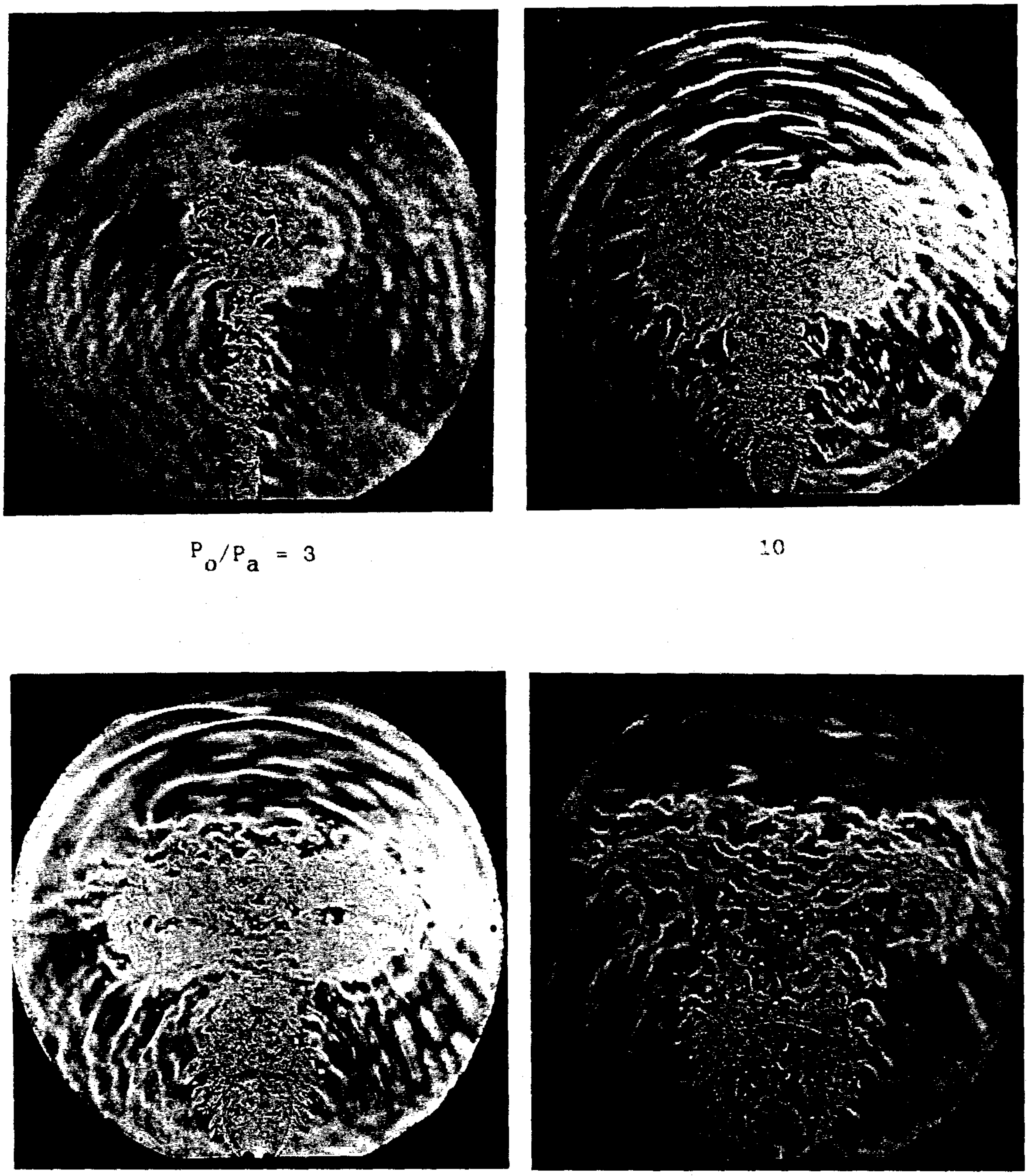

$P_o/P_a = 3$

10

20

50

Figure 5.1 Effect of pressure ratio on vortex ring generation for $SF_6 \rightarrow SF_6$ at equal times ($ta_o/D = 20$).

diaphragm breaks, or the high inertia effect of the atmosphere. For medium pressure ratios the entrainment is larger and a vortex ring is formed. A vortex ring with well defined side lobes and a core which appears as dark spots at the center of the two side lobes, can be clearly seen at a pressure ratio of 20. At higher pressure ratios mixing becomes more violent, and the shape of the head becomes diffuse and is less well defined.

Figure 5.2 shows the development of the head of a single jet taken from a movie for $N_2 \rightarrow N_2$. The initial shape of the head for this jet at $ta_0/D = 17$ is similar to that for $SF_6 \rightarrow SF_6$ jet at $P_0/P_a = 3$ as shown in figure 5.1. However in this case note that nonsymmetric vortex rings develop at later times. This asymmetry occurs because one of the side lobes moves faster than the other, indicating that the speed of propagation is not equally distributed along the vortex core, or, equivalently, that the strength of the ring is not uniformly distributed. Since random perturbations cause larger displacements in light jets than in heavy jets, the formation of asymmetric vortex rings or recirculating regions is more likely to occur in light jets. In this case, rotating the position of the transducer at the jet exit by $180^o$, also rotates the jet head. Many examples of asymmetric jet heads involving light into heavy combinations can be seen in Chapter 3.

The unsteady propagation of the jet head generates a field of pressure waves in the atmospheric gas between the bow shock and the jet head. These pressure waves propagate away from the jet head and overtake the bow shock, as shown in figure 5.3. The figure also shows that in some cases, the jet head has a dimple, giving it a double-headed appearance. A normal shock wave located four exit diameters downstream of the Mach disk can just be seen in the interior of the jet. The double-headed appearance seems to be related to this normal wave and is found in other light jets in Chapter 3. This characteristic was originally predicted in pressure matched jets by Smith et al. (1984) in which hydrodynamic simulation was used to model hot spots in radio

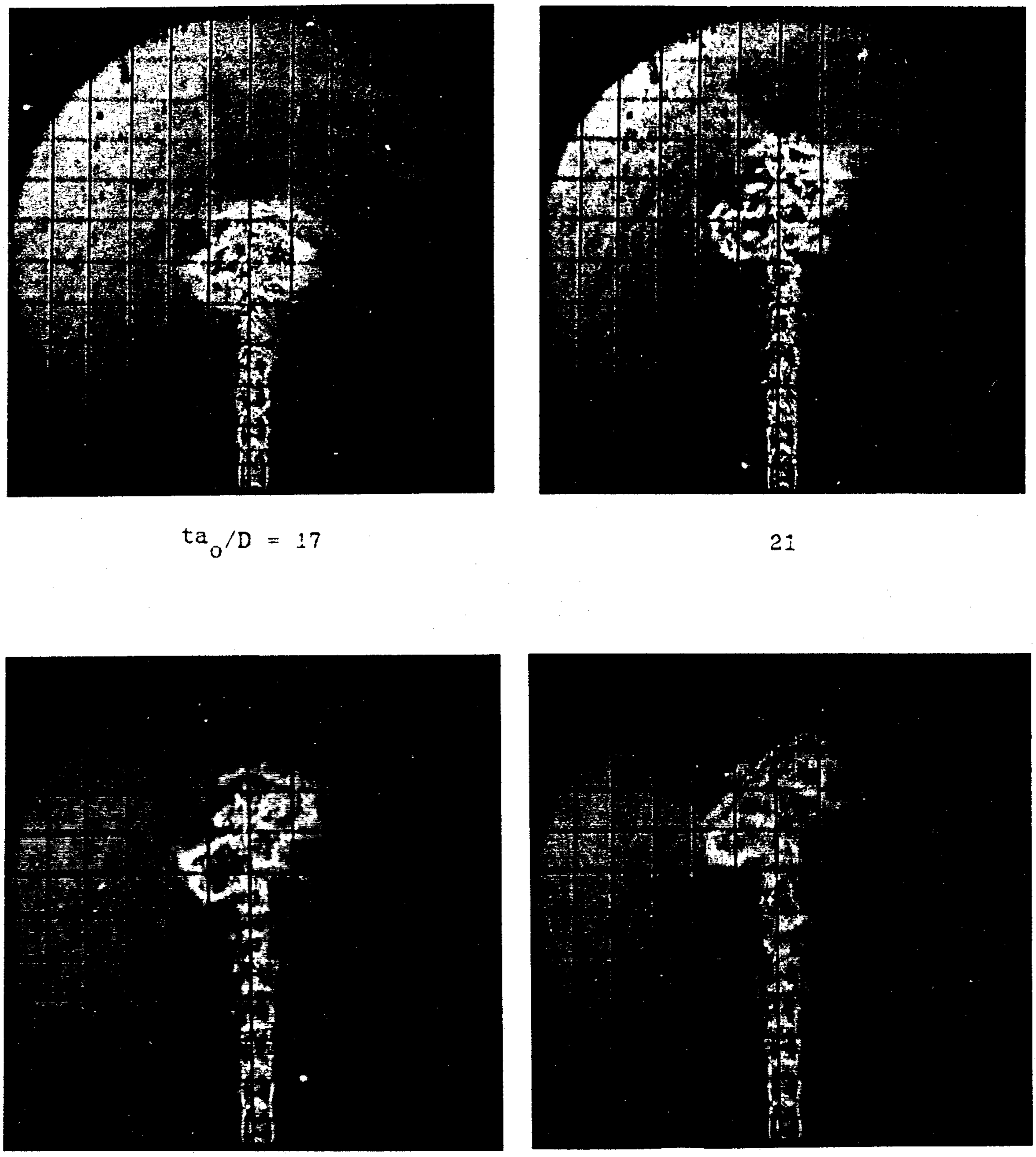

$ta_o/D = 17$ 21

24 28

Figure 5.2 Development of the asymmetric vortex ring for $N_2 \rightarrow N_2$ at $P_o/P_a = 3$

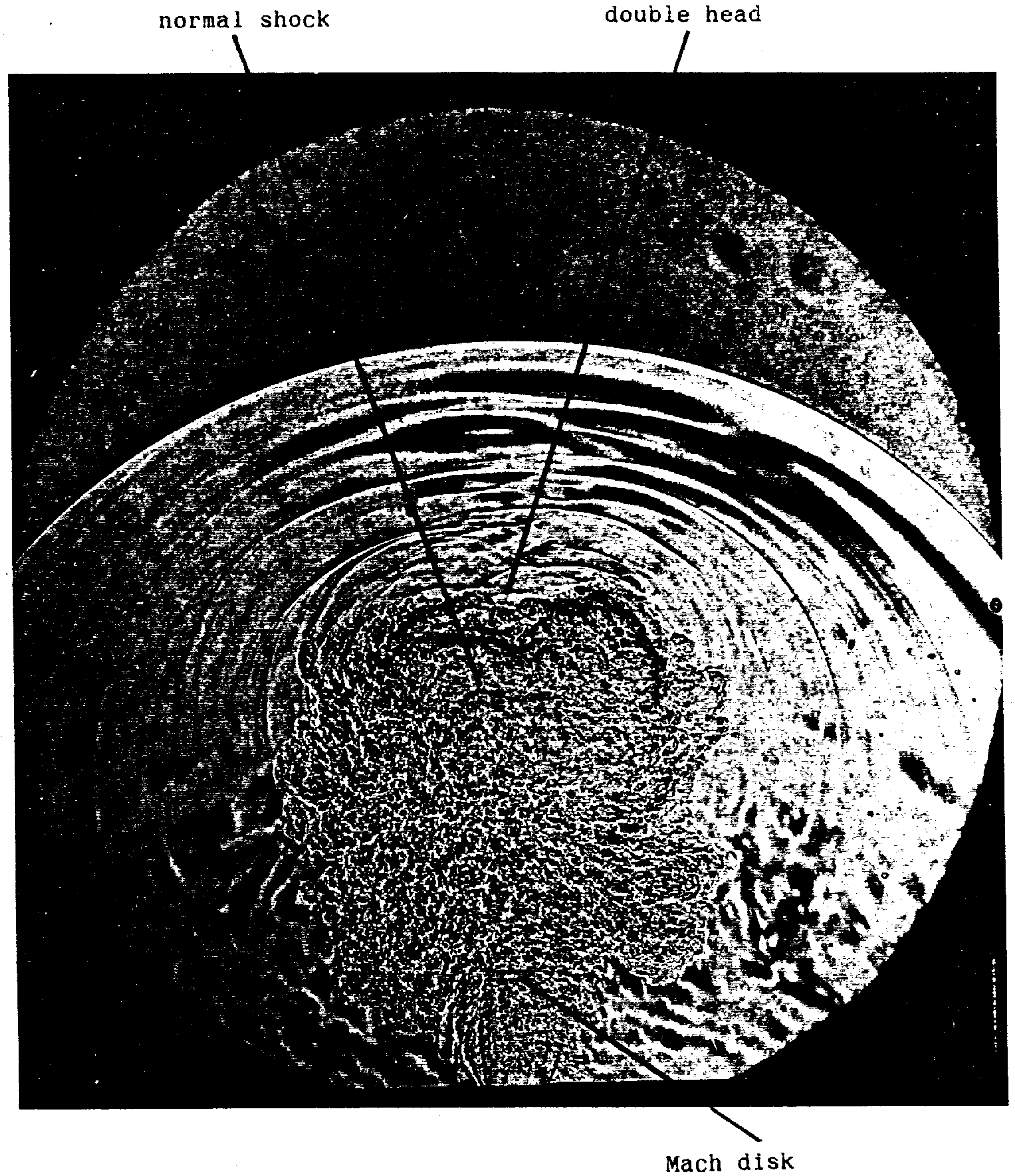

Figure 5.3 The formation of a double head on the $N_2 \rightarrow SF_6$ jet at $P_o/P_a = 10$ and t = 500 $\mu$s

galaxies. A line plot from their work which clearly shows the indentation at the center of the head, is presented in figure 5.4. The figure shows contours of gas density differing by 20%. The formation of compression waves upstream of the jet frontal boundary is exhibited by the high concentration of density contours.

The experimental data indicate that the volume of the jet head depends on the gas combination and pressure ratio. Two cases showing heavy into heavy and light into heavy combinations are highlighted in figure 5.5. The size of the $SF_6$ jet head is much smaller than that of the He jet and it remains fairly constant with time, while the volume of the He head increases substantially with time. The difference between the two gas combinations is probably caused by the damping effect of the atmosphere. For the first case, the momentum flux effect of the jet predominates and a ballistic jet forms behind the spherical head. The second case exhibits a higher damping effect, however, the momentum flux of the jet is not as great as in the first case to form a ballistic jet. Consequently, the jet head grows laterally giving the jet a pronounced expanded appearance.

### 5.3. Development of the Jet Head.

High speed movies showed the jet evolution for four different gases into $SF_6$. Each movie provided a sequence of frames from which the volume that confines the jet head could be measured for times ranging from $ta_o/D = 1$ for $SF_6 \rightarrow SF_6$, $P_o/P_a = 3$ to $ta_o/D = 120$ for $He \rightarrow SF_6$, $P_o/P_a = 3$. Figure 5.6 shows the normalized volume of the jet head as a function of time. The reference volume ($V_{ref}$) was taken to be the volume of a cylinder ($V_{cil}$), whose base and height are each one exit diameter in length, multiplied by the pressure ratio. Normalization with pressure ratio brought the two cases of $He \rightarrow SF_6$ together because mass flux is proportional to pressure ratio; these two cases exhibited similarly growing jet heads. It should be noted that this normalization also brings closer the data for jets of different gas combinations and different pressure ratios especially $SF_6 \rightarrow SF_6$ and $N_2 \rightarrow SF_6$. The

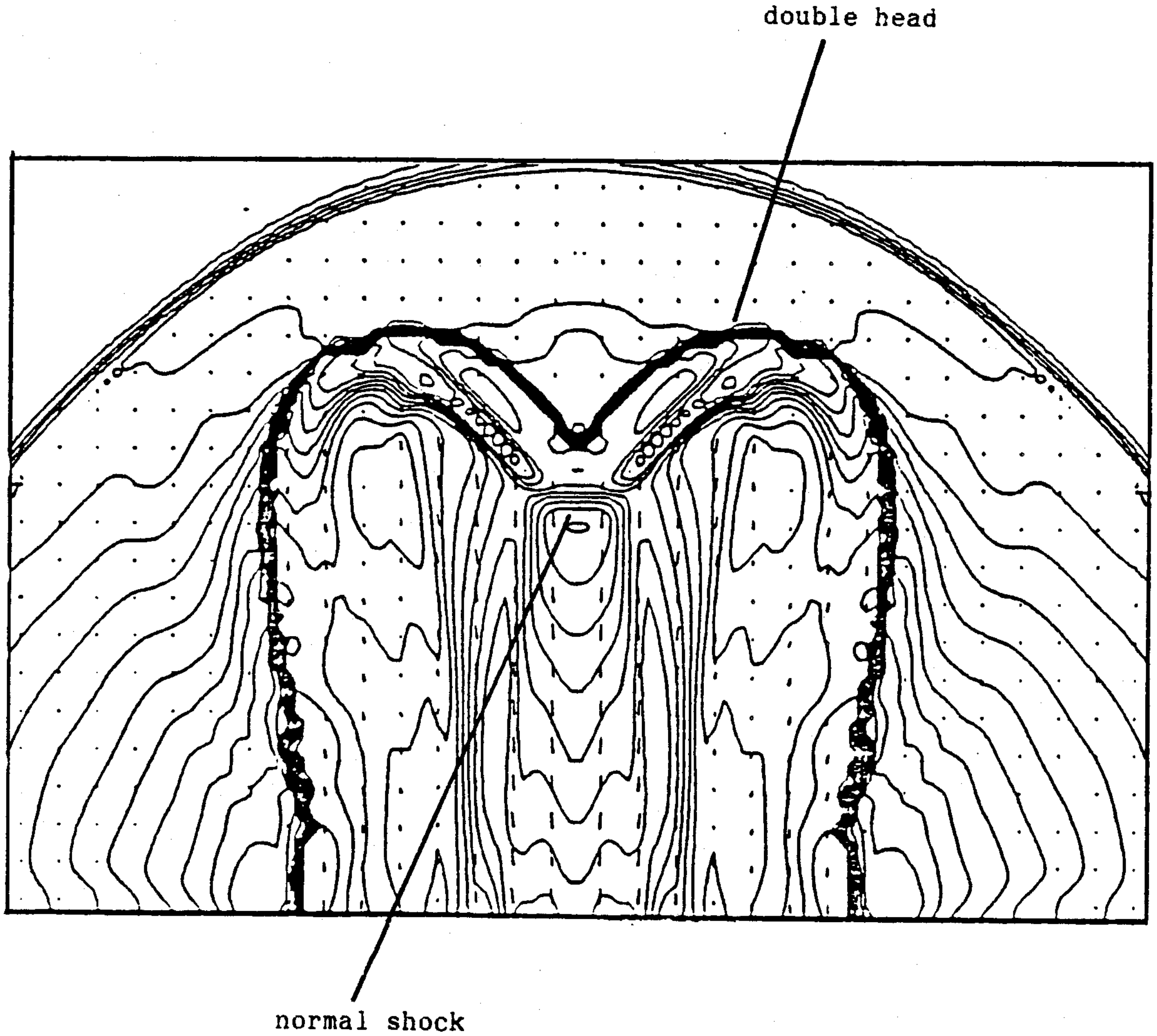

Figure 5.4 Density contours for the pressure matched jet: $\rho_o/\rho_a = 0.1$, $ta_a/D = 14$ and $u_{head}/a_o = 6$ (from Smith et al, 1984).

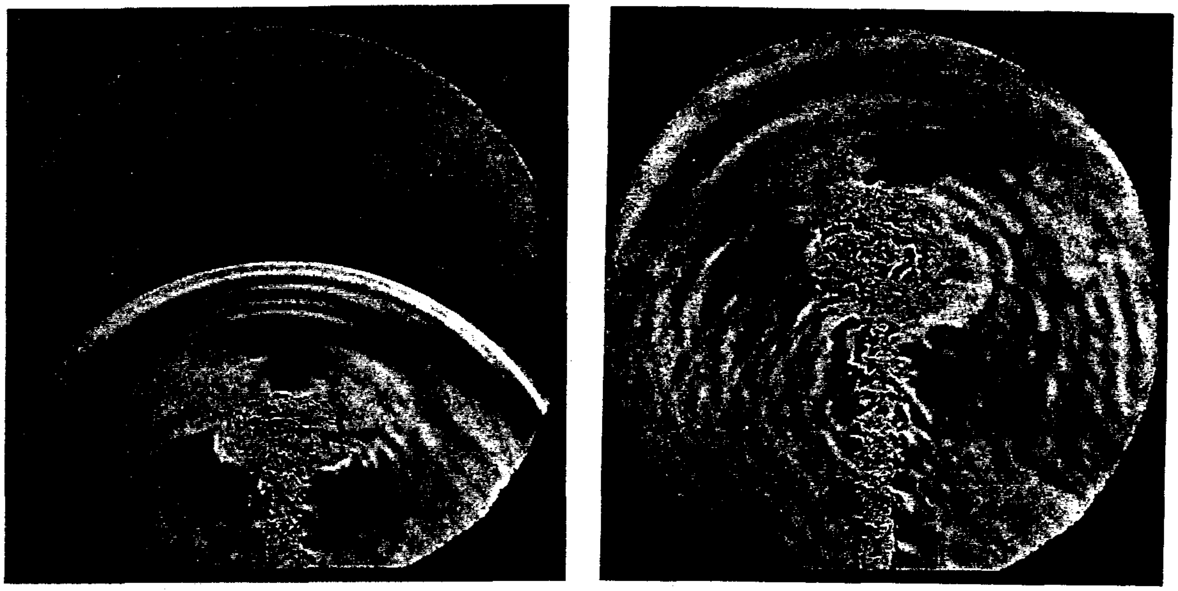

$ta_o/D = 10$ (a) 20

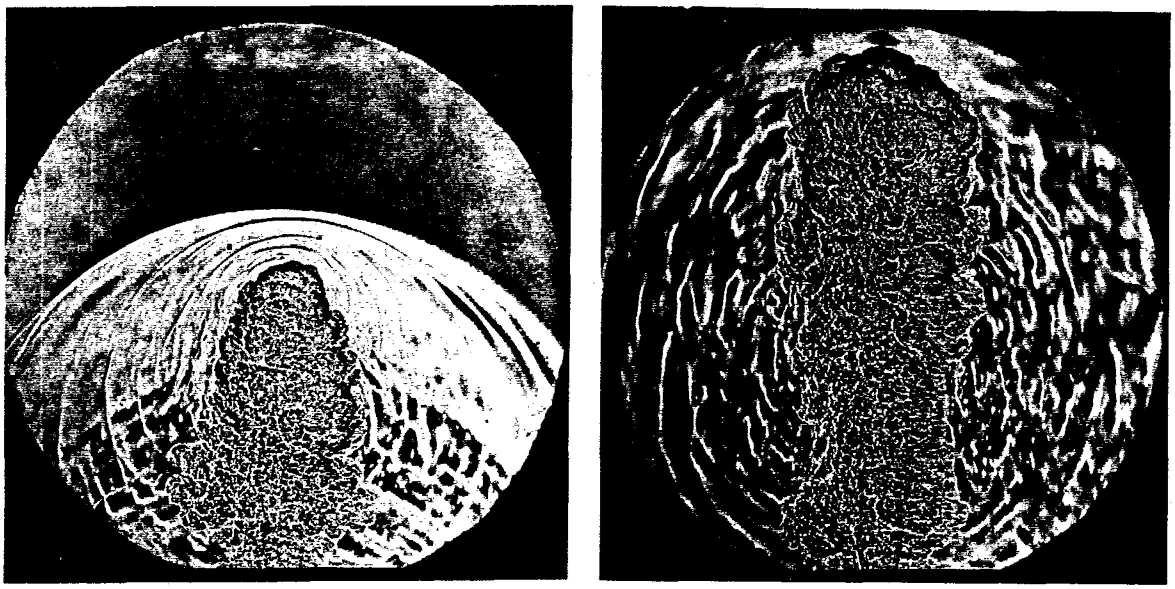

70 (b) 140

Figure 5.5 Development of the jet head in a heavy atmosphere at $P_o/P_a = 3$ (a) $SF_6 \rightarrow SF_6$ and (b) $He \rightarrow SF_6$.

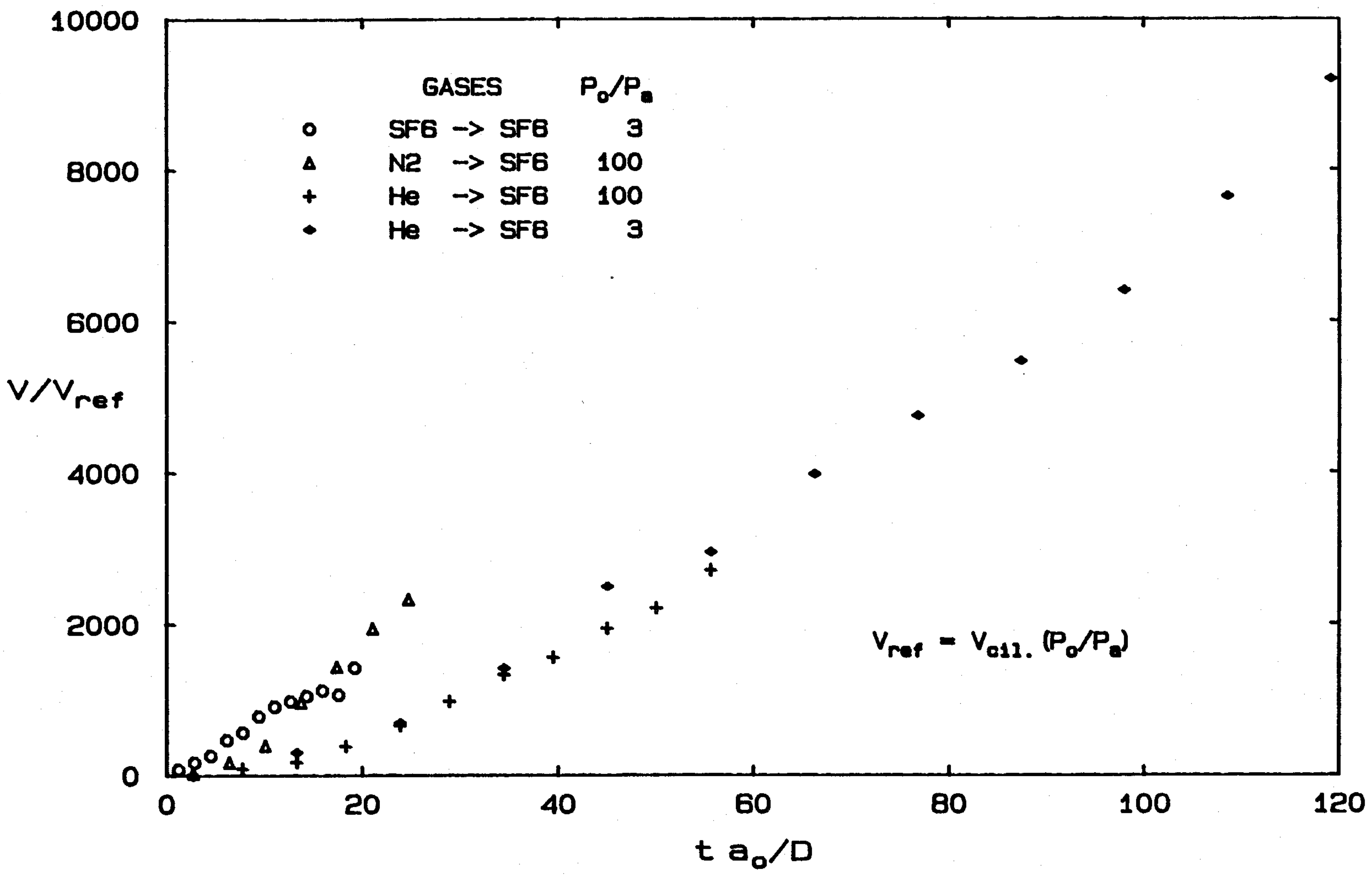

Figure 5.6 The evolution of the jet head volume for several gas combinations.

figure indicates that the volume of lighter jets increases continuously, while the volume of heavier jets tends to an asymptotic value as pointed out before in figure 5.5.

The trajectory of the top of the jet head on the center line, as a function of time, was obtained from the high speed movie. This is shown in figure 5.7, for high pressure ratios and in figure 5.8, for low pressures. A least squares fit of the data is represented by the solid line. Figures 5.7 and 5.8 also show the first derivative of the experimental points and of the fitted curve. Both derivatives are scaled to directly provide the Mach number. The function which was chosen to fit the data is initially linear with time, and at $(X/D)_t$ switches to another law that is proportional to the square root of time. The transition location $(X/D)_t$ is evaluated in the least square sense. This function is chosen to represent both the near field behavior before jet closure and the final asymptotic behavior controlled by the jet entrainment. Justification of the square-root behavior based on considerations of entrainment are presented in Appendix D. The author is indebted to Prof. E.E. Zukoski for pointing out this argument. However the case of figure 5.8 exhibits a linear behavior during the whole period of observation.

Plots similar to figure 5.7 were generated for jets at other pressure ratios and gas combinations. Table 5.1 summarizes the results for the development of the jet head. The absence of results indicates that a prominent change of slope did not occur during the observation time. Table 5.1 indicates that the initial Mach number of the head $(M_i)$ increases with pressure ratio and decreases with molecular weight ratio $(W_o/W_a)$. The location of asymptotic behavior is also a weak function of the ratio of molecular weights. In fact the distance from the jet exit to this location is directly proportional to $(W_o/W_a)$ which was expected because of the entrainment effect.

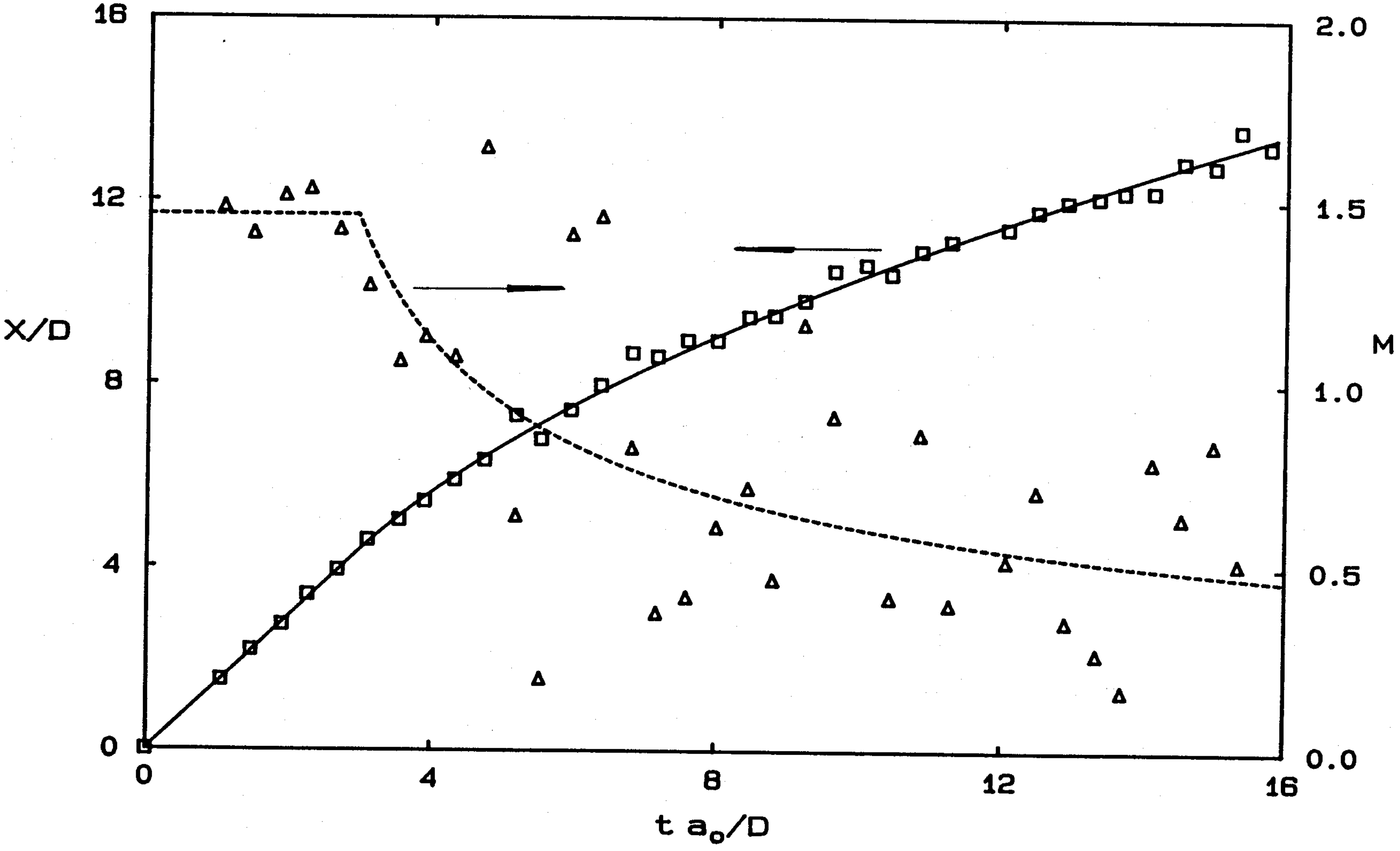

Figure 5.7 The evolution of the jet head for $SF_6$ -> $SF_6$ at $P_o/P_a$ = 100.

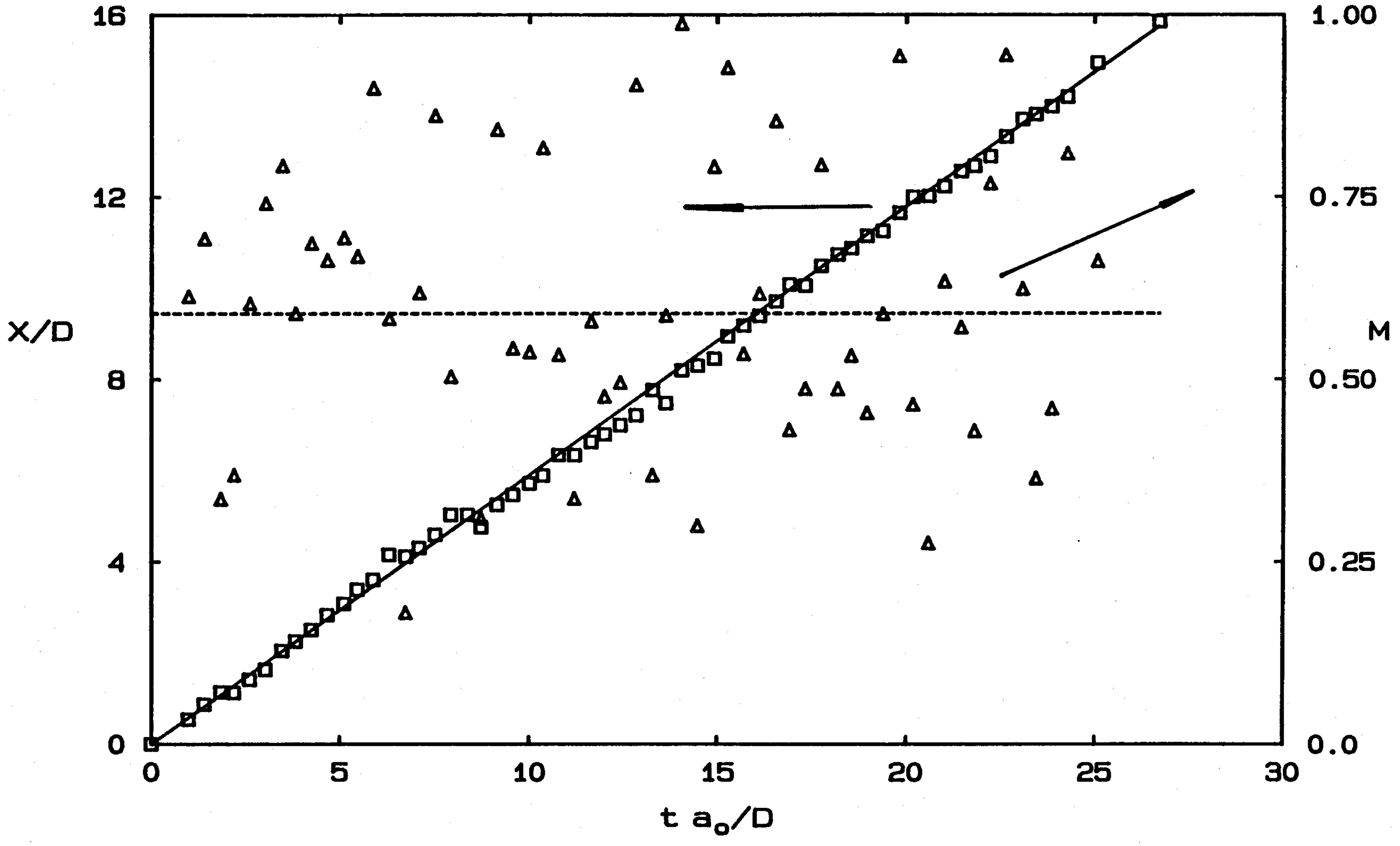

Figure 5.8 The evolution of the jet head for $SF_6$ -> $SF_6$ at $P_o/P_a$ = 3.

The equation 11 from Kieffer & Sturtevant (1984) is an empirical expression for the velocity of the jet head. This expression was compared with the data in Table 5.1. The low pressure ratio cases could be predicted by that expression to within 20%. However the case He → $SF_6$ exhibited the highest discrepancy of 50%. Since that expression was obtained only from low pressure ratio cases, the high pressure ratio cases of the present work are completely off the prediction.

Table 5.1 - The Development of the Jet Head

| gas combination | $M_i$ | | $(X/D)_t$ | |
|---|---|---|---|---|
| | $P_o/P_a = 3$ | $P_o/P_a = 100$ | $P_o/P_a = 3$ | $P_o/P_a = 100$ |
| $SF_6$ → $SF_6$ | 0.6±0.2 | 1.5±0.3 | - | 4.3±0.3 |
| $SF_6$ → $N_2$ | 0.5±0.1 | 0.8±0.2 | 10.3±0.3 | 8.4±0.4 |
| $SF_6$ → He | 0.2±0.1 | 0.3±0.1 | - | - |
| $N_2$ → $SF_6$ | 0.8±0.3 | 2.3±0.3 | 10.8±0.4 | 7.1±0.2 |
| $N_2$ → $N_2$ | 0.6±0.1 | 1.2±0.3 | 10.8±0.4 | 6.4±0.3 |
| $N_2$ → He | 0.4±0.1 | 0.5±0.2 | 11.5±0.5 | - |
| He → $SF_6$ | 0.9±0.3 | 3.5±0.5 | 9.0±0.3 | 3.3±0.2 |
| He → $N_2$ | 0.9±0.2 | 1.8±0.2 | 10.8±0.4 | 4.3±0.3 |

Transition from the initial to the asymptotic behavior for the propagation of the jet head occurs at $(X/D_t)$ of around 8 for high pressure jets and around 11 for low pressure jets. This location is closer to the jet exit for higher pressure jets because entrainment increases with an increase in pressure ratio.

# Chapter 6

# EXPERIMENTAL RESULTS FOR BOW SHOCK

## 6.1. Introduction.

This Chapter reports on the experimental results which show the influence of pressure and density ratio on the shape of the bow shock and the time evolution of the bow shock for extreme values of pressure ratio and different gas combinations. A series of line drawings of the bow shock for different pressure ratios at the same time, as well as of their development for different pressure ratios and gas combinations, are also included.

Of the nine possible cases, only five offered a visible bow shock. The other four cases involve a light atmosphere with small density gradients. The results are organized to show (i) qualitative features of the bow shock, and (ii) quantitative features of the bow shock .

## 6.2. Qualitative Features of the Bow Shock.

In the previous Chapter it was pointed out that light jets have a tendency to form asymmetric jet heads and that these heads induce deformations on the bow shock. Figure 6.1 shows the case of He → $SF_6$ forming a deformed head that distorts the bow shock. These distortions are caused by the wavelets produced by the corners of the head. The wavelets reach the bow shock and locally increase its strength. The region of the bow shock with higher strength tends to move faster than others. This non uniform movement makes the observed distortion on the bow shock.

As with case of the jet head, the distortions on the bow shock tend to be pressure ratio dependent. Maximum deformations are observed deformations on medium pressure ratio cases which are caused by distortions on the jet head. These distortions on the bow shock are shown in the collection of pictures displayed in Chapter 3. The time at which

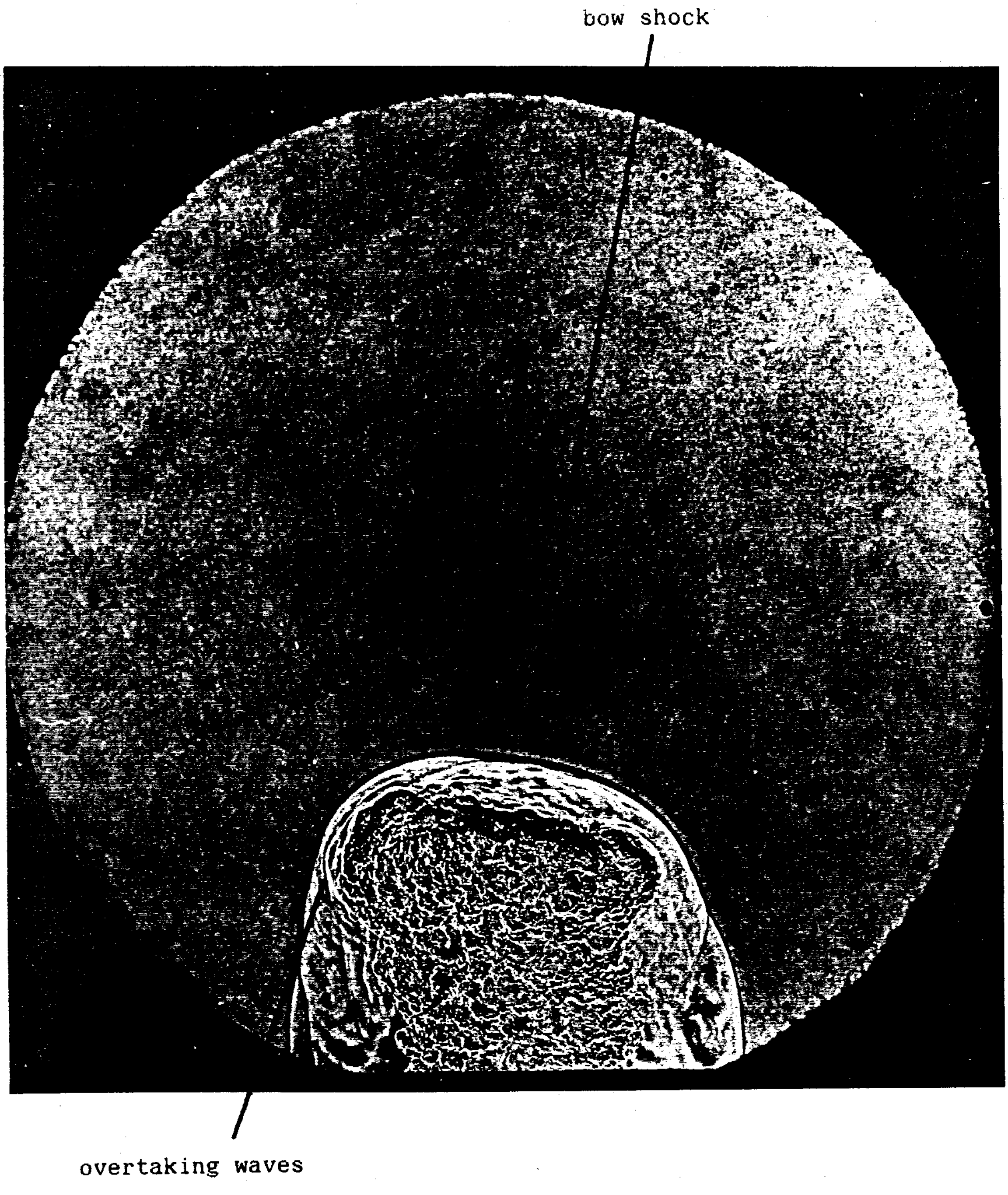

Figure 6.1 Influence of jet head shape on the development of the bow shock for He → $SF_6$ at $P_o/P_a$ = 20 and t = 100 $\mu$s.

these distortions are a maximum depends on the gases in use. In general, at $t \simeq 100\ \mu s$ the recorded pictures exhibited larger distortions when compared with other pictures recorded at different instants of time. The bow shock at about this time, for the different pressure ratio cases involving light into heavy are represented in figure 6.2. The cases involving He → $SF_6$ and $N_2$ → $SF_6$ exhibited higher distortions caused by the non-uniform lateral growth and non uniform propagation of the jet head as explained before for figure 6.1. For the case of He → $N_2$, the distortions are smaller, because the jet head is less distorted due to the lower inertia of the atmosphere.

From the high speed movie, a series of pictures is presented in figure 6.3 showing how the bow shock develops with time for several gas combinations at high pressure ratios. The shock waves are seen to be distorted at early times; this distortion is the largest for the extreme case of a light gas into a heavy gas. These distortions are most predominant in the case of He → $SF_6$, where the distorted cocoon forms the jet head. As time increases, and the shock propagates away from the jet head the distortions tend to smooth out. Additional information such as the decay of perturbations and the evolution of the center of curvature of the bow shock can also be drawn from the pictures.

### 6.3. Quantitative Features of the Bow shock.

The temporal development of the bow shock is highly dependent on the gas combination and the pressure ratio. Of course, the lighter the jet, the stronger and faster the bow shock. On the other hand, in heavier atmospheric gases, due to the low sound speed, the bow shock is slower but stronger. Figure 6.4 and 6.5 shows the trajectory of the bow shock and the shock Mach number for two typical cases of light into heavy combinations, under different pressure ratios. These plots were obtained from an analysis of the high speed movie frames. The curve fits for the bow shock location were obtained with a function with finite slope at the origin and an asymptotic linear behavior. As with the

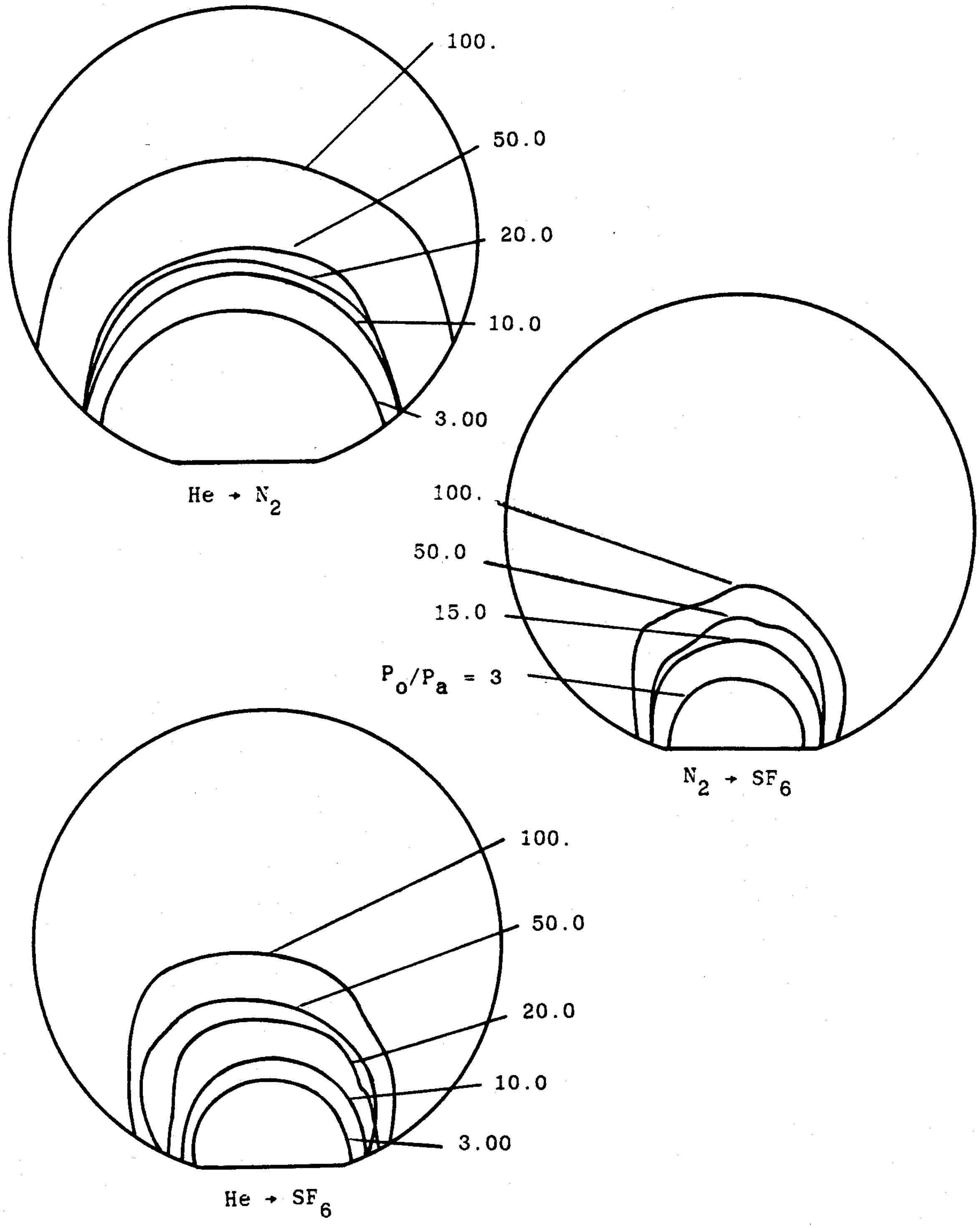

He → $N_2$

$N_2$ → $SF_6$

He → $SF_6$

Figure 6.2 Influence of the pressure ratio on the development of the bow shock at t = 120 μs.

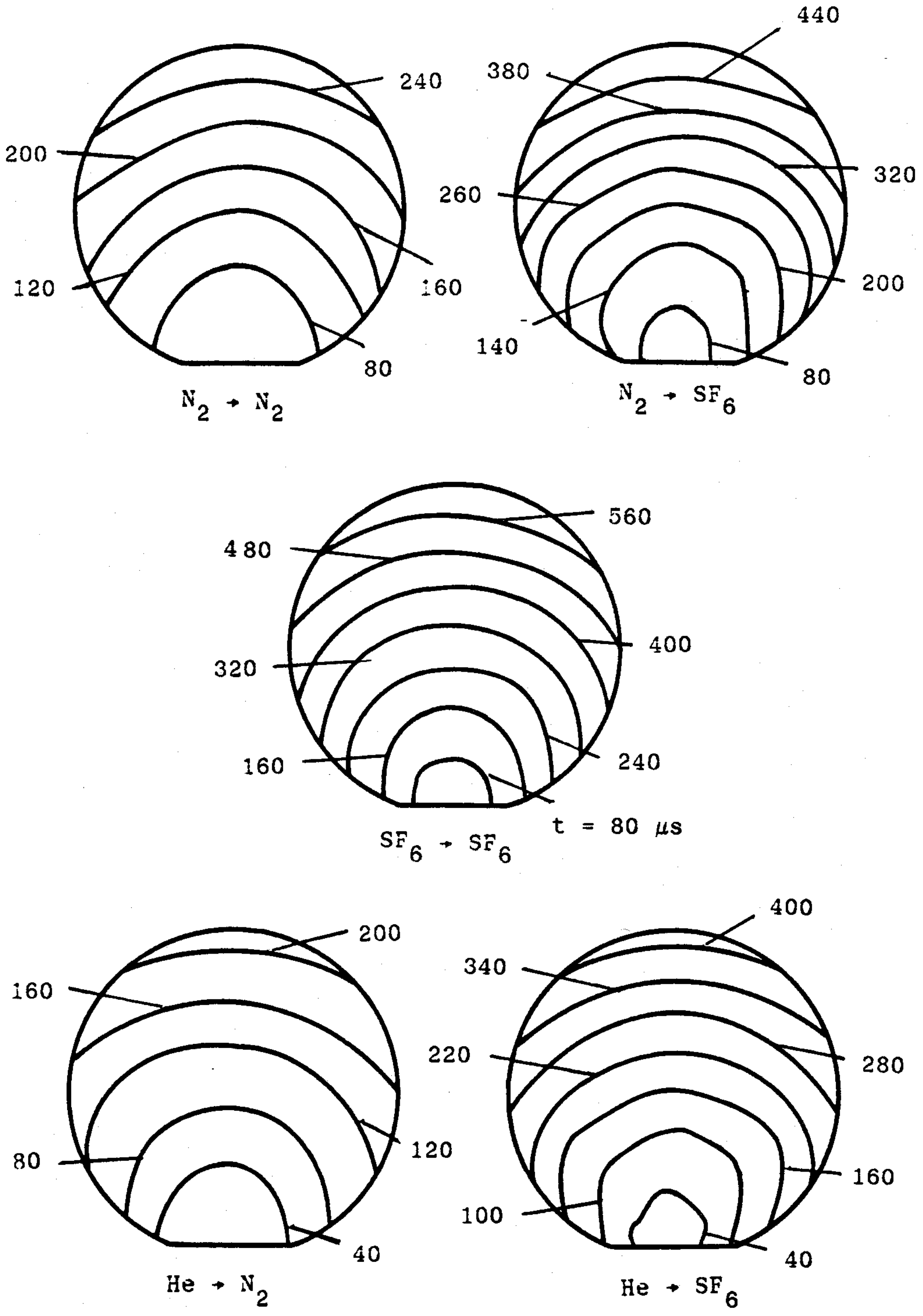
$N_2 \rightarrow N_2$

$N_2 \rightarrow SF_6$

$SF_6 \rightarrow SF_6$

$He \rightarrow N_2$

$He \rightarrow SF_6$

Figure 6.3 Development of the bow shock for $P_o/P_a$ = 100 and several gas combinations.

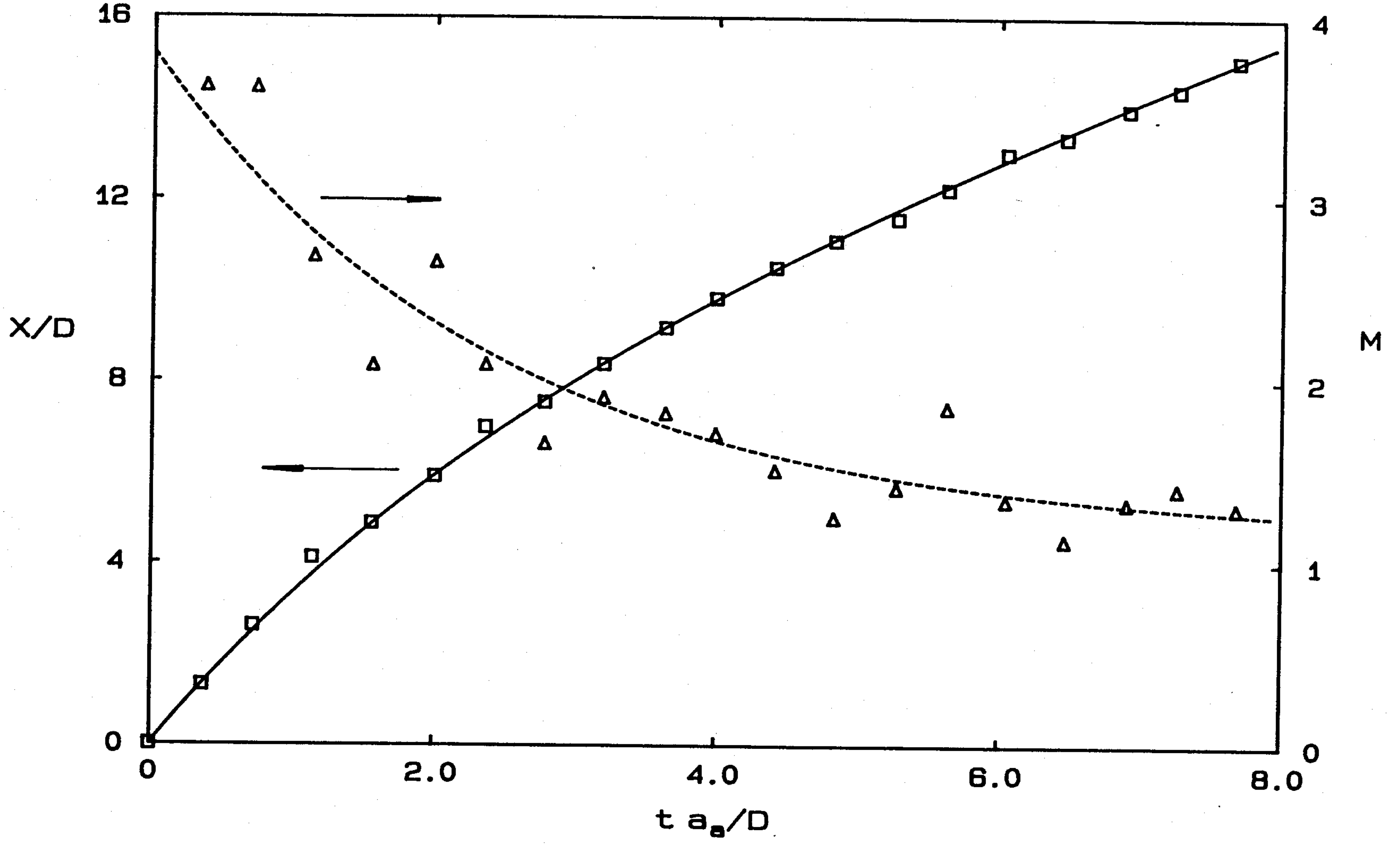

Figure 6.4 The evolution of the bow shock for He -> $SF_6$ at $P_o/P_a$ = 100.

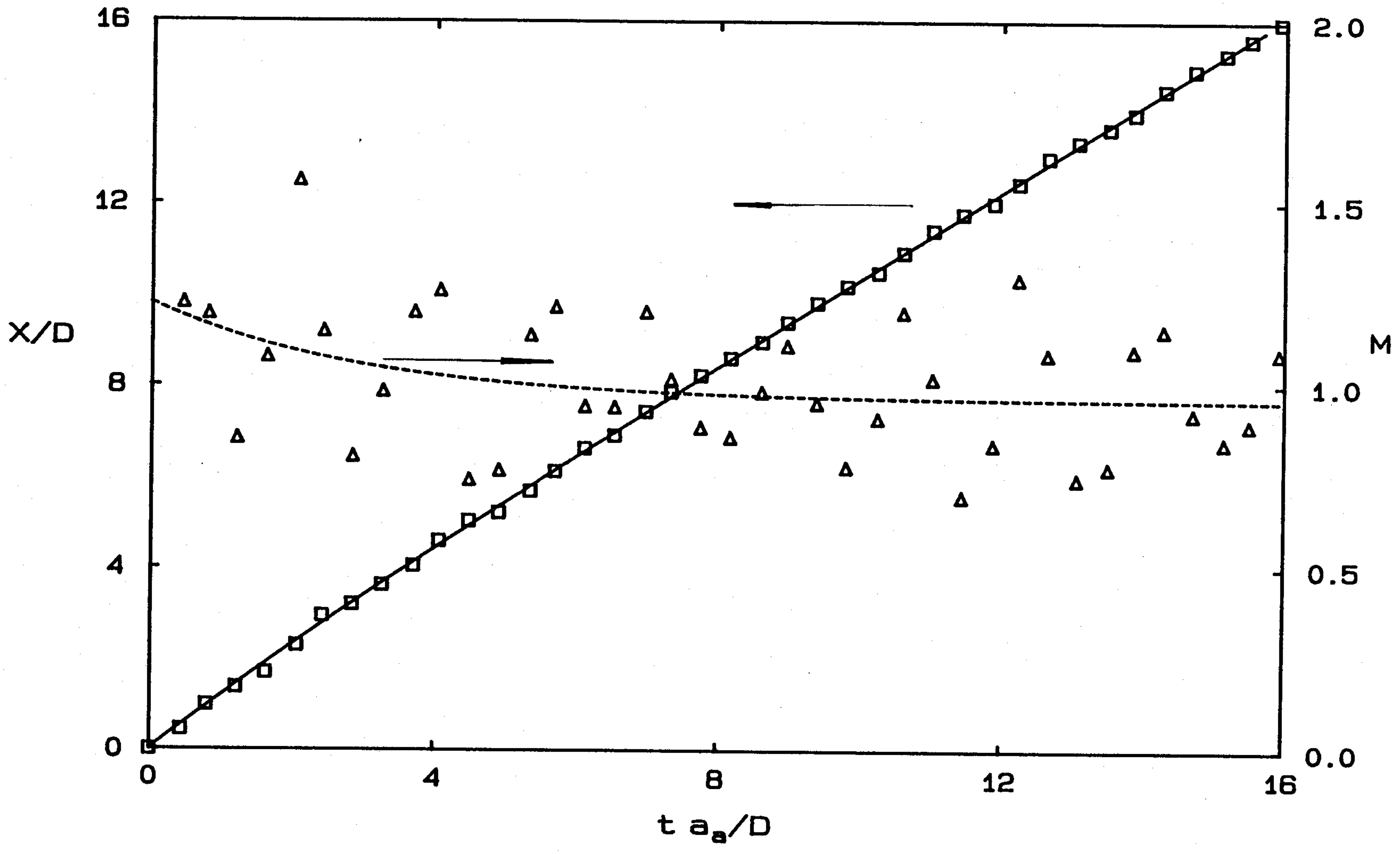

Figure 6.5 The evolution of the bow shock for $N_2$ -> $SF_6$ at $P_o/P_a$ = 3.

jet head in the previous Chapter, both the experimental points and the curve fitting were differentiated and scaled to provide the bow shock Mach number.

Figure 6.4 shows the typical behavior of a light gas into a heavy gas at a high pressure ratio. In this case the shock speed is initially large but is rapidly attenuated caused by the rapid damping of the jet head. This behavior can be altered by changing the jet gas or lowering the pressure ratio, as shown in figure 6.5. Here the initial Mach number is about 1/3 of the previous case and is much closer to the asymptotic value of unity. This causes the attenuation on the evolution to be substantially lower.

The experiments that were carried out which provided plots similar to figures 6.4 and 6.5, also gave the initial Mach number of the bow shock ($M_i$) and the location $(X/D)_t$ for which asymptotic behavior is attained. This location was obtained where the bow shock Mach number is about 20% larger than the asymptotic value of unity. This information is arranged in table 6.1 for the two extreme pressure ratios and the different gases combinations for which the bow shock was visible.

For fixed pressure ratio the initial Mach number ($M_i$) increases with the molecular weight of the atmospheric gas because of the lower sound speed. That Mach number also decreases with the molecular weight of the jet gas since the escaping speed of the jet gas depends on its sound speed that is smaller for heavier gases. High pressure ratios also exhibit higher $M_i$ because the initial volume of gas that is injected into the atmosphere is proportional to the mass flow rate, which is also proportional to the pressure ratio. For lower pressure ratios, the effect of gas combination is smaller, and consequently the initial Mach number varies only slightly from case to case.

Table 6.1 - The Development of the Bow Shock

| gas combination | $M_i$ |  | $(X/D)_t$ |
|---|---|---|---|
|  | $P_o/P_a$ = 3 | $P_o/P_a$ = 100 | $P_o/P_a$ = 100 |
| $SF_6 \rightarrow SF_6$ | 1.4±0.1 | 1.8±0.2 | 7.1±0.4 |
| $SF_6 \rightarrow N_2$ | 1.2±0.1 | 1.3±0.1 | 6.9±0.3 |
| $N_2 \rightarrow SF_6$ | 1.2±0.2 | 2.7±0.3 | 7.7±0.4 |
| $N_2 \rightarrow N_2$ | 1.3±0.2 | 1.7±0.1 | 7.3±0.4 |
| $He \rightarrow SF_6$ | 1.3±0.2 | 3.8±0.2 | 7.2±0.5 |
| $He \rightarrow N_2$ | 1.4±0.2 | 2.3±0.2 | 7.3±0.5 |

The position at which the bow shock reaches the asymptotic behavior for high pressure ratio cases, was found to be around seven exit diameters downstream of the jet exit. For lower pressure ratios, a prominent change in slope wasn't observed.

# Chapter 7
# DISCUSSION

## 7.1. Introduction.

Experiments were performed to study the initial phase of impulsively started gas jets to understand the time, gas combination and pressure ratio dependency of selected features. In particular, the effects of these parameters on the development of the Mach disk, the jet head and the bow shock have been examined. The variation of the shape of the jet with the gas combination was also explored. The purpose of this chapter is to provide additional information together with a comparison with the results of other work where possible.

## 7.2. The Propagation of the Mach Disk.

During the initial instants of flow, as the exit pressure increases, the Mach disk forms within a few diameters downstream of the jet exit. With further increase in exit pressure, the Mach disk propagates further downstream until the exit pressure reaches its maximum. The time required for the Mach disk to reach the maximum position depends on the pressure ratio between the reservoir and the atmosphere, as well as the molecular weight of the gases. Figure 7.1 shows the initial development of the Mach disk in which normalization of time and position shows the collapse of the curves for the initial phase. This collapse was obtained through the use of the molecular weight ratio because the time to reach 75% of the maximum location of the Mach disk is inversely proportional to the ratio, as can be verified in figure 4.4. This proportionality maybe caused by the slower breaking of the diaphragm due to the atmospheric drag.

A power law was fitted to the initial phase in figure 7.1 and the time dependence was found to grow as 0.661, while the muzzle blast of Schmidt & Shear (1974) was shown to grow to the power of 0.652 for the first 100$\mu$s of the propellant flow. In the present experiments

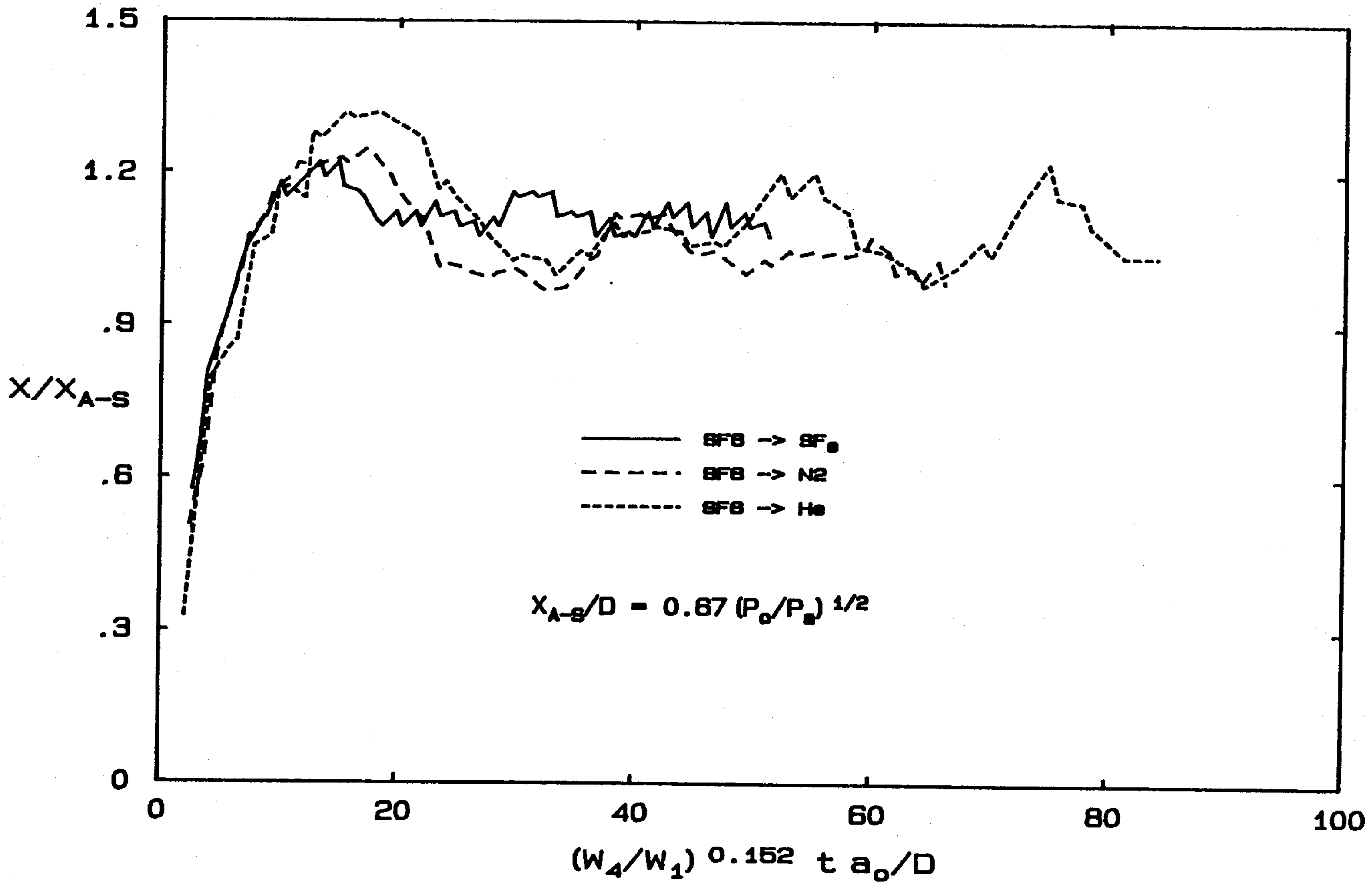

Figure 7.1 The initial propagation of the Mach disk at $P_o/P_a = 100$.

insufficient data was obtain in this interval of time. This agreement may be fortuitous, since (a) the time interval during which Schmidt & Shear obtained their data was much smaller than in the present measurements, so the attenuation would be expected to be smaller, (b) the pressure ratio of the propellant flow attained a value six times larger than in the present experiment and (c) the propellant gas had a molecular weight of 25.6 and a ratio of specific heats of 1.24. Nevertheless, the time to maximum position observed by Schmidt & Shear was around 350$\mu$s, which lies between our observed times of 500 $\mu$s for $SF_6$ ($\gamma$ = 1.093) and 280 $\mu$s for $N_2$ ($\gamma$ = 1.4).

## 7.3. The Jet Head.

The jet head assumes a shape that depends on both gases and on the pressure ratio. In the case of heavy gas into light atmosphere most of the gas is contained in the jet body, as shown in figure 5.5 (a). However in the case of a light fluid into a heavy atmosphere, shown in figure 5.5 (b), most of the jet gas is contained in the recirculating flow. Figure 7.2 shows the cases of light into heavy obtained both in the present work and by Lin (1986). The difference between these two cases is the atmospheric fluid. The present experiment uses $SF_6$ whereas Lin uses water that is 153 times as dense. The case involving $SF_6$ as atmosphere exhibits the jet boundary inside the recirculating flow. A sketch of the streamlines for this case is shown in Appendix A.

In figure 7.3 two light into heavy cases are shown with the same atmospheric gas ($SF_6$). Although both cases are shown within the same order of flow time and both have the same head volume, their shape are different. For He the jet is entirely enclosed by a "cocoon" of recirculating fluid, while for $N_2$ the head resembles a vortex ring. Owing to the reduced density the momentum flux for the He jet is lower than for the $N_2$ jet. Heavier jets, as shown here with the $N_2$ jet or with the $SF_6$ jet shown in figure 5.1, exhibit better defined vortex rings. The cases of $SF_6$ → He (figure 3.7) and He → $SF_6$ (figure 3.3) can also be compared at different volumes but at the same time and pressure

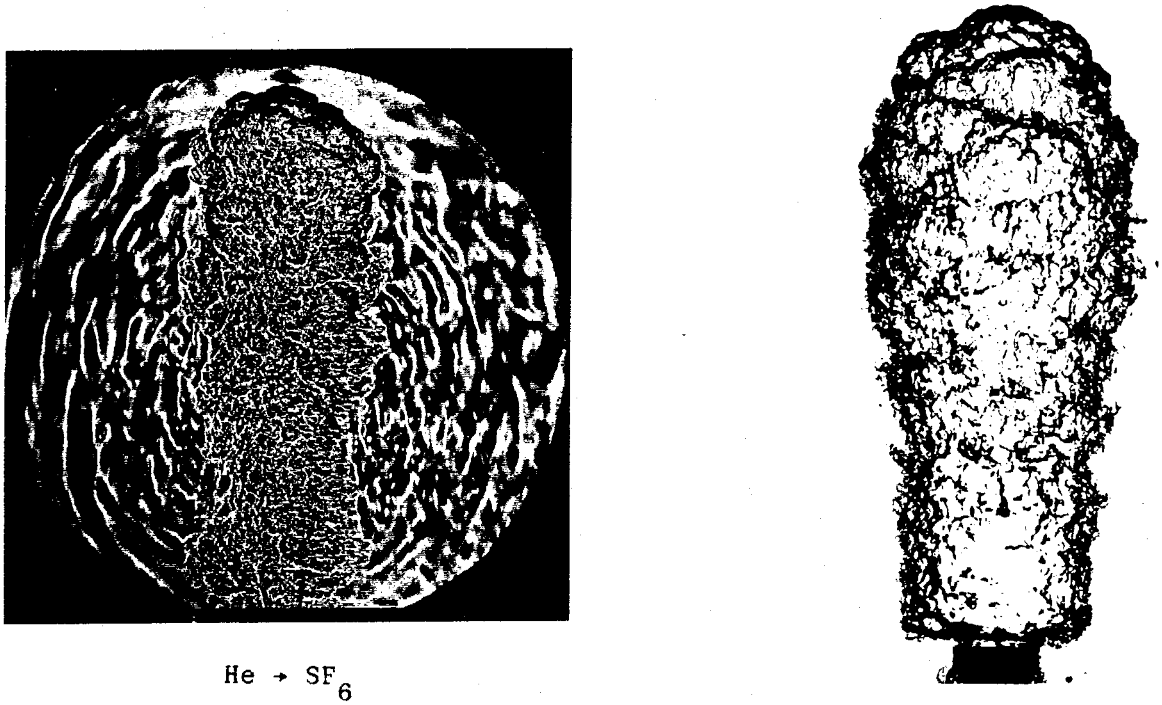

He → $SF_6$

(a)

He → $H_2O$

(b)

Figure 7.2 Comparison between the light jet into heavy atmosphere at equal pressure ratio ($P_o/P_a = 3$) (a) present work and (b) Lin (1986).

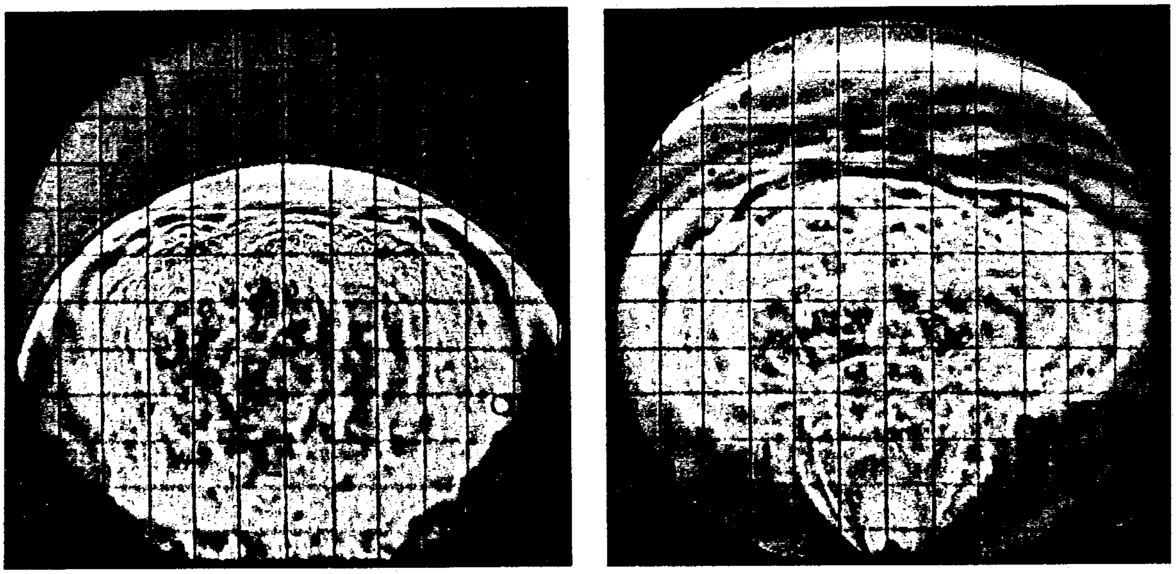

He → $SF_6$

$ta_o/D = 40$

$N_2$ → $SF_6$

20

Figure 7.3 Comparison between cases with same head volume at $P_o/P_a = 100$.

ratio. The heavy into light case develops as a ballistic jet that exhibit larger initial lateral growth as pressure increases, while the light into heavy case forms a head that extends to the jet exit and gets larger as the pressure ratio increases.

The propagation of the jet head during the initial phase is highly dependent on the conditions of the jet. Thus, higher initial Mach numbers can be obtained by higher .pressure ratios using lighter jets. At low pressure ratios the jet head propagates at a constant velocity for longer distances than the high pressure jets. This is because there exists a low exchange of momentum due to entrainment which is directly proportional to the pressure ratio. At higher reservoir pressures the jet head moves at a constant velocity for the first 5 diameters only. However entrainment-induced attenuation occurs later. Figure 7.4 show cases involving $N_2$ and $SF_6$ as atmosphere. These cases exhibit non-linear behavior during late times.

The plot shown in figure 7.4 is an attempt to fit a power law through the data points. The growth-law index $\lambda$ for the jet head after it had propagated about 5 diameters, is close to 1/2. Table 7.1 summarizes several cases.

Table 7.1 - Growth-Law Index for the Jet Head Development

| Gas Combination | $\lambda$ |
|---|---|
| $SF_6 \rightarrow SF_6$ | 0.53 ± 0.04 |
| $N_2 \rightarrow SF_6$ | 0.53 ± 0.07 |
| $He \rightarrow SF_6$ | 0.54 ± 0.07 |
| $N_2 \rightarrow N_2$ | 0.55 ± 0.04 |
| $He \rightarrow N_2$ | 0.53 ± 0.04 |

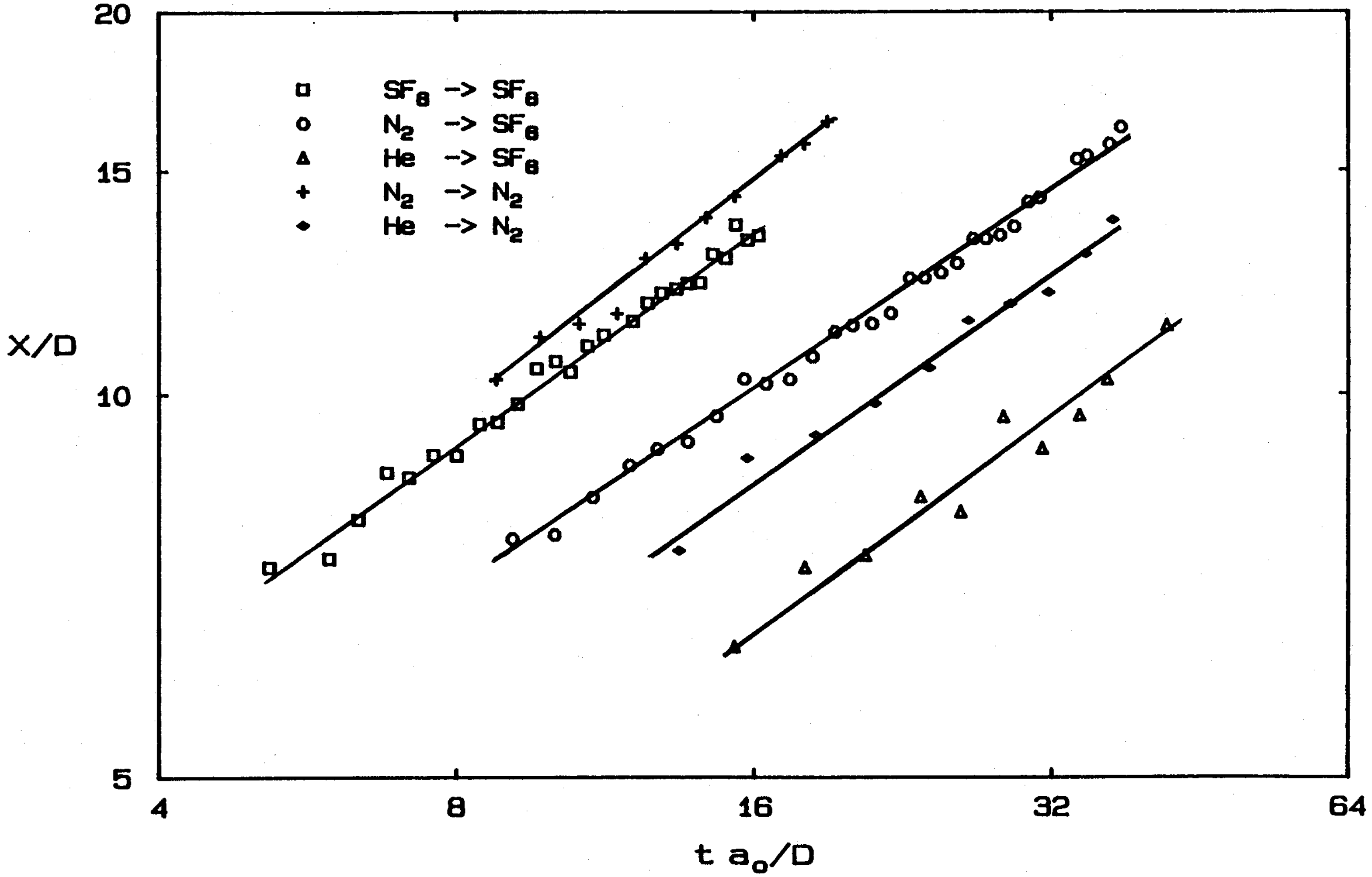

Figure 7.4 – The propagation of the jet head at $P_o/P_a$ = 100.

Based on entrainment considerations, the dependence of the propagation of the jet head on the square root of time is discussed in Appendix D. This observation suggests that the attenuation of the propagation of the jet head is caused by entrainment of the outer fluid, consequently decreasing the speed of the head. The dependence on $\gamma_o$ and density ratio in the result of Appendix D, did not lead to the collapse of the curves in a plot similar to figure 7.4.

## 7.4. The Bow Shock.

Ahead of the jet head, a bow shock is formed. When the jet head velocity is subsonic relative to the atmospheric gas the bow shock propagates faster than the head, getting weaker as it moves ahead. In the cases when the head is initially supersonic the bow shock is strong and closely wrapped around the head, and it moves at the same velocity as the head. Later, the distance between them increases. Figure 7.5 shows the bow shock development at later times for the same cases which were shown in figure 7.4 for the jet head. The plot was an attempt to see if the bow shock evolution could be described by a power law. In fact, the obtained growth-law indexes $\beta$ lie between about 0.7 and 0.9. Table 7.2 summarizes several cases.

Table 7.2 - Growth-Law Index for the Bow Shock Development

| Gas Combination | $\beta$ |
|---|---|
| $SF_6 \rightarrow SF_6$ | 0.88 ± 3% |
| $N_2 \rightarrow SF_6$ | 0.79 ± 2% |
| $He \rightarrow SF_6$ | 0.71 ± 1% |
| $He \rightarrow N_2$ | 0.87 ± 1% |

The growth-law index should be more than 0.5 because the bow shock propagates ahead of the jet head, consequently the bow shock must be less

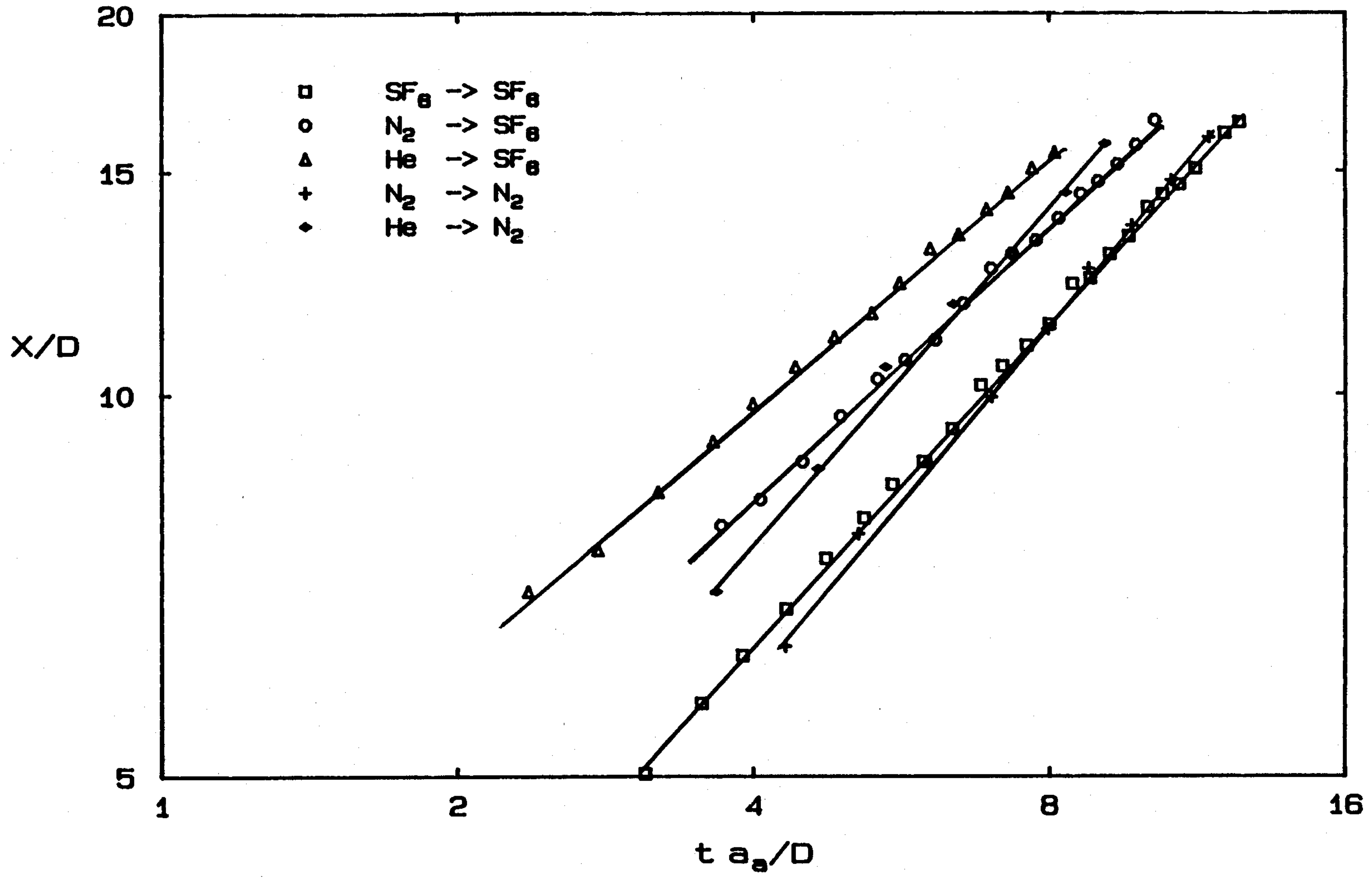

Figure 7.5 - The propagation of the bow shock at $P_o/P_a$ = 100.

attenuated than the head. As the bow shock propagates and gets weaker, it tends to move with a Mach number of unity. Large growth-law indices are caused by less damped bow shocks, typical of higher momentum driven jets. These are represented by the heavier jets in figure 7.5.

Figure 7.6 shows the development of the Mach number of the bow shock with time. The curves where obtained, as in figure 6.4, using the data obtained from the high speed movies. The heavy atmosphere cases are shown because they provide high initial Mach numbers. Also, the curves show that after about eight flow times, the bow shock Mach number is close to unity, independent of its initial value. The lighter jets have higher Mach numbers, because they escape with a higher speed.

A normalized X - t diagram for the flow outside the reservoir is shown in figure 7.7. The trajectories of the Mach disk, jet head and bow shock are indicated. For later flow times a slight decay in the Mach disk location can be observed. This is caused by the decreasing reservoir pressure. At later observation times, the Mach disk can be seen moving upstream towards the jet exit. As the flow decays and becomes subsonic, the Mach disk disappears. The families of curves shown here represent the oscillation of local pressure in terms of the percentage of maximum exit pressure. The percentage values were obtained from the pressure trace of the jet exit in figure A.2. The purpose of this plot is to identify the regions on the X - t plane in which the unsteady flow becomes steady, due to the decay of the oscillations in local pressure. At the region upstream of the Mach disk, the curves are represented by a family of characteristics; however in the subsonic region, the curves are represented by trajectories similar to the jet head trajectory, distanciating themselves from the jet head as time increases and as percentage decreases. Analysis of this plot suggests that the 2% curve can be considered to be the boundary between unsteady and steady flow. At this instant in time at the jet exit, the oscillations in pressure are small enough to be neglected.

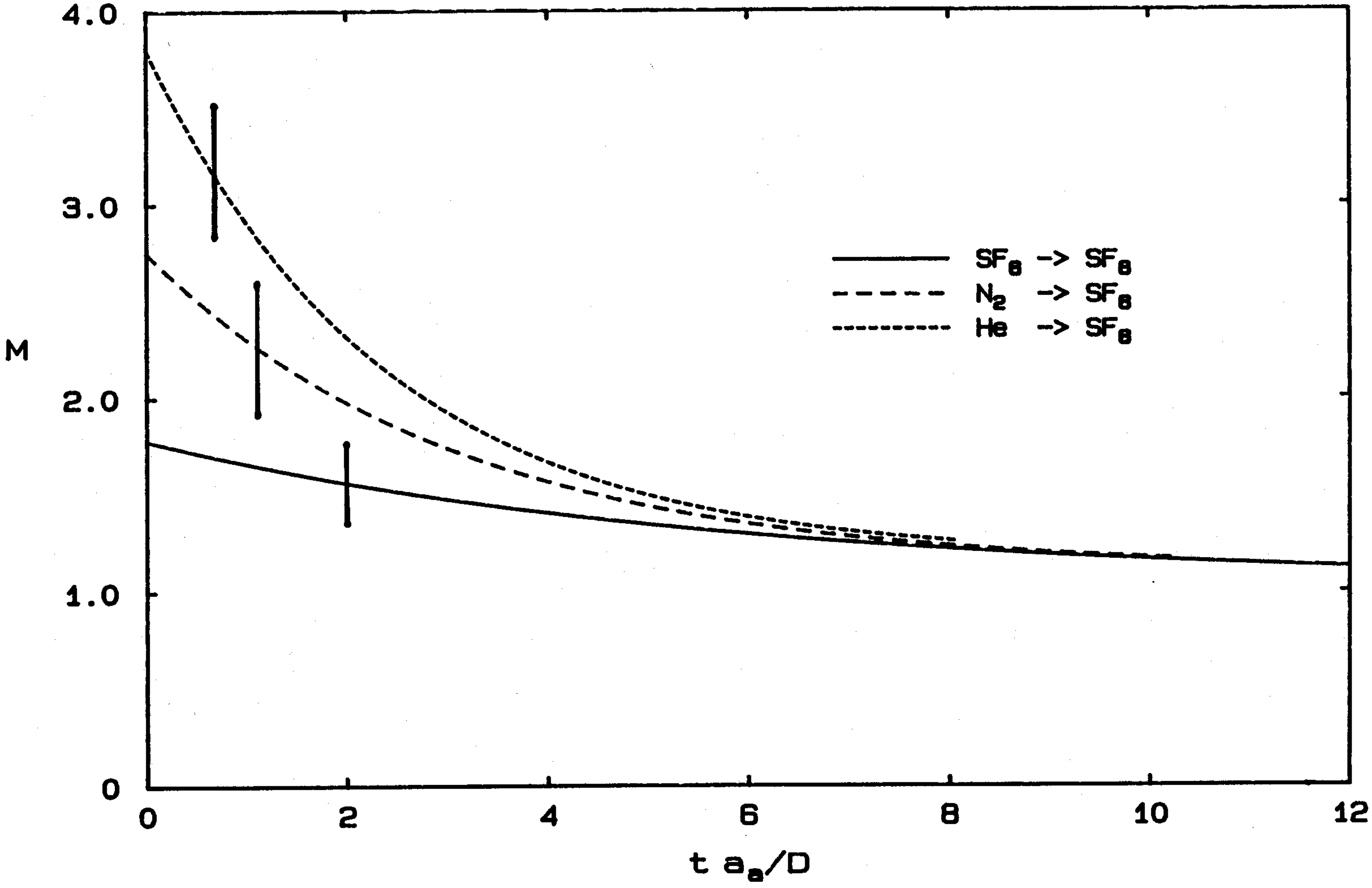

Figure 7.6 The bow shock Mach number at $P_o/P_a = 100$.

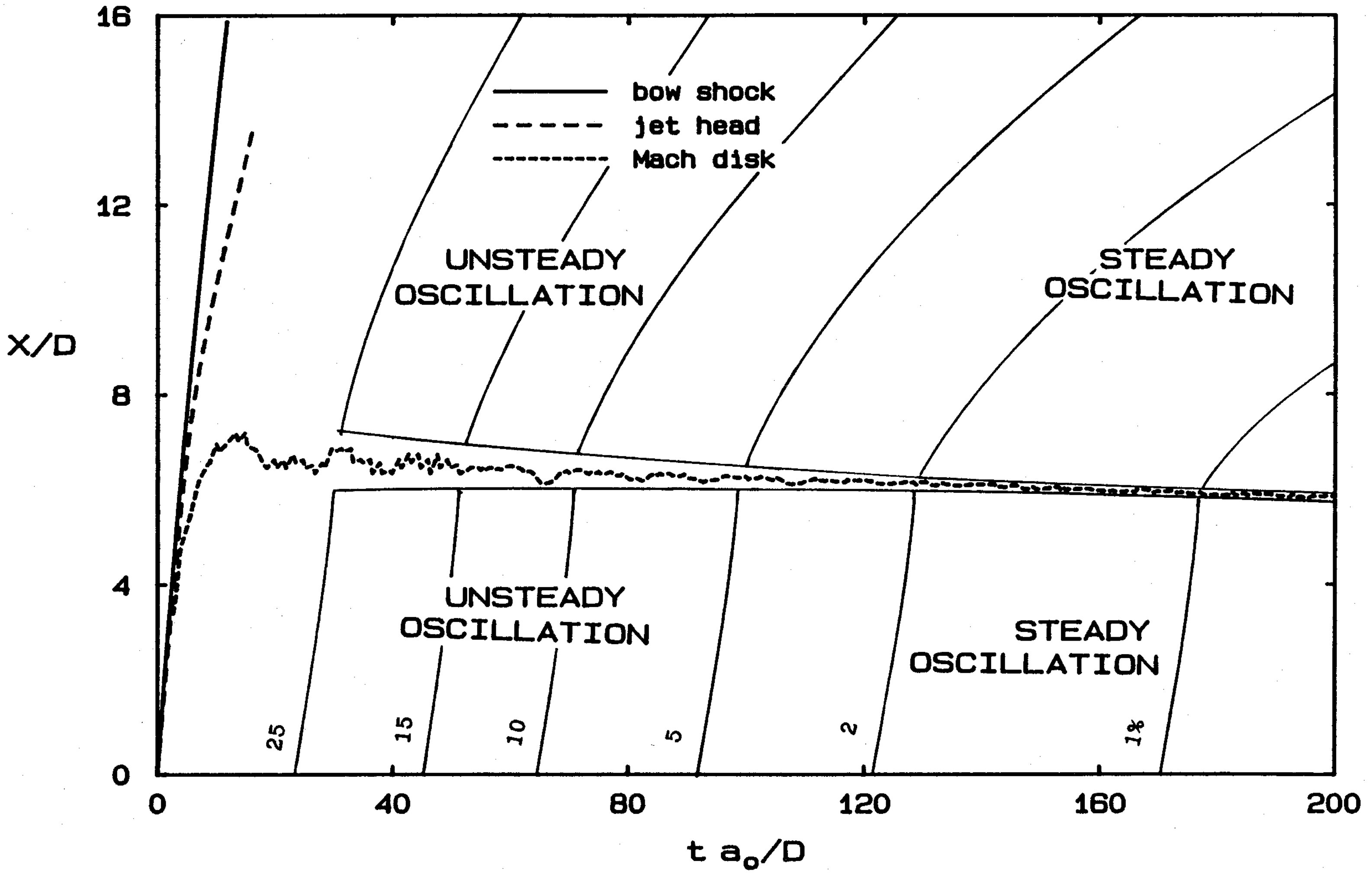

Figure 7.7 Regions showing steady and unsteady flow for $SF_6$ -> $SF_6$ at $P_o/P_a$ = 100.

## Chapter 8

## CONCLUSION

The time evolution of underexpanded supersonic jets has been studied experimentally. This investigation was motivated by the desire to obtain a more detailed physical understanding of the effects of the jet and the atmospheric composition, and the pressure ratio on the starting phase of an underexpanded supersonic jet. The gas, initially confined in a high pressure reservoir, expanded through a contraction section, and escaped from a small exit hole into a controlled atmosphere. Both the jet and the atmosphere were selected from He, $N_2$ and $SF_6$, at preset pressures. To demonstrate the unsteady effects of the jets, high-speed photography and fast-response pressure instrumentation have been used.

It was found that the shape of the jet is dependent on the pressure ratio and on the gases making up the jet and the atmosphere. At low pressure ratios the jets form a repetitive diamond cell structure that is visible better when both the jet and atmospheric gases are the same. In the quasi-steady regime light jets at low pressure ratios exhibited helical instability approximately six jet diameters downstream of the jet exit. This seems an instability which is characteristic of axisymmetric jets. Light jets into heavy atmospheres, when visible, assumed the expected growth rate of $25^{\circ}$ for steady jets in the quasi-steady phase. However, at the start the jet has a bubble shape caused by the damping effect of the high inertia atmosphere. The size of the bubble increases with time and pressure ratio.

During the start up of the jet, a Mach disk forms downstream of the exit; as the flow develops, the Mach disk moves further downstream and oscillates around the quasi-steady position with a characteristic frequency that changes with the conditions of the experiment. These oscillations are caused by pulsations of the throat pressure. It was found that the frequency of the pulsations was close to the resonance frequencies of the reservoir and was caused by the bouncing back-and-forth of the expansion and compression waves inside the reservoir. The position of the Mach disk was verified to be a function of the pressure ratio; the amplitude of oscillation was found to increase with jet fluid density. The steady jet theory of Ashkenas & Sherman (1966) predicts the Mach disk location for steady jets. It was shown to be also useful for predicting the corresponding location of the Mach disk for the quasi-steady jets, provided that the instantaneous exit pressure and the time for the waves to travel from the jet exit to the Mach disk location are taken into account.

The jet head is formed by the accumulation of gas at the front part of the jet. The evolution of the jet head was found to be linear with time initially, but for high pressure ratios, after the jet head has propagated a distance of five exit diameters, it was dependent on the square root of time. This change in behavior is caused by entrainment that develops as the jet head propagates. Lighter atmospheres or lower pressure ratios have lower entrainment rates, consequently these jet heads propagate for larger distances before a change in behavior is noticed. It was also observed that the asymptotic behavior for the evolution of the jet head was reached at a distance of ten exit diameters. In the case of light jets into heavier atmospheres, unsteadiness of the jet head forms waves which overtake the bow shock and distort it. The low pressure ratios of heavy into heavy cases tend to form spherical heads, probably because of the atmospheric damping effect which forms a cocoon at early times. Due to the high momentum flux of the jet at later times, since the exit pressure is increasing, a ballistic jet forms behind the cocoon and pushes it into the atmosphere. The amount of gas that is pumped into the jet head is a function of the jet gas. Lighter jets have a tendency to form larger head volume which is caused by the atmospheric damping effect that persists for long times. The vortical nature of the jet head is most visible at medium pressure ratios of medium to dense jets into dense atmospheres, however higher pressure ratio seems to produce more violent mixing resulting in the vortex ring becoming more diffuse. In some cases of light into heavy, the presence of a double-head, whose appearance seems to be related to the presence of a nonsteady normal shock just upstream of the head, was observed.

The bow shock evolution was found to exhibit a non-linear behavior. The growth-law indexes which were obtained are far from that observed for spherical ($\beta$ = 0.4) and axisymmetric ($\beta$ = 0.5) explosions. However, growth-law indexes were found in the expected range between 1/2 and 1, i.e. between that of the jet head and of an acoustic wave. The initial bow shock Mach number increases with pressure ratio and with the molecular weight of the atmospheric gas and decreases with the moleculat weight of the jet gas. The asymptotic behavior is reached a distance of eight exit diameters for high pressure ratios. Which means that after this location the propagation is independent of the jet gas.

The results which were obtained from the present work lead to some suggestions for future work. High speed movies can provide information on the upstream propagation of the Mach disk during the decay phase of the jet. High spatial resolution pictures, can give information on the decay of perturbations on the bow shock and also evolution of its center of curvature. Changes in the geometry of the jet exit can be performed to understand pressure matched jets, by replacing the convergent nozzle by a Laval nozzle. Replacing the reservoir by a slender reservoir with constant area section can provide results for comparison with a muzzle blast. Also, the study of the influence of the wave field inside the reservoir on the outer flow features can be investigated.

# Appendix A

# OBSERVATIONS AND MEASUREMENTS OF THE FLOW FIELD

## A.1. The Formation of Waves at the Jet Exit.

An underexpanded jet is characterized by the flow of gas from a pressurized reservoir in which the static exit pressure is higher than the ambient pressure. For this type of jet, its cross-section area increases as the jet expands to the ambient pressure and is shown in figure A.1. The exiting flow is supersonic and further downstream it gets subsonic, requiring the formation of a strong shock wave inside the jet to change the flow regime. This shock wave is slightly curved and is located several diameters downstream of the jet exit; it is called a Mach disk.

As the jet expands at the jet exit, a Prandtl-Meyer expansion fan is formed reaching the free jet boundary and reflecting as a series of compression waves. These compression waves coalesce, forming an oblique shock in the jet interior. This shock is weak and causes the deflection of the flow direction, leaving a supersonic flow behind it. The shock intercepts the Mach disk, forming a reflected shock that is also weak, and consequently the flow behind it is still supersonic. The flow downstream of the Mach disk and downstream of that weak shock must be bounded by a viscous shear layer, since they are flowing at different speeds. When the reflected shocks intercepts the jet boundary, it reflects as an expansion fan that propagates and reaches the jet boundary again. for lower pressure ratios these reflection repeat several times exhibiting the known diamond cell structures, that were observed in Chapter 3. All these features were pointed out in the work of Crist et al. (1968), where they studied highly underexpanded steady jets. It should be noted that the same observation is valid for unsteady jets, however the difference is that the shocks and the expansions oscillate

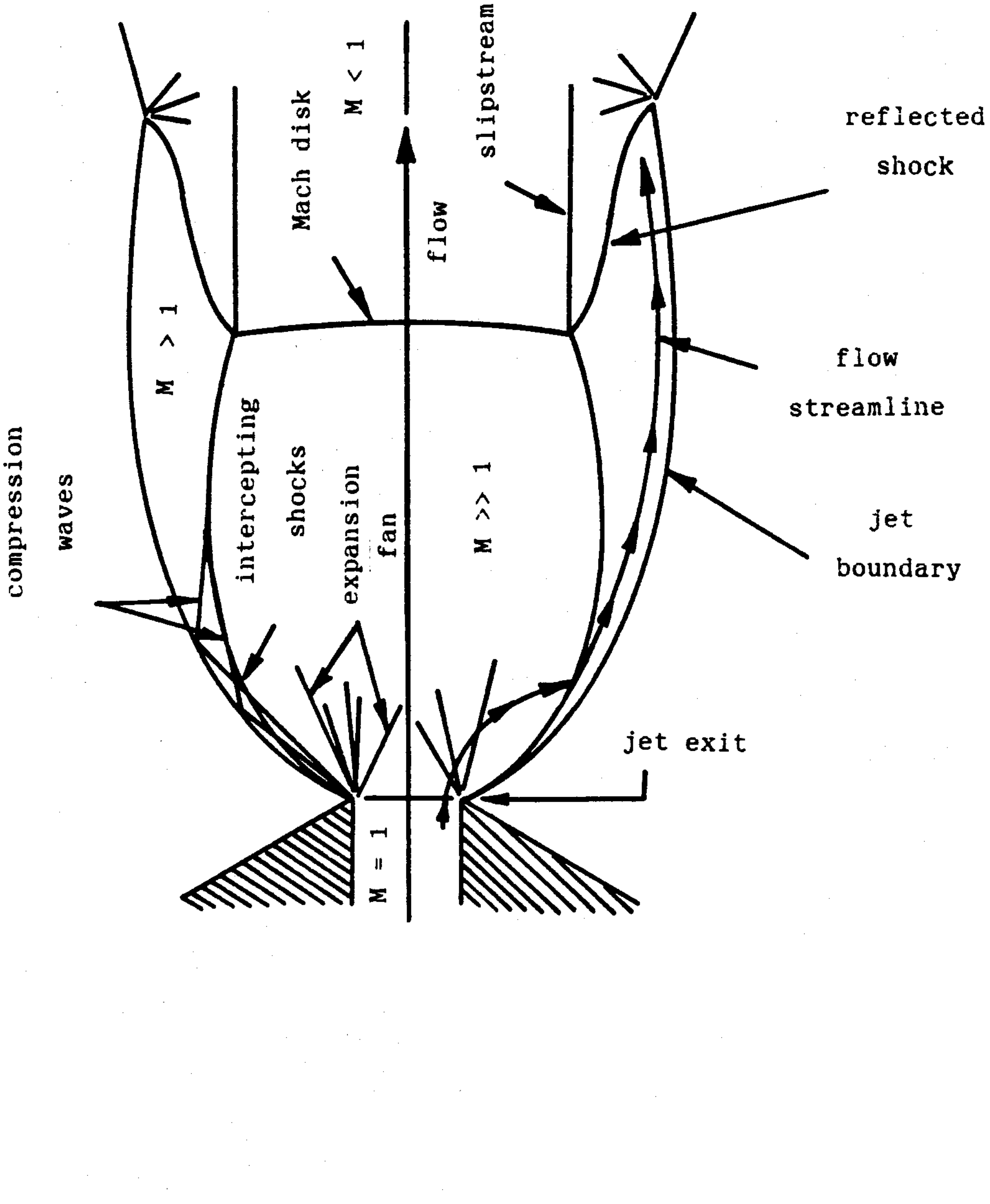

Figure A.1 Flow structure at the exit of an underexpanded jet.

in position due to oscillations in the jet exit pressure.

### A.2. Pathlines for Low Pressure Cases.

The pathlines showing recirculating regions in the low pressure ratio cases of heavy into light and light into heavy are shown in figure A.2. When the light jet penetrates the heavy fluid, it rebounds and forms an outer layer that entrains the jet, up to the jet exit. However, in reverse case all the entrainment is made closer to the top of the head forming a vortex ring. The reason for this is probably as a result of a light gas reflecting more when moving against a heavy atmosphere, whereas a heavy gas penetrates more as it moves into the light atmosphere.

### A.3. The Pressure History of the Flow Field.

The experimental facility enabled to record the pressure history at the top of the tank, at the jet exit and at the bottom of the reservoir as shown in Chapter 2. Those pressure traces are shown in figure A.3 for an experiment of $SF_6 \rightarrow SF_6$ at $P_o/P_a = 100$. A brief explanation on each pressure trace is provided below.

A.3.1. <u>Top of the Tank</u>. The initial pressure in the tank is set to 10 kPa. After the diaphragm breaks (at t = 0.0 ms), the pressure at the top of the tank remains unchanged until the bow shock reaches the transducer at the tank end plate; it provides a rise in pressure of 1.0 kPa at 2.7 ms as shown in figure A.3. This shock waves reflects on the tank end plate and propagates toward the jet exit. However the incident bow shock that was reflected by the tank walls focuses on that transducer, and generates a spike of 20 kPa at 3.7 ms. after that, the complicated wave field provides a pressure trace without prominent observation.

### A.4. Jet Exit.

After the diaphragm breaks, the pressure increases and reaches its maximum value at t = 400 μs. For other gas combinations the time to reach a maximum pressure at the exit is of the same order. This was observed even for He that has a sound speed about seven times higher

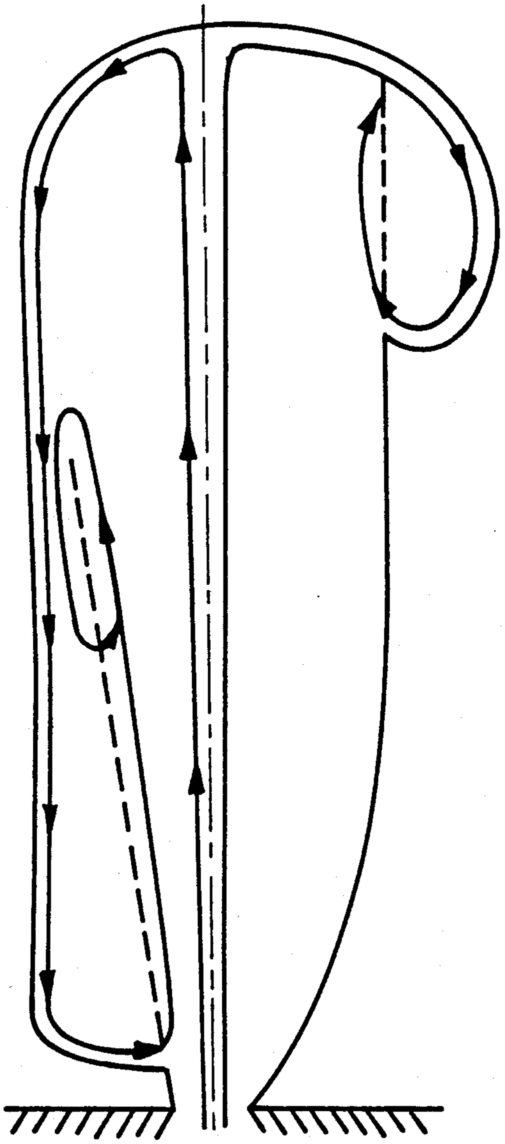

Figure A.2 Pathlines for low pressure cases: light into heavy (left) and heavy into light (right).

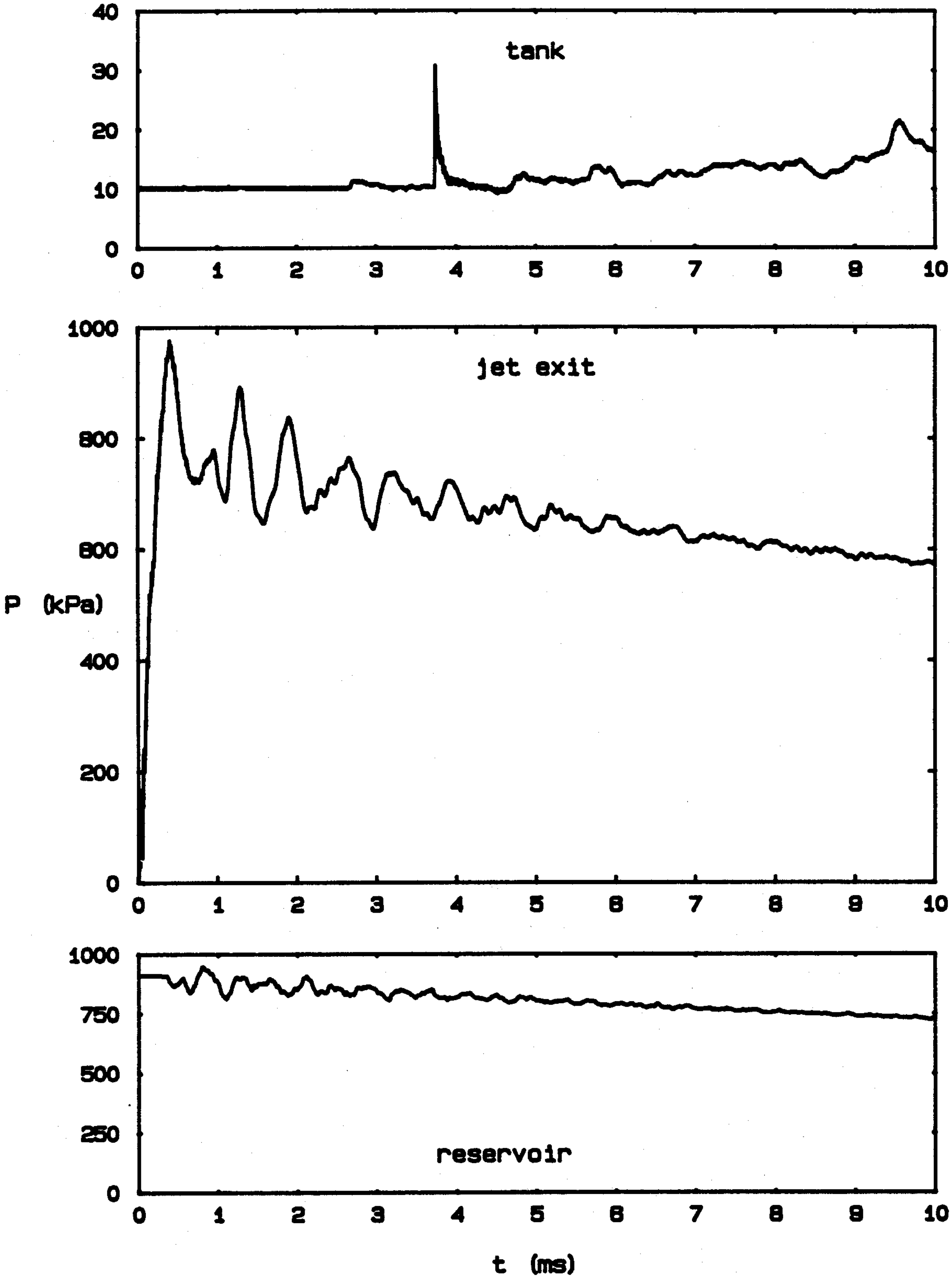

Figure A.3 Pressure history of the flow field for $SF_6$ -> $SF_6$ at $P_o/P_a = 100$.

than $SF_6$. This suggests that the method to start the flow was slower than expected. For lighter atmospheres the maximum pressure is reached at shorter times, probably because of the lower drag on the pieces of diaphragm. After the pressure reaches the maximum value, it decreases and oscillates at a frequency that is close to one of the resonance frequencies of the reservoir.

### A.5. Reservoir.

The first expansion wave reaches the bottom of the reservoir at $t = 360\ \mu s$ after the diaphragm breaks. This interval of time depends on the jet gas and on the reservoir length. The initial pressure of the reservoir is the breaking pressure of the diaphragm. This pressure is decreased as the reservoir empties and during the decay phase, the pressure oscillates due to the complicated wave field established inside the reservoir.

# Appendix B

## FILTERING THE EXPERIMENTAL DATA

The time evolution of the jet head and the bow-shock were shown in Chapter 5 and 6, respectively. The Mach number of these features was expressed in terms of the slope of the graph of location versus time in the neighborhood of the experimental point. For example in figure 6.6, this slope is obtained by a linear least square fit of three consecutive experimental points. The temporal evolution of the Mach number shown in figure 6.6 for the bow-shock oscillates with a frequency which was found to be close to 13 kHz and independent of the experimental conditions. The only oscillating event in the experiment with this frequency is the sweeping light beam inside the camera. Since this frequency was not due to a gas-dynamic effect, attempts to filter it were made and are shown in this section.

A common technique used to filter data is by performing a Fourier transform. This technique takes the Fourier transform of the experimental data and filters out the high frequencies. An inverse transformation is executed leading to the filtered data. As a result of the insufficient amount of experimental data, it became impractical to use this procedure.

Other attempts to find a general law to filter the data involved the use of sinusoidal waves as well as modulated amplitude waves. The last one was found to be the most acceptable for this purpose since the obtained data exhibited a modulation in amplitude. In figure 6.6 the evolution in Mach number is represented both by the derivative of the experimental points ($\Delta$) and the derivative of the line representing the least square fit for the position of the bow-shock (dashed). The result obtained by the subtraction of the ordinate of the dashed curve from the ordinate of the discrete distribution is the variation in the

Mach number of the bow-shock. Figure B.1 shows a plot of the variation in Mach number $\Delta M$; the modulated wave that provided the least square fit for the experimental points, and the result of the filtering obtained by subtracting the modulated wave from the variation in Mach number ($\Delta M$). The modulated amplitude wave for this case has a frequency of 13.5 kHz and a modulation frequency of 0.95 kHz.

The result obtained in figure B.1 shows that the modulated wave used for filtering, did not provide a good result; this is due to the presence of other frequencies in the signal. Similar plots were obtained for the other different cases: All the gas combinations showed frequencies around 13 kHz. However differences between their amplitudes were so large that there was no available method to remove this effect, even when considering the corresponding frames on the movie.

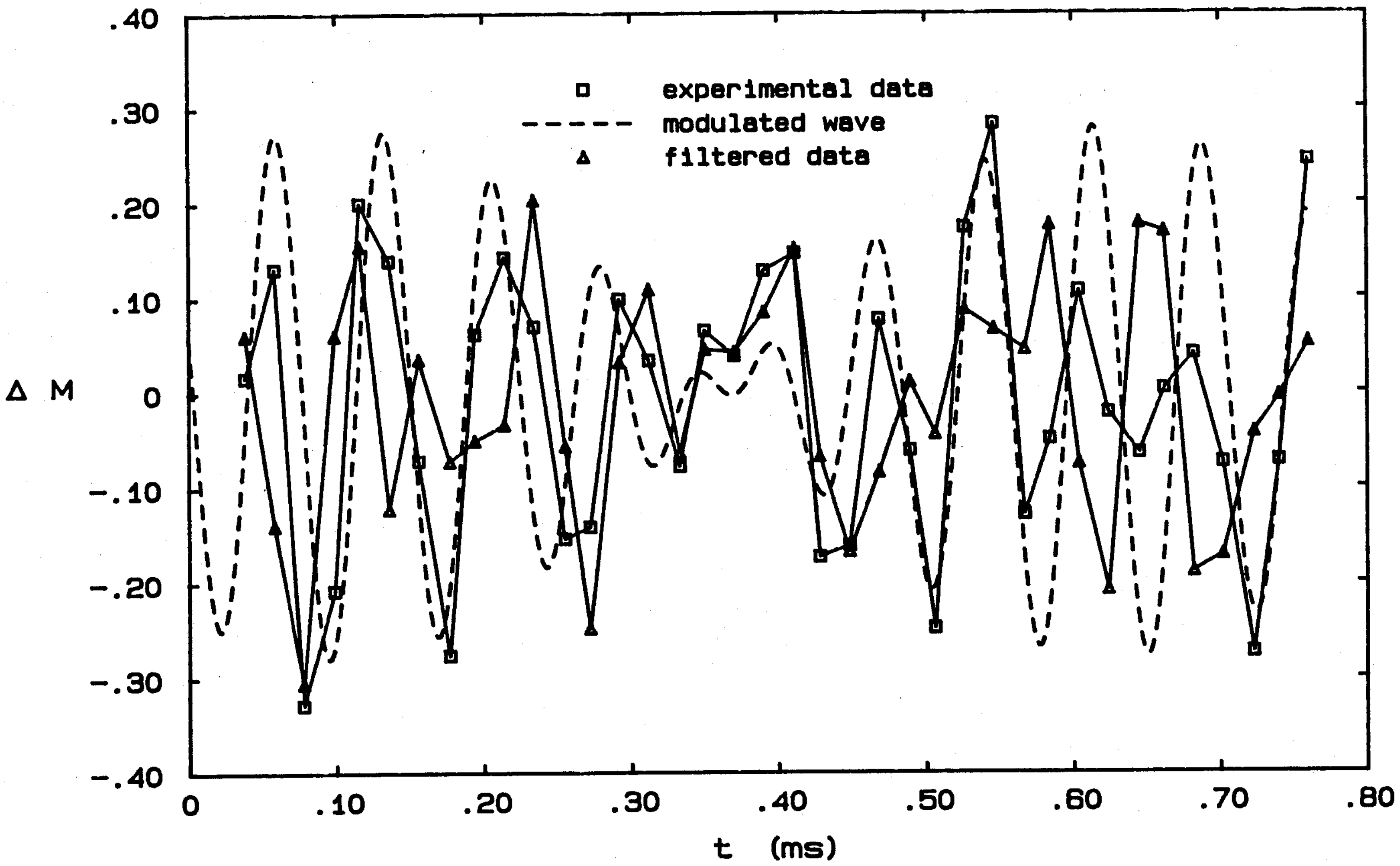

Figure B.1 Attempt to filter the experimental data from 13 kHz.

# Appendix C

# THE HIGH SPEED CAMERA

## C.1. Description of the Camera.

The Cordin camera, model 374A, is capable of taking 512 pictures at a preset rate ranging from 10,000 to 100,000 frames per second at intervals of 100 frames per second. It consists of a rotating drum on whose surface is positioned a one meter long strip of film, as shown in figure C.1. The film is exposed during one revolution of the drum, and provides four columns of pictures. The film is held on the inner surface of the drum by the centrifugal force and on its edges by friction. A light proof loading cassette is used to insert the film onto the drum surface. Before running, the camera is evacuated to avoid drag on film and consequent film damage. Shuttering action is provided by a nine-faced counter-rotating prism and the aperture stop denoted $A_3$ in figure C.1. The prism rotates 14.22 times faster than the drum.

The self-illuminated object is located at a distance from the camera's entrance lens, a Canon 200 mm, f/2.5 5:1 zoom. After passing through this lens, the light beam can be deflected through the ocular O using the viewing prism $\Pi_1$, tilted to position B to view the object for alignment and focusing purposes.

Once the camera focus is adjusted, the prism is returned to position A, allowing the light beam to pass through the aperture stop $A_1$, the lens $L_2$, the stop $A_2$, the open shutter S, and the lens $L_3$. The light is reflected by the mirror $m_1$, passes through lens $L_4$, and then reflects from the face of the rotating prism $\Pi_2$. Depending on the instantaneous orientation of that face, the light beam will be incident on one of the apertures denoted $A_3$. Each aperture is associated with an optical arrangement formed by lenses $L_5$ and $L_6$ and mirrors $m_2$ and $m_3$.

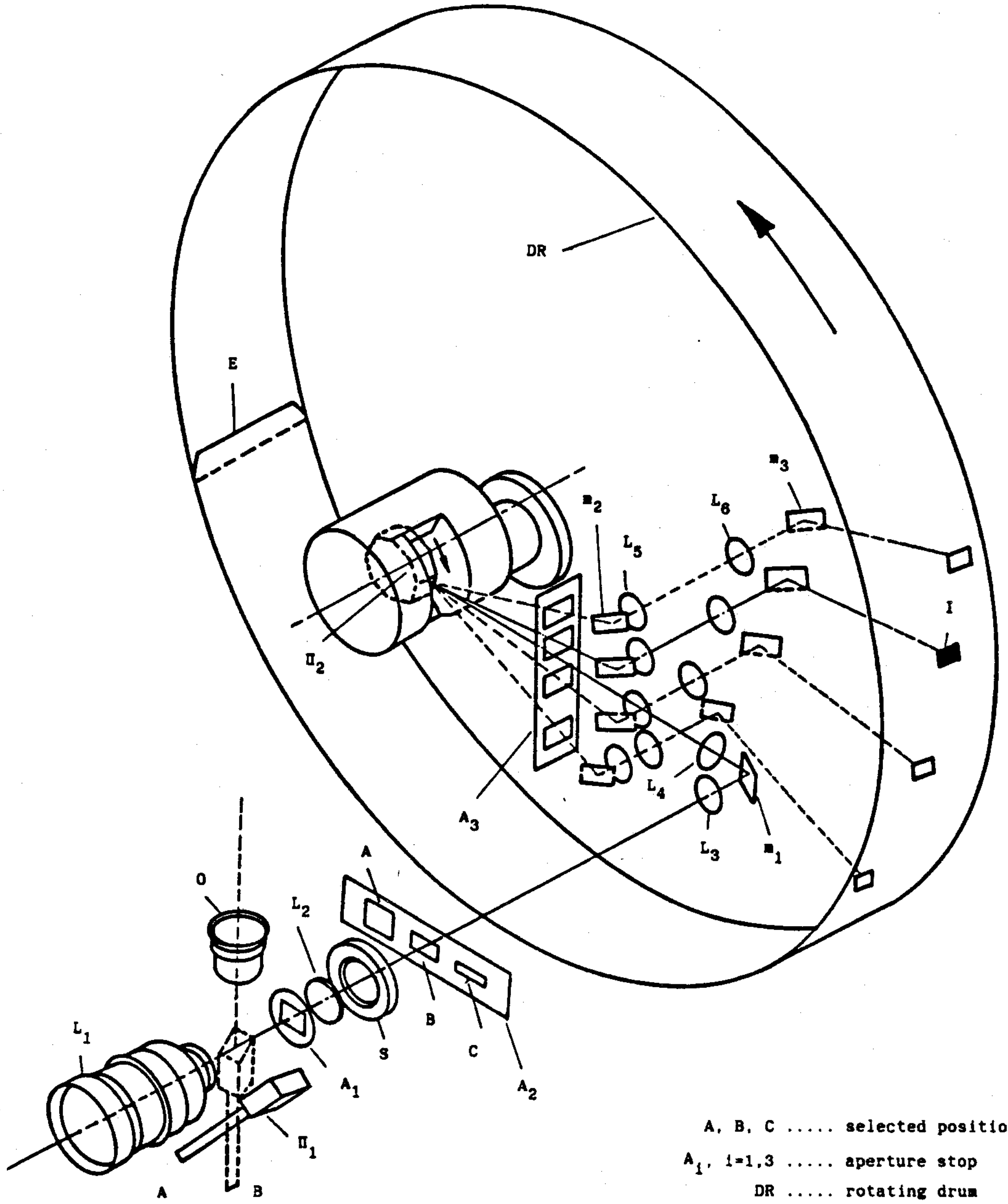

A, B, C ..... selected positions
$A_i$, $i=1,3$ ..... aperture stop
DR ..... rotating drum
E ..... overlap of the film edges
I ..... image on film plane
$L_i$, $i=1,6$ ..... lens
$m_i$, $i=1,3$ ..... plane mirror
O ..... ocular
S ..... shutter
$\Pi_1$ ..... viewing prism
$\Pi_2$ ..... contra-rotating prism

Figure C.1 General view of the optical arrangement for the high speed Cordin model 374A camera.

The complete optical arrangement generates an image I on the film on the inner surface of the drum.

There are three sets of aperture stops $A_3$ available that provide time exposures of 1.0, 2.0 or 4.0 μs, with the camera running at 100,000 frames per second. Once the above aperture stop is in position, another associated stop, $A_2$, is selected at either position A, B or C, to be compatible with the desired time exposure. The camera cap shutter S is the part that allows light to enter the camera, and for this experiment it was used only as a security device, due to its long opening and closing times of 13 ms.

A sample of exposed film is shown, actual size, in figure C.2. The frame sequence is diagonal, and a magnified view of a typical frame is also given. The demagnification of the image on the film is given by the ratio between the jet exit diameter D and the jet exit diameter d measured on the film. As a result of the camera design, each column of pictures gives a different demagnification of the image. For the present experiment this is shown in table C.1.

Table C.1 Demagnification of the Jet Image

| Column | D/d |
|---|---|
| I | 16.1 |
| II | 15.5 |
| III | 15.5 |
| IV | 16.2 |

We take the initial frame to be the one that precedes the first picture of the jet. With this origin, x - t diagrams can be plotted, and extrapolated to the x-axis to define the real origin. The time difference

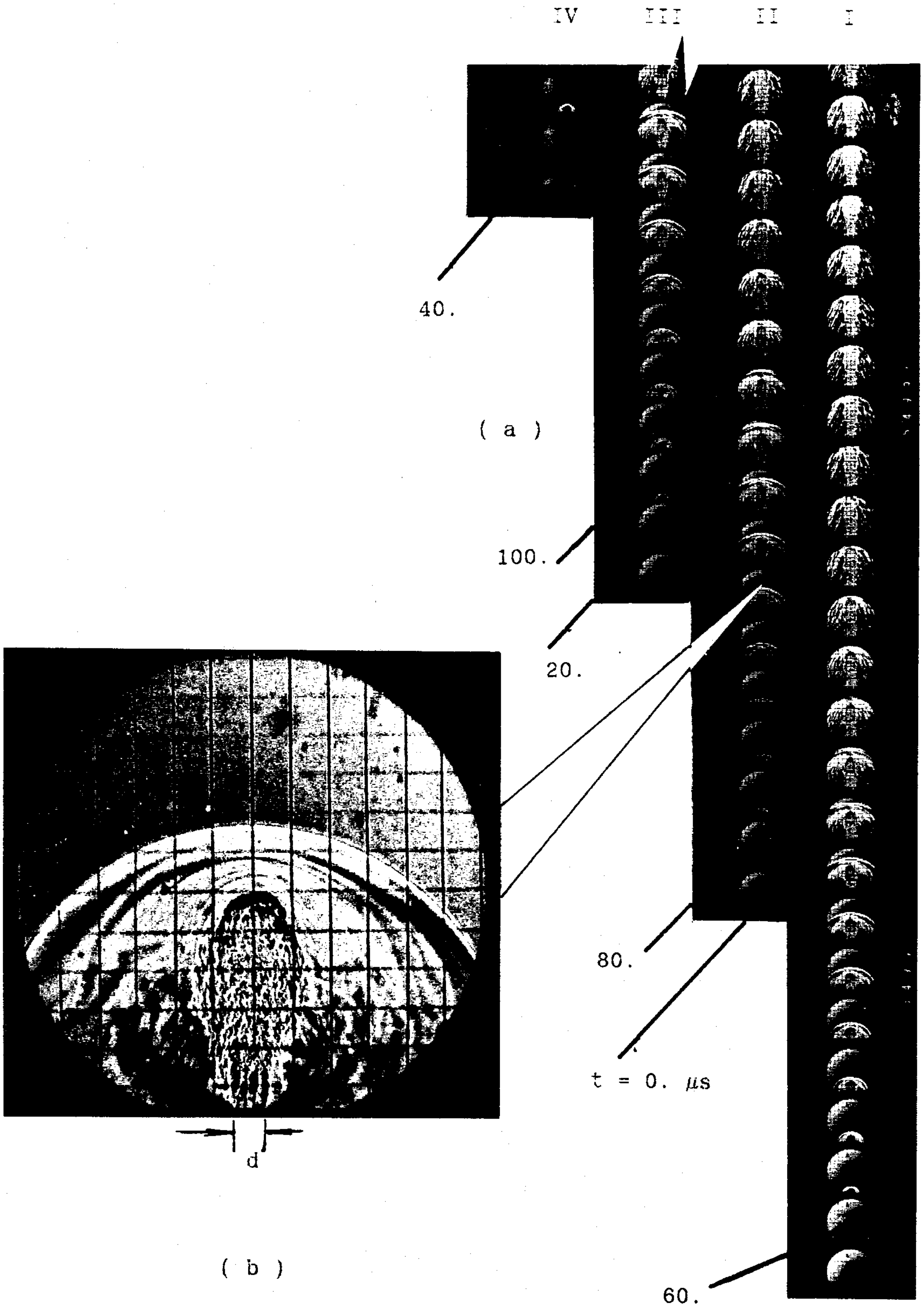

Figure C.2 Film recording by the high speed camera: (a) real size film showing diagonal sequence of pictures, and (b) magnification of an individual frame.

between the initial frame and the time origin is applied to all frames to provide the actual timing.

## C.2. The Camera as a Timing device.

The purpose of using the high-speed camera was to take a large number of pictures to obtain the time evolution of selected features. This requires a precise knowledge of the rate at which the pictures are being taken. The camera control panel provides the instantaneous framing rate through a digital display with an accuracy of 2%. The timing may be improved by directly measuring the time exposure of each frame.

The opto-electronical set-up used for this measurement as well as the results are shown in figure C.3. The idea consists of placing four photodiodes inside the camera. Each photodetector was placed at the optical exit of each relay lens, $L_6$, shown in figure C.1. They were used as a normally-open switch that is closed, i.e., current flows, when exposed to the light. TIL81 phototransistors made by Texas Instruments were used, with +10 V applied to the collector and the base was grounded with a 160 KΩ 0.4 W resistor. The advantage of this arrangement is that short rise time of 0.3 $\mu$s is obtained. The phototransistor has 20% of its maximum spectral response at $\lambda = 0.6$ $\mu$m.

The wiring from the optoeletronical devices were routed to the exterior of the camera through a vacuum-tight mount, enabling the experiment to be performed under vacuum, at any desired framing rate, without damage. The wires were connected to Nicolet dual-trace oscilloscope described in Chapter 2. The output of each of the photodiodes was recorded in turn (using a selector switch), relative to the output of one of the diodes used as a reference.

The scope output was recorded on floppy disk and plotted in fig. C.3.b From these traces a more accurate timing was possible. The time separation between tracks 4 and 1 is 21 $\mu$s; between tracks 1 and 2 is 20 $\mu$s; between tracks 2 and 3 is 20 $\mu$s and between 3 and 4 is 17 $\mu$s.

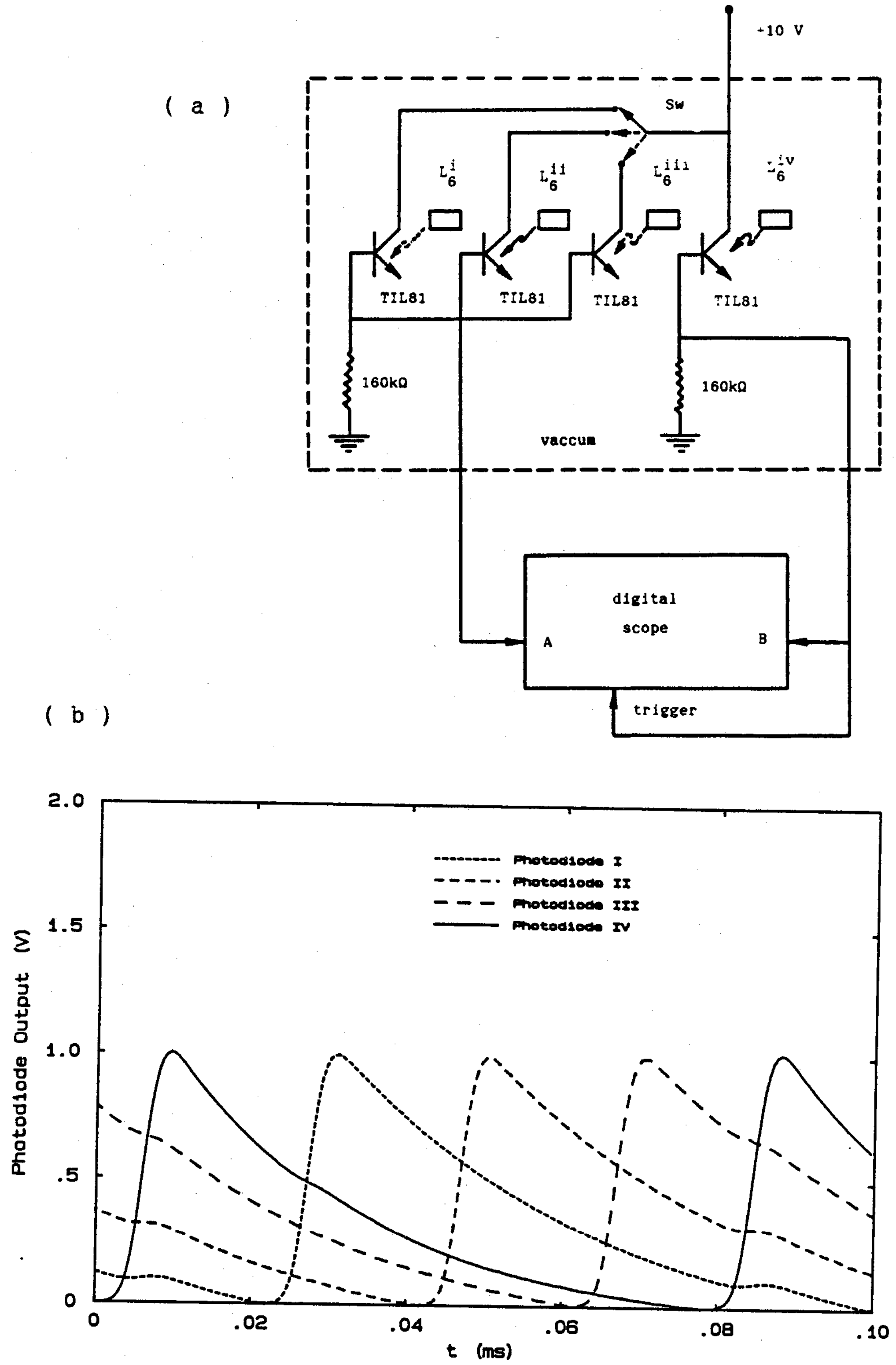

Figure C.3 Calibration of the high speed movie camera: (a) electronical circuit, and (b) result of the timing experiment.

These data were obtained with the camera running at the nominal rate of 50,000 frames per second.

# Appendix D

## THE QUASI-STEADY EVOLUTION OF THE JET

### D.1. The Mach Disk Location.

The location of the Mach disk was observed to be unsteady for the starting phase of the jet. In order to understand its dependence on the flow parameters, an argument based on the entropy balance principle for steady jets from Young (1975), is shown below. This principle states that the total change in molar entropy for the jet gas from the stagnation state (o) to the state far downstream (∞), in figure 1.1, is equal to the sum of the two changes in molar entropy: one is across the Mach disk and the other is the change that the flow undergoes after the Mach disk until far downstream. The molar entropy between the initial state and the final state ($\Delta S_{o,\infty}/R$), can be found in terms of the pressure (P) and temperature (T) of the initial (o) and final (∞) states and $\gamma_o$. It is given by the relation shown below:

$$\frac{\Delta S_{o,\infty}}{R} = \ln \left[ \left(\frac{P_o}{P_\infty}\right) \left(\frac{T_\infty}{T_o}\right)^{\gamma_o/\gamma_o - 1} \right] \tag{D.1}$$

The flow inside the jet core up to the Mach disk, can be considered to be isentropic and the Mach disk can be approximated by a normal shock. The molar entropy change across the Mach disk ($\Delta S_{n,m}/R$) can be found in terms of $\gamma_o$ and the Mach number upstream of the Mach disk ($M \gg 1$). It is given by the following expression:

$$\frac{\Delta S_{n,m}}{R} \simeq \ln \left[ \left(\frac{\gamma_o + 1}{\gamma_o - 1}\right)^{-\gamma_o/(\gamma_o - 1)} \left(\frac{2\gamma_o}{\gamma_o + 1}\right)^{1/(\gamma_o - 1)} M^{2/(\gamma_o - 1)} \right] \tag{D.2}$$

The process that the gas undergoes after crossing the Mach disk up to the state far downstream can be considered isobaric. Thus the molar entropy change ($\Delta S_{m,\infty}/R$) in terms of temperature (T) and $\gamma_o$ is given by:

$$\frac{\Delta S_{m,\infty}}{R} = \frac{\gamma_o}{\gamma_o - 1} \ln\left(\frac{T_\infty}{T_m}\right) \tag{D.3}$$

The Mach number inside a supersonic jet, in terms of the distance downstream of the sonic exit (X/D) and $\gamma_o$, is given by an empirical result by Ashkenas & Sherman (1966):

$$M \simeq (2.2)^{(\gamma_o-1)/2} \, [\gamma_o(\gamma_o - 1)]^{(\gamma_o-1)/4} \left(\frac{\gamma_o + 1}{\gamma_o - 1}\right)^{(\gamma_o+1)/4} \left(\frac{X}{D}\right)^{(\gamma_o-1)} \tag{D.4}$$

Substituting (4.4) into (4.2) and adding (4.3), the result obtained is the total change in molar entropy that is equal to (4.1). Equating both right hand sides, the expression leads to:

$$\frac{X}{D} = f(\gamma_o) \left(\frac{P_o}{P_\infty}\right)^{1/2} \tag{D.5}$$

The function $f(\gamma_o)$ depends weakly on $\gamma_o$ and has values close to 0.67 obtained by Ashkenas & Sherman (1966), for $\gamma_o$ ranging from 1.100 to 1.667.

### D.2. The Jet Head Location.

The initial evolution of the jet head was verified to be linear with time and after some time damped behavior was exhibited. A simple argument based on entrainment was carried out to verify the dependence on time and is shown below. A previous study by Ricou & Spalding (1961) was done on entrainment by axisymmetrical turbulent jets. They showed that the entrainment rate $\dot{m}$, at a point X/D inside a jet of gas with density $\rho_o$, into an atmospheric gas with density $\rho_a$ that is generated by a mass flux $\dot{m}_e$ from an exit with diameter D, is given by:

$$\dot{m} = 0.32\ \dot{m}_e \left[\frac{X}{D}\right] \left[\frac{\rho_a}{\rho_o}\right]^{1/2} \quad . \qquad (D.6)$$

The entrainment rate after the Mach disk for the jet under study, where the flow is subsonic, can be approximated by:

$$\dot{m} \simeq \rho_a \frac{\pi b^2}{4} \frac{dX}{dt} \qquad (D.7)$$

It can be assumed that the thickness of the jet b is proportional to the distance X (b = C X) . Substituting this assumption into (D.7) and equating to (D.6), it can be found that:

$$\frac{X}{D} = \left[\frac{4}{3\pi^{1/2}C^2}\right]^{1/2} \left\{ \left(\frac{2}{\gamma+1}\right)^{\frac{\gamma}{2(\gamma-1)}} \left[\frac{\rho_o}{\rho_a}\right]^{1/2} \right\}^{1/2} \left[t\ \frac{a_o}{D}\right]^{1/2} \qquad (D.8)$$

This result shows how entrainment attenuates the evolution of the jet head and the dependency on density ratio.

# 1. References

ASHKENAS, H. & SHERMAN, F.S. 1966 Rarefied Gas Dynamics, 4th Symposium vol.II, pp84/105 Academic Press, N.Y.

CRIST, S.; SHERMAN, P.M. & GLASS, D.R. 1968 Study of the Highly Underexpanded Sonic Jet. AIAA J. 4(1).

DONALDSON, C. duP. 1966 A Brief Review of Research on the Impingement of Axially Symmetric Free Jets. Proc. Aeroesp. Eng. Conf. 74-110.

HAMMOND, C.M. & WIGGINS, T.A. 1972 Hypersound Speeds in Sulfur Hexafluoride. J.Acoust.Soc.Am. 52(5) part 2, pp.1373-6.

Joint Army, Navy, NASA, Air Force (JANNAF) 1975 Handbook of Rocket Exhaust Plume Technology. Chap 2 Chemical Propulsion Agency, Washington, D.C.

KIEFFER, S.W. & STURTEVANT, B. 1984 Laboratories Studies of Volcanic Jets. Journal of Geophysical Research 89(B10), p.8253-68.

LIEPMANN, H.W. & ROSHKO, A. 1957 The Elements of Gasdynamics. John Wiley, N.Y.

LIN, J.M.C., 1986 Private Communication.

LOVE, E.S.; GRIGSBY, C.E.; LEE, L.P. & WOODLING, M.J. 1959 Experimental and Theoretical Studies of Axisymmetric Free Jets. NASA TR R-6, Langley Research Center.

MARSHALL, N. 1976 Gas Encyclopaedia. Elsevier, N.Y.

NABOKO, I.M.; BELAVIN, V.A. & GOLUB, V.V. 1979 Non Stationary Wave Structure of Intermittent Supersonic Jet. Acta.Astro. B6, pp.885-90.

NORMAN, M.L.; WINKLER, K.H.A. & SMARR, L.L. 1983 Propagation and Morphology of Pressure Confined Supersonic Jets. MPA 61, Max Planck Intitut, Munich.

RICOU, F.P & SPALDING, D.B. 1961 Measurements of Entrainment by Axisymmetric Turbulent Jets. JFM (11), pp.21-32.

SCHMIDT, E.M. & SHEAR, D.D. 1974 The Formation and Decay of Impulsive Supersonic Jets. AIAA Paper No. 74-531.

SMITH, M.D.;NORMAN, M.L.;WINKLER, K.H.A. & SMARR, L.L. 1984 Hot Spots In Radio Galaxies; A Comparison With Hydrodynamic Simulations. MPA 150, Max Planck Institut, Munich.

TACHEON, D. 1975 Statistical Thermodynamic Properties of Hexafluoride Molecules. Los Alamos Nat. Lab. Rep, August.

TOMBACH, I.H. 1969 Velocity Measurements with a New Probe in Inhomogeneous Turbulent Jets. Ph.D. Thesis, California Institute of Technology.

WEAST, R.C. 1983 CRC Handbook of Chemistry and Physics CRC Press.

YOUNG, W.S. 1975 Derivation of the free-jet Mach disk location using the entropy balance principle. The Physics of Fluids 18(11),pp.1421-25.